MODELLING OF INSTABILITIES IN MAGNETO-ELASTIC MEMBRANES

Master Thesis
in the study programme Computational Engineering

submitted by

Vinayak Balasaheb Gholap
Matriculation number: 22065422
born on 01.11.1993 in Pune, India

performed at

Chair of Applied Mechanics (LTM)
Friedrich-Alexander-Universität Erlangen–Nürnberg
(Prof. Dr.-Ing. habil. Paul Steinmann)

Examiner: Prof. Dr.-Ing. habil. Paul Steinmann

Supervisors: Dr. Jean-Paul Pelteret (FAU Erlangen, Germany)
Dr. Prashant Saxena (University of Glasgow, UK)

Date of submission: March 18, 2019

Ehrenwörtliche Erklärung / Declaration

Ich versichere, dass ich die Arbeit ohne fremde Hilfe und ohne Benutzung anderer als der angegebenen Quellen angefertigt habe und dass die Arbeit in gleicher oder ähnlicher Form noch keiner anderen Prüfungsbehörde vorgelegen hat und von dieser als Teil einer Prüfungsleistung angenommen wurde. Alle Ausführungen, die wörtlich oder sinngemäß übernommen wurden, sind als solche gekennzeichnet.

Der Universität Erlangen-Nürnberg, vertreten durch die Lehrstuhl für Technische Mechanik, wird für Zwecke der Forschung und Lehre ein einfaches, kostenloses, zeitlich und örtlich unbeschränktes Nutzungsrecht an den Arbeitsergebnissen der Master Thesis einschließlich etwaiger Schutzrechte und Urheberrechte eingeräumt.

I hereby declare formally that I have developed and written the enclosed thesis entirely by myself and have not used sources or means without declaration in the text. Any thoughts or quotations which were inferred from the sources are marked as such. This thesis was not submitted in the same or a substantially similar version to any other authority to achieve an academic grading.

Erlangen, den 18. März 2019

Vinayak Gholap

Acknowledgments

This report is the official document of the Master Thesis conducted for 30 ECTS by Vinayak Gholap in the course of M.Sc. Computational Engineering.

I would like to specially thank my advisor Dr. Jean-Paul Pelteret for providing me this interesting topic and for his continuous support, guidance and honest remarks during the course of this work. He has given me the freedom and time to work on my concepts and help me channelize our ideas into appropriate direction. I also thank my second supervisor Dr. Prashant Saxena for his valuable feedbacks on the documentation and his insightful suggestions to overcome the hurdles and difficulties that we faced in the course of this research. This project would have not been possible without the many fruitful discussions and conversations the three of us have had.

I would like to thank Prof. Dr.-Ing. Paul Steinmann for providing the working environment at his chair. His insightful courses have been instrumental in my personal knowledge development over the past three years.

I would like to sincerely express my gratitude to all the people who have helped me continuously through this exciting journey. A cheerful shout-out to Dr. Denis Davydov for introducing me to the `deal.II` library through a project opportunity which helped me with an easy start to my thesis. I would specially like to thank the `deal.II` community group and the contributors for the wonderful platform they have build to share and communicate the thoughts with other people.

Above all, I would like to express my sincere gratitude to my family and my brother and sisters in India and my friends in Germany for their kind love and persistent belief in me throughout my studies. The moral support and love that I received from them has made this journey comfortable and worthwhile.

Vinayak Gholap
Erlangen, March 18, 2019

Contents

List of Figures

List of Tables

List of Algorithms

1 Introduction

1.1 Motivation

Magnetorheological elastomers (MREs) are soft materials which consist of micron sized iron particles dispersed in an elastomeric matrix. Magneto-active polymers (MAPs) termed as smart materials of future are capable to change their mechanical properties under the application of magnetic loads. This is due to the interaction of the ferrous magnetizable particles which gives rise to a coupled magneto-mechanical effect. In the presence of an external magnetic field, the magnetization vectors in iron particles align with the externally applied magnetic field and this causes a change in the mechanical stiffness and the macroscopic deformation of the polymer. Various polymers such as natural and synthetic rubber, hydrogels, silicon elastomers and polyurethanes have been utilized as the matrix material to synthesize MAPs [22]. The different magnetic filler particles used are iron particles in micro- and nano-size. The proportion of these filler particles is usually between 0 and 30% by volume of the entire mixture [32]. The finite deformations arising from the coupled interaction of the magnetic and mechanical fields is desired in many industrial applications. MAPs are synthesized and tuned with different micro-structural properties for a variety of applications such as magnetic actuators and vibrational dampers in mechatronic sensors and artificial muscles in the biomedical field.

Motivated by the plethora of applications, the theory of MAPs macroscopic behaviour at continuum level proposed by [1, 2] is reviewed again by researchers. New modelling approaches were recently developed by [6, 9, 8, 11, 21, 28]. These recent contributions form the theoretical foundation for the present work described in this thesis. In the work by [8, 11] it was pointed out that any one of the three magnetic vector fields, namely the magnetic field $\mathbb{H}$, the magnetic induction $\mathbb{B}$ and the magnetization $\mathbb{M}$, can be used as an independent input field to proceed with the mathematical modelling. The other two fields can be obtained through constitutive relations. Two different formulations depending on the choice of the independent field, termed as the scalar magnetic potential formulation and the vector magnetic potential formulation, were presented in [8, 11]. The difficulties arising in terms of numerical modelling and the restrictions on the choice of the class of constitutive material models to describe MAPs was also highlighted therein.

The solution of non-trivial boundary value problems through numerical modelling was the obvious next step in understanding the nature of the coupled response of these smart materials. The elastic partial differential equations (PDEs) for the material deformation and the magnetic PDEs for the magnetic field are solved using the favourable discretiza-

tion approach such as Finite Element method (FEM). FE simulations of the deformations of the magneto-elastic materials have been performed considering different geometries of interest in [18, 20, 29]. Due to the applications of MAPs in the critical fields such as aerospace and biomedical engineering, the investigation of the failure and stability analysis of the materials under applied loads is of vital importance. Research studies in understanding the material behaviour near critical limit points and post limit points is carried out both analytically and numerically considering an isotropic and anisotropic material micro-structure in [26, 38, 41, 16, 31]. In an isotropic MRE, the iron particles are distributed randomly in the matrix and the resulting macroscopic response is thus isotropic. In an anisotropic MRE, the particles are arranged in chains due to the curing process during the fabrication of the material. Different numerical experiments were carried in this direction considering the chain-like micro-structure [32] and a multiscale approach using computational homogenization in [34].

Of particular interest to this thesis are the recent studies carried out in [38, 41] for isotropic MREs with axisymmetric geometries under inflating pressure loads. In case of membranes of finite thickness it is already known from the stability and buckling analysis that the elastic limit points are an important phenomenon during the free inflation of these thin membranes under finite pressure loads. At the critical limit points, the membranes start to deform significantly under a slight increase of pressure load. The material softens and due to reduced stiffness we may observe buckling or wrinkling effects in the membranes. The behaviour of the material beyond these limit points leads to multiple equilibrium states, stable or unstable or both. Hence, it is important to know a priori the limit point and the limit pressure load a membrane can withstand before a structural failure is observed. The instability behaviour of such membranes is also dependent on the constitutive material model employed to describe the magneto-elastic material response. The presence of a magnetic limit point instability, a state where both the stable and unstable equilibriums merge and cease to exist, was described in [16, 38].

In the macroscopic modelling approaches [24, 36], the energy contributions arising from the surrounding free space around the magneto-elastic membrane are also taken into consideration. The forces arising from the Maxwell stress developed in the free space by the permeating magnetic field are significant and thus need to be taken into account. The approach of a FE mesh with truncated free space from [36] was adopted in this thesis. The magneto-elastic membrane geometry along with the truncated surrounding free space was discretized using finite element basis in order to capture a more accurate response of the deformable membrane and the free space. The free space was modelled as an elastic deformable solid with relatively low elastic stiffness compared to the magneto-elastic membrane stiffness.

The research plan for this thesis is to make an attempt to model the instabilities in the finite thickness torus membranes employing the h-adaptive mesh refinement finite elements. The lack of research in the numerical modelling of axisymmetric magneto-elastic solids modelled with the surrounding free space employing FEM is the main motivation for the thesis. Development of a robust and computationally efficient multi-physics,

fully coupled finite element framework for the magneto-elasticity problems employing open-source, high-performance C++ FEM library such as `deal.II` [15, 39] is the basic goal. The developed framework tested with various sample models and unit tests to proof-check the correct functioning may be useful as a starting point for the further research.

1.2 Research objectives

The research direction and the discrete objectives aimed to achieve in this thesis are precisely listed below.

- Magneto-static magnetic scalar potential (MSP) formulation:
  1. Devise a method of modelling the thin tubular membrane toroidal geometry using the MSP formulation
  2. Set up simulation code for the 3D and axisymmetric (2.5D) problem
  3. Validate the axisymmetric formulation
- Quasi-static finite strain elasticity problem:
  1. Understand and implement a quasi-static finite-strain elasticity problem for pure mechanical loads and deformations [35, 23]
  2. Extend the application code from previous task to include finite elasticity
  3. Implement a constitutive material law considering the geometric and material non-linearity of an isotropic continuum elastic body [17]
  4. Implement an iterative Newton method with (quasi-static linear) load incrementing algorithm to solve for the vector-valued displacements
  5. Test the developed code with mechanical test problems that exhibit finite deformations with instability/buckling characteristics
- Coupled magneto-elasticity problem:
  1. Implement a material model for the coupled problem [36, 32]
  2. Extend the application code incorporating the conclusions drawn from both of the previous decoupled problems
  3. Implement a segregated iterative solver from the literature [10] to solve the coupled saddle point system
  4. Examine material behaviour at high mechanical and magnetic loads for material instability

1.3 Outline of the thesis

This thesis is organised into four chapters. The first chapter introduced the magneto-active polymers and presents a short summary of the research performed and undergoing in these smart materials. It motivates the need to model the unstable behaviour of inflating membranes of finite thickness and also points to its importance in practical applications in different industries. As mentioned briefly above in the research objectives, the thesis was carried out in three major milestones described in the next three chapters. In the second chapter, the theory for non-linear magneto-elasticity is laid out. A particular axisymmetric (2.5D) and a 3D geometry for the membrane and the free space is developed. Different experiments are performed to model a magnetic field closely fitting to the desired results from the existing literature. Validation of the axisymmetric formulation is carried out by comparing the results against the results of a 3D model simulation. The third chapter is dedicated to the finite deformations of the membrane along with the free space under quasi-static inflating pressure loads. Here, the membrane is modelled employing a standard Neo-Hookean constitutive material law and the surrounding free space as another non-linear complaint elastic solid. The considered solution field is the vector-valued displacement field only. Linearisation of the non-linear quantities is carried out and a non-linear Newton solver is implemented. A number of mechanical test problems are presented to proof-check the implementation at various stages of code development and to validate the behaviour of the modelling approach. Test models are also developed from the literature to study the instability behaviour under finite strain elasticity framework and to demonstrate the failure of Newton method at/near critical limit points. The fourth chapter deals with coupling of the problems from Chapter 2 and Chapter 3. Different conclusions drawn from the results of previous chapters are taken into consideration to modify the approach in order to model the instabilities. The implemented material model in Chapter 3 is extended to account for the additional energy contribution from the magnetic loads and the coupled interaction of the elastic and magnetic fields. Corresponding linearisations for the updated material model are derived and implemented to form a linear system of equations. The solution strategies of the resulting saddle point system are discussed in detail. A test model for the coupled problem to gain understanding of the behaviour of the material under combined loads is simulated. Finally, an attempt is made to initiate and model the buckling instability in the membrane near the limit points.

2 Magneto-static magnetic scalar potential

2.1 Kinematics

We consider a magneto-elastic solid body $\mathcal{B}_0$ in a three-dimensional Euclidean space that is initially in stress-free configuration, not subjected to any mechanical or magnetic field loads. On application of a magnetic load defined by a magnetic field $\mathbb{H}$ and an associated magnetic induction $\mathbb{B}$ and magnetization vector $\mathbb{M}$, in the absence of any mechanical load, the body will undergo some deformation due to this magnetic load. This phenomenon is referred to as *magnetostriction*. Let the resulting deformed configuration from the magnetostriction be denoted as $\mathcal{B}_t$. This configuration will depend on the choice of the initial magnetic field $\mathbb{H}$.

Let any point in the reference configuration $\mathcal{B}_0$ be identified by the position vector $\mathbf{X}$ and it's position in the deformed configuration $\mathcal{B}_t$ be given as $\mathbf{x} = \boldsymbol{\varphi}(\mathbf{X})$. The field $\boldsymbol{\varphi}$ is a one-to-one mapping describing the deformation of the body. The associated deformation gradient $\mathbf{F}$ relative to $\mathcal{B}_0$ is defined as $\mathbf{F} := \nabla_0 \boldsymbol{\varphi}$ and it's determinant is $J = \det\mathbf{F} > 0$ (non-negative to avoid material self-penetration). The gradient w.r.t. the reference configuration $\mathcal{B}_0$ is denoted as ∇_0 and the gradient w.r.t. the deformed configuration $\mathcal{B}_t$ be denoted as ∇. The magnetic vector fields in the deformed configuration are denoted as $\mathbb{b}, \mathbb{h}$ and $\mathbb{m}$.

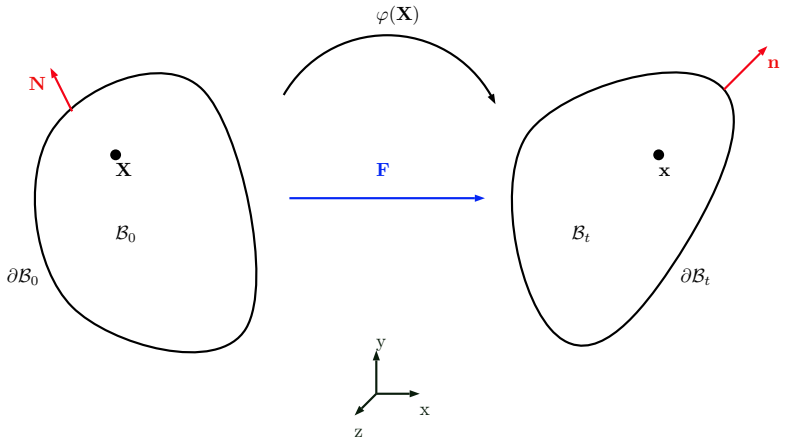

Figure 2.1: Kinematics

2.2 Balance equations

2.2.1 Magnetic balance laws

In the absence of any deformation ($\mathbf{F} = \mathbf{I}$), the magnetic quantities $\mathbb{b}, \mathbb{h}, \mathbb{m}$ are related by the standard formula

$$\mathbb{b} = \mu_0(\mathbb{h} + \mathbb{m}), \tag{2.1}$$

where $\mu_0 = 4\pi \times 10^{-7}\mathrm{Hm}^{-1}$ is the magnetic permeability in vacuum.

For the case of time-independent problems and in the absence of external currents, from the Ampere's law we have [9]

$$\mathrm{curl}(\mathbb{h}) = \nabla \times (\mathbb{h}) = \mathbf{0}. \tag{2.2}$$

For the case of magneto-statics (absence of time varying electromagnetic fields), from the assumption of the absence of magnetic monopoles we have [9]

$$\mathrm{div}(\mathbb{b}) = \nabla \cdot \mathbb{b} = 0. \tag{2.3}$$

Both the Equations (2.2) and (2.3) are the specializations of Maxwell's equations. Equation (2.1) defines the third vector field when one field is used as an independent variable and the other field is provided by an appropriate constitutive law.

2.2.2 Mechanical balance laws

The balance law for mass conservation is given as

$$\frac{d\rho}{dt} + \nabla \cdot [\rho \dot{\mathbf{x}}] = 0, \tag{2.4}$$

where ρ is the mass density in $\mathcal{B}_t$.

From the balance law for linear momentum assuming that the inertial effects are negligible, we have the equilibrium equation

$$\mathrm{div}\boldsymbol{\sigma} + \boldsymbol{b}_t = \mathbf{0} \quad \text{in } \mathcal{B}_t, \tag{2.5}$$

where $\boldsymbol{\sigma}$ is the Cauchy stress tensor and $\boldsymbol{b}_t$ is the body load per unit current volume. The balance of angular momentum leads to the requirement that $\boldsymbol{\sigma}$ is symmetric.

2.3 Boundary conditions

In order to formulate a boundary-value problem we need constitutive laws in which $\boldsymbol{\sigma}$ and $\mathbb{b}$ are given in terms of the variables $\mathbf{F}$ and $\mathbb{h}$. Additionally, appropriate boundary

conditions must be satisfied by the fields $\mathbb{b}, \boldsymbol{\sigma}$ and $\boldsymbol{\varphi}$. At a bounding surface of the material body in the deformed configuration, the vector fields $\mathbb{b}$ and $\mathbb{h}$ satisfy the standard jump conditions

$$\mathbf{n} \cdot [\![\mathbb{b}]\!] = 0, \quad \mathbf{n} \times [\![\mathbb{h}]\!] = \mathbf{0} \quad \text{on } \partial\mathcal{B}_t, \tag{2.6}$$

where the square brackets indicate a jump across the surface and $\mathbf{n}$ is the outward pointing unit normal vector to the surface in the deformed configuration $\mathcal{B}_t$. These boundary conditions enforce that the tangential component of the magnetic field, as well as the normal component of the magnetic induction, remain continuous on the boundary [36].

2.4 Magnetic scalar potential (MSP) formulation

The magnetic field quantities $(\mathbb{b}, \mathbb{h}, \mathbb{m})$ are all discontinuous over boundaries and material interfaces: $b_{1t} \neq b_{2t}, h_{1n} \neq h_{2n}$ when $\mu_1 \neq \mu_2$ (where t and n denote the tangential and normal components, respectively). These discontinuities are difficult to model using the finite element method simulations. Thus, a fictitious quantity such as the magnetic scalar potential ϕ is used in solving the magneto-elastic problems using FEM. The magnetic scalar potential formulations can be used only in the case where there are no free currents in the domain. We define a scalar potential related to the curl-free magnetic field by [36]

$$\mathbb{h} := -\nabla\phi \quad \text{in } \mathcal{B}_t. \tag{2.7}$$

The continuity condition associated with ϕ is

$$[\![\phi]\!] = 0 \quad \text{on } \partial\mathcal{B}_t. \tag{2.8}$$

The magnetic induction vector $\mathbb{b}$ is modelled in terms of magnetic field $\mathbb{h}$, taking $\mathbb{h}$ as the independent field

$$\mathbb{b} = \mathbb{b}(\mathbb{h}). \tag{2.9}$$

We consider the magnetization $(\mathbb{m})$ and the magnetic field $(\mathbb{h})$ are aligned. For a material with relative permeability μ_r, we have

$$\mathbb{h} + \mathbb{m} = \mathbb{h} + (\mu_r - 1)\mathbb{h} = \mu_r \mathbb{h}. \tag{2.10}$$

The relation for the magnetic induction in terms of the magnetic field using the above relation is

$$\mathbb{b} = \mu_0 \mu_r \mathbb{h}. \tag{2.11}$$

2.5 Variational formulation

In this section, we will derive the axisymmetric weak form of the magnetic balance law:

$$\mathrm{div}\mathbb{b} = 0, \tag{2.12}$$

with the body symmetric about the Y-axis in the cylindrical co-ordinate system. The boundary condition is

$$\mathbf{n} \cdot [\![\mathbb{b}]\!] = 0 \quad \text{on } \partial\mathcal{B}_t \text{ (Natural boundary condition).} \tag{2.13}$$

Taking integration of the strong form over the whole domain, we have

$$\int_z \int_y \int_x \nabla \cdot \mathbb{b} \; \mathrm{d}z \; \mathrm{d}y \; \mathrm{d}x = 0 \quad \text{in } \mathcal{B}_t. \tag{2.14}$$

The rules for co-ordinate transformation between Cartesian and Cylindrical co-ordinate system are

$$\begin{aligned} x = r\cos\theta, \;\; y = r\sin\theta, \;\; z = z, \\ \mathrm{d}x = \mathrm{d}r, \;\; \mathrm{d}y = r\mathrm{d}\theta, \;\; \mathrm{d}z = \mathrm{d}z, \\ \text{with } r = \sqrt{x^2 + y^2} \text{ and } \tan\theta = \frac{y}{x}. \end{aligned} \tag{2.15}$$

Applying the rules for co-ordinate transformation, we have

$$\int_z \int_\theta \int_r \nabla \cdot \mathbb{b} \; \mathrm{d}z \; r \; \mathrm{d}\theta \; \mathrm{d}r = 0 \quad \text{in } \mathcal{B}_t. \tag{2.16}$$

For a magnetic field (induction) invariant w.r.t. the θ co-ordinate, i.e. symmetric field about the Y-axis, we have

$$\int_\theta \mathrm{d}\theta = 2\pi \implies \int_z \int_r \nabla \cdot \mathbb{b} \; \mathrm{d}z \; 2\pi r \; \mathrm{d}r = 0 \quad \text{in } \mathcal{B}_t. \tag{2.17}$$

Employing the relation given by Equation (2.11), we have

$$\int_z \int_r \mu_0\mu_r \; 2\pi r \; \nabla \cdot \mathbb{h} \; \mathrm{d}z \; \mathrm{d}r = 0 \quad \text{in } \mathcal{B}_t. \tag{2.18}$$

Equation (2.18) represents the axisymmetric formulation for the considered strong form (2.3) in the Cartesian co-ordinate system.

2.6 Finite element approximation

For modelling using the finite element method, as stated earlier, we use the magnetic scalar potential formulation. Using the definition for the magnetic field in terms of the virtual scalar potential as given in Equation (2.7), we have

$$-\int_z \int_r \mu_0\mu_r \; 2\pi r \; \nabla \cdot \nabla\phi \; \mathrm{d}z \; \mathrm{d}r = 0 \quad \text{in } \mathcal{B}_t. \tag{2.19}$$

We now introduce a test function η, which is an element of the function space V of test functions. The unknown function ϕ is an element of the function space S:

$$\phi \in S \text{ and } \eta \in V. \tag{2.20}$$

Multiplying Equation (2.19) with the test function η:

$$\int_z \int_r \mu_0 \mu_r \, 2\pi r \, [(\nabla \cdot \nabla \phi)] \eta \, \mathrm{d}z \, \mathrm{d}r = 0 \quad \forall \eta \in V. \tag{2.21}$$

We observe different continuity requirements hold concerning the solution function ϕ and the test function η; ϕ is required to have second derivatives thus indicating continuous first derivatives, whereas there is no derivative on η. Thus the two function spaces S and V are not the same. This leads to an unsymmetrical formulation. To avoid this, we reformulate the above equation using integration by parts to have a symmetric formulation

$$\int_z \int_r \mu_0 \mu_r \, 2\pi r \, [\nabla \cdot (\nabla \phi \, \eta) - (\nabla \phi \cdot \nabla \eta)] \, \mathrm{d}z \, \mathrm{d}r = 0 \quad \forall \eta \in V. \tag{2.22}$$

Applying the Gauss divergence theorem on the first term, we have

$$\int_{\partial\Omega} \mu_0 \mu_r \, 2\pi r \, \nabla \phi \cdot \mathbf{n} \, \eta \, \mathrm{d}\sigma - \int_z \int_r \mu_0 \mu_r \, 2\pi r \, (\nabla \phi \cdot \nabla \eta) \, \mathrm{d}z \, \mathrm{d}r = 0 \quad \forall \eta \in V, \tag{2.23}$$

where $\mathbf{n}$ is the outward pointing unit normal vector to the surface. Since the test function η have to vanish on the part of boundary prescribed by Dirichlet boundary condition and considering the natural boundary condition (2.13) on the rest boundary, we get the symmetric weak form

$$\int_z \int_r \mu_0 \mu_r \, 2\pi r \, (\nabla \phi \cdot \nabla \eta) \, \mathrm{d}z \, \mathrm{d}r = 0 \quad \forall \eta \in V. \tag{2.24}$$

We now look at the discretization of the above axisymmetric weak formulation by finite element approximation. The function spaces S and V belong to the Sobolev space given as

$$H^1 = \left\{ \phi : \Omega \mapsto \mathbb{R} \,\middle|\, \int_\Omega |\phi|^2 + |\nabla \phi|^2 \, \mathrm{d}\mathbf{x} < \infty \right\}. \tag{2.25}$$

Let the solution space be

$$S = \{\phi \in H^1, \phi|_{\partial\Omega_D} = \overline{\phi}\}, \tag{2.26}$$

and the test functions space be

$$V = \{\eta \in H^1, \eta|_{\partial\Omega_D} = 0\}. \tag{2.27}$$

The approximation of ϕ and η through linear combinations of M shape functions $N_i(\mathbf{x})$ with $i = 1, ..., M$ is given as

$$\begin{aligned} \phi \approx \phi^h \text{ and } \nabla\phi \approx \nabla\phi^h, \\ \eta \approx \eta^h \text{ and } \nabla\eta \approx \nabla\eta^h. \end{aligned} \tag{2.28}$$

The approximate solutions ϕ^h and test functions η^h have to be chosen from the discrete function spaces

$$\begin{aligned} S^h &= \left\{ \phi^h \in S : \phi^h(\mathbf{x}) = \sum_{i=1}^{M} \phi_i N_i(\mathbf{x}),\ \phi_i \in \mathbb{R} \right\} \text{ and} \\ V^h &= \left\{ \eta^h \in V : \eta^h(\mathbf{x}) = \sum_{j=1}^{M} \eta_j N_j(\mathbf{x}),\ \eta_j \in \mathbb{R} \right\}. \end{aligned} \tag{2.29}$$

The shape functions $N_i(\mathbf{x})$ are chosen such that the approximations ϕ^h and η^h follow the continuity requirements and the prescribed boundary conditions. Inserting the approximations in Equation (2.24), we have

$$\int_z \int_r \sum_{i=1}^{M} \sum_{j=1}^{M} \mu_0\mu_r\ 2\pi r\ \phi_i\ \eta_j \Big(\nabla N_i(\mathbf{x}) \cdot \nabla N_j(\mathbf{x}) \Big)\ \mathrm{d}z\ \mathrm{d}r = 0 \quad \forall \eta_j \in V^h. \tag{2.30}$$

Applying the Gauss quadrature rule for numerical integration

$$\sum_q \sum_{i=1}^{M} \sum_{j=1}^{M} \mu_0\mu_r\ 2\pi r(q)\ (\nabla N_i(q) \cdot \nabla N_j(q))\ Jw(q)\ \phi_i(q) = 0, \tag{2.31}$$

where q are the quadrature points with the corresponding weights $w(q)$. Equation (2.31) is the final FE discretized axisymmetric formulation.

2.7 Input mesh generation

The input mesh for the axisymmetric (2.5D) geometry and the 3D geometry were created using the CUBIT Geometry and Mesh Generation Toolkit [13] developed and released by Sandia National Laboratories, USA.

The input structured grids were generated using quadrilateral (2D) and hexahedral (3D) mesh elements. Different material id's were set to the elements belonging to the free-space region (material id = 2) and the magneto-elastic material tube region (material_id = 1). The magnetic field was generated by applying a linearly varying potential function in a circular disk in 3D/rectangular box in 2D region (material_id = 3) at the center of the geometry.

Consider the Euclidean origin is on the left edge at the center (see Figure (2.2)) and the relative distances are measured from the origin. The major radius of torus membrane is 0.5. The minor inner edge radius of the torus membrane is 0.195 and the minor outer radius is 0.2. Thus, in modelling the thin membrane of magneto-elastic material we consider a toroid tube of finite thickness (0.005). The free space is of considerably large size (length = 5, height = 10) in order to have a uniform magnetic field in the region far away from the permanent magnet that generates this field.

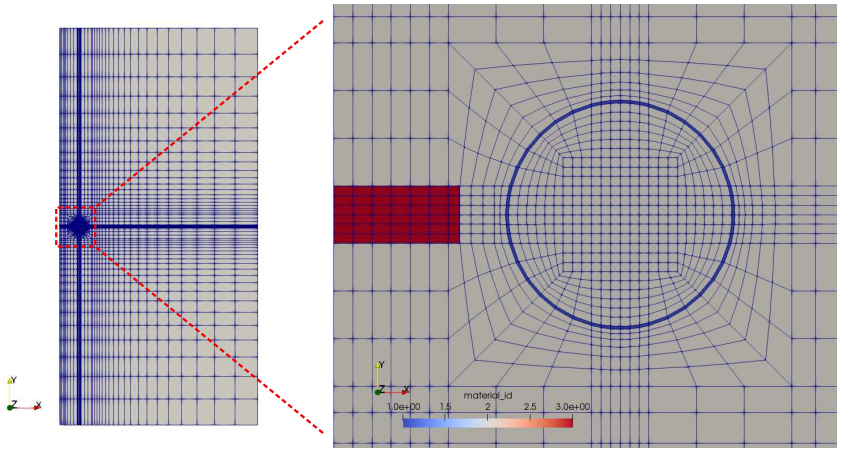

Figure 2.2: Axisymmetric (2.5D) mesh geometry of toroid tube material modelled with surrounding free space (Red region: permanent magnet, blue region: torus magneto-elastic material and remaining region is the free space)

2.8 Implementation details

The open-source, high performance finite element library deal.II [15, 39] is used to model and simulate the magneto-elastic material with the free space around the toroid tube. Trilinos [12] vectors, matrices, preconditioners and solvers are used. The use of class parallel::shared::Triangulation for automatic partitioning of the domain among all the involved MPI processes (in parallel context) is done. To perform adaptive h-/p-refinement of the coarse mesh for a certain number of refinement iterations we employ the class hp::DoFHandler to manage the distribution and enumeration of the degrees of freedom. In adaptive p-refinement we can have a different finite element on every cell of our mesh, whereas in h-refinement we can reduce the size of the mesh element where the error in solution is large. To mark the fraction of cells with largest error that would be then refined, we use the standard Kelly error estimator from the literature which is suitable and efficient for a large class of elliptic PDE's including the Laplace problem that we solve here.

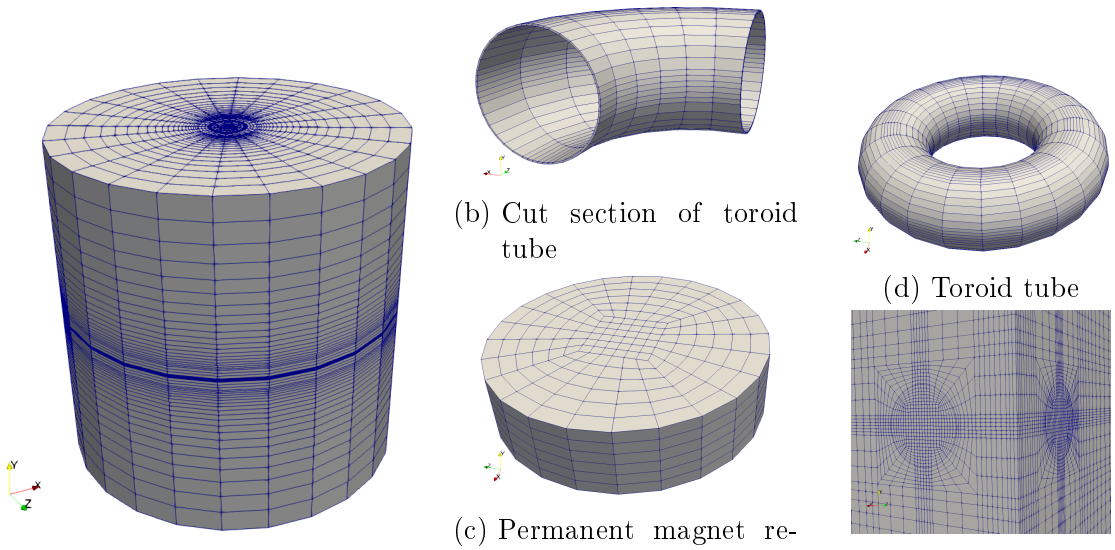

(a) 3D mesh with free space

(b) Cut section of toroid tube

(c) Permanent magnet region

(d) Toroid tube

(e) Zoomed cross-section

Figure 2.3: 3D mesh geometry

To generate a circulating magnetic field around the toroid tube we apply a linearly varying potential function to a region at the center of the body. This region of constrained degrees of freedom with the potential values has a shape of a rectangular box (in 2D), see the red box region in Figure (2.2) or circular disk (in 3D) at the center of the domain, see Figure (2.3c). The dimensions for this permanent magnet box/disk region to constrain the degrees of freedom and the linear potential function with which these DoFs will be constrained are user input parameters.

2.9 Numerical results

2.9.1 Validation of the axisymmetric formulation

In order to validate the results of the axisymmetric formulation with the 3D simulation results we compute and compare an energy metric (scalar) contained in the magneto-elastic toroid tube material. The energy is computed as

$$E = \sum_{cells \in \mathcal{B}_{tube}} \sum_{q} \frac{1}{2} \mu_0 \, \mu_r \, \alpha \, \| -\nabla \phi(q) \|^2 \, J \, w(q), \tag{2.32}$$

where α is the co-ordinate transformation scaling factor which has the value of $2\pi r$ for the axisymmetric formulation (2.5D) and 1 for the 3D simulation.

We observe the total energy in the magneto-elastic membrane due to the applied magneto-static magnetic scalar potential for the axisymmetric formulation for 4 refinement cycles in Figure (2.4a) and for the 3D simulation for 3 refinement cycles in Figure

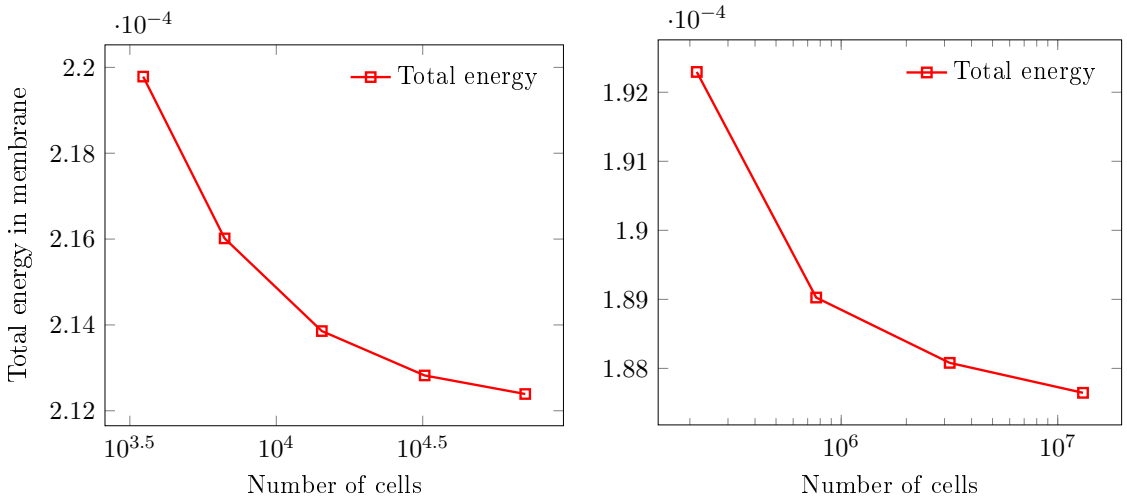

(a) Axisymmetric formulation (b) 3D simulation

Figure 2.4: Total energy in the magneto-elastic toroid membrane for each refinement cycle

(2.4b) (less number of refinement cycles due to memory bottleneck with vastly growing number of cells). Four MPI processes were employed to obtain the results. As can be observed, the total energy by both the approaches are comparable with a maximum relative error of 15%. We observe a convergence in the total energy with each h-adaptive mesh refinement cycle. High computational cost for the 3D simulation is clearly observable when comparing the number of cells in the domain against the number of cells in axisymmetric (2.5D) simulation result.

2.9.2 Experiment with the permanent magnet region and the applied potential

We carried out a study on the size of the permanent magnet region in which we constrain the degrees of freedom to a linearly varying magnetic potential. This region, as explained earlier, is a rectangular box in 2D/circular disk in 3D. In addition to studying the behaviour of results on the dependence of the size of this magnet region, we also experimented with the change in the linear potential function values. The magnet region dimensions (length and height) and the potential function to apply are user input parameters and are varied in this study. This experiment was carried out for the axisymmetric (2.5D) model only.

In the above figures we observe the resulting magnetic field $\mathbb{h}$ for the input magnet region and applied magnetic potential parameters. Figure (2.5d) has double the magnet size when compared to the magnet size in Figure (2.5a). When comparing the results for this effect of increased magnet size, we observe in Figure (2.5e) an increase in the

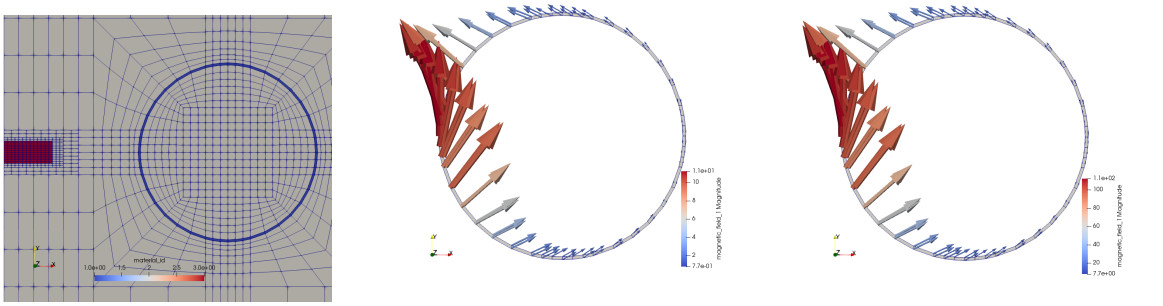

(a) Magnet x=0.11,y=0.0255 (red block)

(b) Pot. diff.= 1000 Max. h= 1.1e+01, Min. h= 7.7e-01

(c) Pot. diff.= 10000 Max. h= 1.1e+02, Min. h= 7.7e+00

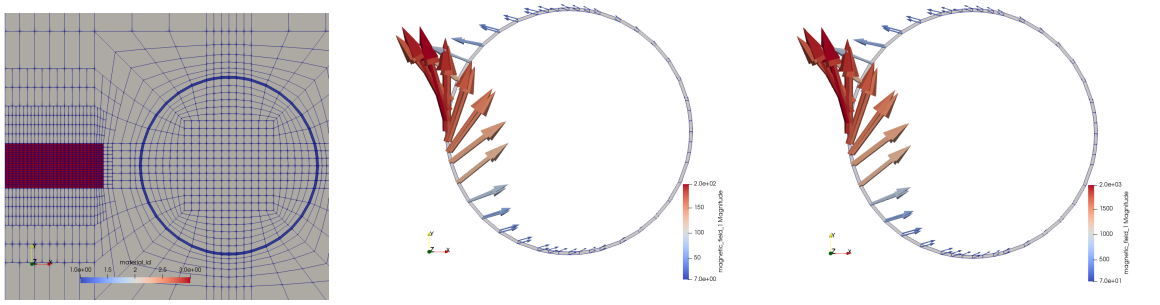

(d) Magnet x=0.22,y=0.051 (red block)

(e) Pot. diff.= 1000 Max. h= 2.0e+02, Min. h= 7.0e+00

(f) Pot. diff.= 10000 Max. h= 2.0e+03, Min. h= 7.0e+01

Figure 2.5: Effect of magnet size and applied magnetic potential in torus membrane field

magnitude of the magnetic field against the result in Figure (2.5b). In Figure (2.5c) we increase the applied magnetic potential ten times of that used in the result for Figure (2.5b) keeping the size of the permanent magnet region the same. We observe the magnetic field has proportionally increased by same magnitude. Combined increase in the magnet region (twice as original size) and magnetic potential (ten times the original value) we observe the magnetic field has increased by a significantly large magnitude, see Figure (2.5f). It is important to observe that the direction of magnetic field near the torus membrane did not change in any of the variation case. The aim of this study is to find appropriate values for the above three parameters such that we have a tangential magnetic field in the torus membrane to satisfy the curl free condition as given in Equation (2.2).

The results with appropriately chosen values of these parameters for future work are depicted in Figure (2.6) and (2.7).

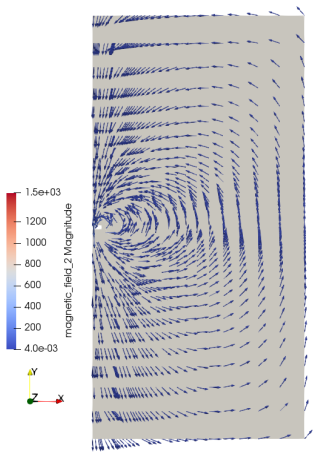

(a) Magnetic field in free space

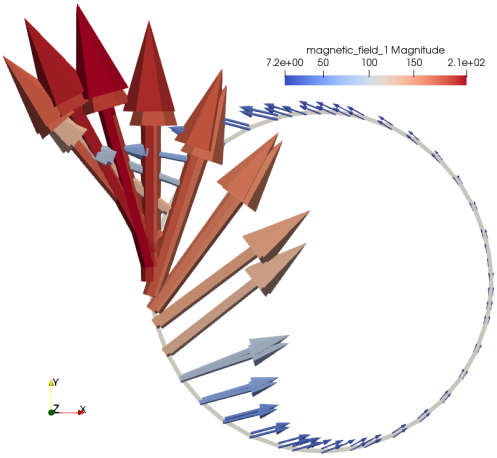

(b) Magnetic field in torus membrane

Figure 2.6: Axisymmetric (2.5D) formulation

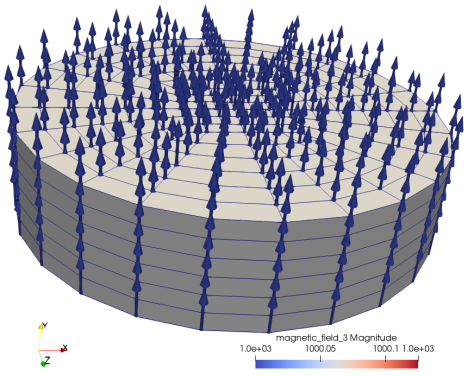

(a) Magnetic field in permanent magnet

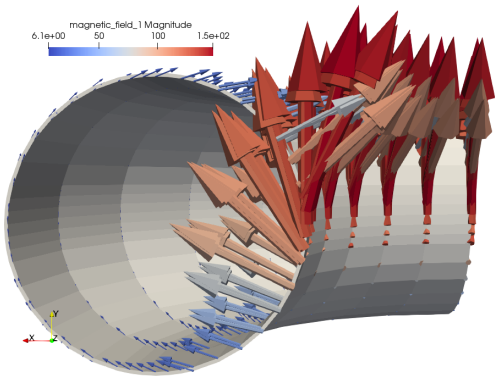

(b) Magnetic field in torus membrane

Figure 2.7: 3D simulation

3 Quasi-static finite-strain compressible elasticity

3.1 Kinematics

Consider a continuum body $\mathcal{B}_0$ in a three dimensional Euclidean space. Let any point in this reference configuration $\mathcal{B}_0$ be identified by the position vector $\mathbf{X}$. The configuration after some time $t > 0$ is termed as deformed configuration $\mathcal{B}_t$ and the corresponding position vector $\mathbf{x}$ is given by a non-linear one-to-one deformation map $\mathbf{x} = \boldsymbol{\varphi}(\mathbf{X}, t)$. The material description of the displacement of the particle at the position $\mathbf{X}$ is defined as

$$\mathbf{u}(\mathbf{X}, t) := \mathbf{x}(\mathbf{X}, t) - \mathbf{X}. \tag{3.1}$$

A tensor $\mathbf{F}$ which describes the deformation process locally relates the tangent vectors of reference and current configuration to each other. It maps a material line element of the reference configuration $\mathbf{dX}$ in $\mathcal{B}_0$ to a line element $\mathbf{dx}$ in $\mathcal{B}_t$ as

$$\mathbf{dx} = \mathbf{F} \cdot \mathbf{dX}. \tag{3.2}$$

This tensor $\mathbf{F}$ is called the deformation gradient and is the material gradient of the motion defined as

$$\mathbf{F}(\mathbf{X}, t) := \frac{\partial \boldsymbol{\varphi}(\mathbf{X}, t)}{\partial \mathbf{X}} = \nabla_0 \mathbf{x}(\mathbf{X}, t) = \mathbf{I} + \nabla_0 \mathbf{u}. \tag{3.3}$$

The gradient w.r.t. the reference configuration $\mathcal{B}_0$ is denoted as ∇_0 and the gradient w.r.t. the deformed configuration $\mathcal{B}_t$ be denoted as ∇ and are related as

$$\nabla\{\cdot\} = \frac{\partial\{\cdot\}}{\partial \mathbf{x}} = \frac{\partial\{\cdot\}}{\partial \mathbf{X}} \cdot \frac{\partial \mathbf{X}}{\partial \mathbf{x}} = \nabla_0\{\cdot\} \cdot \mathbf{F}^{-1}. \tag{3.4}$$

The transformation of surface area elements between $\mathcal{B}_0$ and $\mathcal{B}_t$ is given by the **Nanson's formula**

$$\mathbf{da} = \mathbf{n} \cdot \mathrm{d}a = J\ \mathbf{F}^{-T} \cdot \mathbf{N}\mathrm{d}A = J\ \mathbf{F}^{-T} \cdot \mathbf{dA}, \tag{3.5}$$

where $\mathbf{n}$ is the normal vector of the surface in $\mathcal{B}_t$, $\mathbf{N}$ is the normal vector in $\mathcal{B}_0$ and $\mathrm{d}a$ and $\mathrm{d}A$ are the corresponding area elements. The determinant of the deformation gradient,

known as the Jacobian, $J(\mathbf{X},t) := \det\mathbf{F}(\mathbf{X},t) > 0$ (non-negative to avoid material self-penetration) maps the volume elements in material and spatial configurations $\mathrm{d}V$ and $\mathrm{d}v$, respectively as

$$\mathrm{d}v = J(\mathbf{X},t)\ \mathrm{d}V. \tag{3.6}$$

The strain tensor in the material configuration $\mathcal{B}_0$ is defined as

$$\mathbf{E} := \frac{1}{2}(\mathbf{F}^T\cdot\mathbf{F} - \mathbf{I}) = \frac{1}{2}(\mathbf{C} - \mathbf{I}), \tag{3.7}$$

and is called as the Green-Lagrange strain tensor. The tensor $\mathbf{C} := \mathbf{F}^T\cdot\mathbf{F}$ is known as the right Cauchy-Green deformation tensor which expresses the square of the line element $\mathbf{dx}$ by the material line element $\mathbf{dX}$ as $\mathbf{dx}\cdot\mathbf{dx} = \mathbf{dX}\cdot\mathbf{C}\cdot\mathbf{dX}$. $\mathbf{C}$ is *symmetric* and *positive definite* at each $\mathbf{X}\in\mathcal{B}_0$. Thus the Green-Lagrange strain $\mathbf{E}$ is also symmetric. The strain $\mathbf{E}$ describes the change of the square of the line elements from $\mathcal{B}_0$ to $\mathcal{B}_t$. Using the definition of $\mathbf{F}$ from Equation (3.3), we can express the Green-Lagrange strain in terms of the displacement gradient as

$$\mathbf{E} = \frac{1}{2}(\nabla_0\mathbf{u} + [\nabla_0\mathbf{u}]^T + [\nabla_0\mathbf{u}]^T\cdot\nabla_0\mathbf{u}). \tag{3.8}$$

3.2 Kinetics

The Cauchy stress theorem states that the Cauchy traction $\mathbf{t}$ acting on an infinitesimal surface element $\mathrm{d}a$ in the current configuration $\mathcal{B}_t$ is the product of the Cauchy stress tensor $\boldsymbol{\sigma}$, a spatial quantity, and the outward unit normal vector to the surface $\mathrm{d}a$ as

$$\mathbf{t}(\mathbf{x},t,\mathbf{n}) = \boldsymbol{\sigma}(\mathbf{x},t)\cdot\mathbf{n}. \tag{3.9}$$

Following the result of balance of angular momentum, it is known that the Cauchy stress tensor is symmetric. Similar relation in the material configuration is given as

$$\mathbf{T}(\mathbf{X},t,\mathbf{N}) = \mathbf{P}(\mathbf{X},t)\cdot\mathbf{N}, \tag{3.10}$$

where $\mathbf{T}$ is the first Piola-Kirchhoff traction acting on an infinitesimal surface element $\mathrm{d}A$ and $\mathbf{P}$ is the first Piola-Kirchhoff stress tensor. $\mathbf{P}$ is a two-point tensor indicating that it is neither a material or a spatial quantity. The first Piola-Kirchhoff stress tensor is related to the Cauchy stress tensor as

$$\mathbf{P} = J\ \boldsymbol{\sigma}\cdot\mathbf{F}^{-T}. \tag{3.11}$$

The Cauchy traction $\mathbf{t}$ and the first Piola-Kirchhoff traction $\mathbf{T}$ are related as

$$\mathbf{T}\ \mathbf{dA} = \mathbf{t}\ \mathbf{da}, \tag{3.12}$$

such that

$$\int_{\mathcal{B}_0} [\mathbf{P}\cdot\mathbf{N}]\,\mathrm{d}A = \int_{\mathcal{B}_0} \left[J\,\boldsymbol{\sigma}\cdot\mathbf{F}^{-T}\right]\cdot\mathbf{N}\,\mathrm{d}A = \int_{\mathcal{B}_0} \boldsymbol{\sigma}\cdot\left[J\,\mathbf{F}^{-T}\cdot\mathbf{N}\right]\mathrm{d}A \overset{\text{Nanson's}}{=} \int_{\mathcal{B}_t} \boldsymbol{\sigma}\cdot\mathbf{n}\,\mathrm{d}a. \tag{3.13}$$

A completely material stress measure is also introduced known as the second Piola-Kirchhoff stress tensor given as

$$\mathbf{S} = \mathbf{F}^{-1}\cdot\mathbf{P}. \tag{3.14}$$

The second Piola-Kirchhoff stress tensor is symmetric tensor.

3.3 Constitutive material model

The kinematical relations and balance laws are not sufficient to solve a boundary value or initial value problem. For a complete set of equations, a constitutive equation needs to be formulated which can appropriately characterize the material response of a body.

Hyperelastic materials are the purely elastic material behaviour under the assumption of the so-called Green elasticity. The material response is characterised by a Helmholtz free energy function $\Psi = \Psi(\mathbf{F}) = \Psi(\mathbf{C})$ which serves as a potential for the stress. Ψ describes the strain energy stored in the body and hence also known as the strain energy function (S.E.F.). When S.E.F. is described in terms of the right Cauchy-Green tensor $\mathbf{C}$ then the isotropic hyperelastic material response is

$$\mathbf{S} = 2\frac{\partial\Psi(\mathbf{C})}{\partial\mathbf{C}}. \tag{3.15}$$

A Neo-Hookean solid is a hyperelastic material model that can be used for predicting the non-linear behaviour of materials undergoing large deformations under loads. The Neo-Hookean material model is usable for plastics and rubber-like materials. The S.E.F. corresponding to a compressible Neo-Hookean material is given as

$$\Psi \equiv \frac{\mu}{2}[\mathbf{C}:\mathbf{I} - \mathbf{I}:\mathbf{I} - 2\ln J] + \frac{\lambda}{2}(\ln J)^2, \tag{3.16}$$

where μ and λ are the Lamé parameters. For the considered S.E.F. for the Neo-Hookean material as stated in Equation (3.16), the second Piola-Kirchhoff stress is

$$\mathbf{S} = 2\left\{\frac{\mu}{2}\left[\frac{\partial(\mathbf{C}:\mathbf{I})}{\partial\mathbf{C}} - 0 - 2\frac{\partial\ln J}{\partial\mathbf{C}}\right] + \frac{\lambda}{2}\frac{\partial(\ln J)^2}{\partial\mathbf{C}}\right\}. \tag{3.17}$$

Employing the chain rule for the intermediate partial derivatives

$$\frac{\partial(\mathbf{C}:\mathbf{I})}{\partial\mathbf{C}} = \mathbf{I}, \tag{3.18}$$

$$\frac{\partial\ln J}{\partial\mathbf{C}} = \frac{1}{J}\frac{\partial J}{\partial\mathbf{C}}, \tag{3.19}$$

$$\frac{\partial(\ln J)^2}{\partial\mathbf{C}} = 2\frac{\partial\ln J}{\partial\mathbf{C}} = 2\frac{1}{J}\frac{\partial J}{\partial\mathbf{C}}. \tag{3.20}$$

The partial derivative of the Jacobian w.r.t. the right Cauchy-Green deformation tensor is given as [see 17, page 46 Equation (3.124)]

$$\frac{\partial J}{\partial \mathbf{C}} = \frac{1}{2}\, J\, \mathbf{C}^{-1}. \tag{3.21}$$

Rearranging the terms with the use of the results from Equations (3.18) to (3.20) and Equation (3.21), we have

$$\mathbf{S} = \mu \mathbf{I} - [\mu - \lambda \ln J]\, \mathbf{C}^{-1}. \tag{3.22}$$

The fourth-order elasticity tensor in the material description is defined as

$$\mathfrak{C} := 2\frac{\partial \mathbf{S}(\mathbf{C})}{\partial \mathbf{C}} = 4\frac{\partial^2 \Psi(\mathbf{C})}{\partial \mathbf{C} \otimes \partial \mathbf{C}}. \tag{3.23}$$

Using the derived form for the second Piola-Kirchhoff stress from Equation (3.22), we have

$$\mathfrak{C} = [2\lambda \ln J - 2\mu]\, \frac{\partial \mathbf{C}^{-1}}{\partial \mathbf{C}} + \lambda \mathbf{C}^{-1} \otimes \mathbf{C}^{-1}, \tag{3.24}$$

with the standard result [see 17, page 519]

$$\frac{\partial C^{-1}_{IJ}}{\partial C_{KL}} := \frac{-1}{2}\left[C^{-1}_{IK}\, C^{-1}_{LJ} + C^{-1}_{IL}\, C^{-1}_{KJ}\right]. \tag{3.25}$$

The fourth-order elasticity tensor for hyperelastic materials possess both major and minor symmetries, i.e. $\mathfrak{C} = C_{IJKL} = C_{KLIJ} = C_{JIKL} = C_{IJLK}$.

3.4 Weak formulation in the referential configuration

For the analysis of (non-)linear initial boundary value problems in continuum theory, a coupled system of partial differential equations needs to be solved consisting of kinematical relations, the local balance law of linear momentum and the constitutive equations. The description of the strong form of these equations, here, will be with respect to the initial configuration of the bodies.

$$\begin{aligned} \text{Kinematics}: &\quad \mathbf{F},\ \mathbf{E} = \frac{1}{2}(\mathbf{F}^T \cdot \mathbf{F} - \mathbf{I}), \\ \text{Equilibrium}: &\quad \mathrm{Div}(\mathbf{F} \cdot \mathbf{S}) + \mathbf{b}^p = \mathbf{0}, \\ \text{Constitutive equation}: &\quad \mathbf{S} = 2\frac{\partial \Psi}{\partial \mathbf{C}}. \end{aligned}$$

In addition the boundary conditions for the displacements have to be imposed on $\partial\mathcal{B}_{0,u}$ and for tractions on the boundary $\partial\mathcal{B}_{0,t}$, with $\partial\mathcal{B}_{0,u} \cap \partial\mathcal{B}_{0,t} = \emptyset$.

$$\text{Boundary conditions}: \quad \mathbf{u} = \mathbf{u}^p \text{ on } \partial\mathcal{B}_{0,u} \ \&\ \mathbf{F} \cdot \mathbf{S} \cdot \mathbf{N} = \mathbf{t}^p \text{ on } \partial\mathcal{B}_{0,t}.$$

$\mathbf{b}^p$ is the prescribed body force and $\mathbf{t}^p$ is the prescribed traction force per unit area. The finite element method, which is based on a variational formulation of the equations, can be fulfilled in a weak sense minimizing the error of the finite element approximation for arbitrarily chosen test functions. Let $\mathbf{u}^h$ be the approximation of the exact solution $\mathbf{u}$. Since the approximate solution is usually not the same as the exact solution, an error $\mathbf{R}$ will occur when satisfying the strong form of the above equations.

$$\mathrm{Div}(\mathbf{F}(\mathbf{u}^h) \cdot \mathbf{S}) + \mathbf{b}^p = \mathbf{R}. \tag{3.26}$$

The error $\mathbf{R}$ will be minimized in a weak sense by multiplying the residual by a vector-valued weighting function $\boldsymbol{\eta}$ and integrating the residual over the whole domain. This vector-valued function $\boldsymbol{\eta}$ is called as test function. Thus, we have

$$\int_{\mathcal{B}_0} \mathrm{Div}(\mathbf{F} \cdot \mathbf{S}) \cdot \boldsymbol{\eta} \, \mathrm{d}V + \int_{\mathcal{B}_0} \mathbf{b}^p \cdot \boldsymbol{\eta} \, \mathrm{d}V = 0 \quad \forall \boldsymbol{\eta}. \tag{3.27}$$

By doing integration by parts of the first term in Equation (3.27), with the application of divergence theorem and the boundary conditions for displacement and traction, we have the weak form as

$$\int_{\mathcal{B}_0} \mathbf{F} \cdot \mathbf{S} \cdot \nabla_0 \boldsymbol{\eta} \, \mathrm{d}V - \int_{\mathcal{B}_0} \mathbf{b}^p \cdot \boldsymbol{\eta} \, \mathrm{d}V - \int_{\partial \mathcal{B}_{0,t}} \mathbf{t}^p \cdot \boldsymbol{\eta} \, \mathrm{d}A = 0 \quad \forall \boldsymbol{\eta}. \tag{3.28}$$

Simplifying the first term in Equation (3.28) using the fact that the scalar product of a symmetrical tensor with an anti-symmetrical tensor is zero, we have

$$\mathbf{F} \cdot \mathbf{S} \cdot \nabla_0 \boldsymbol{\eta} = \mathbf{S} \cdot \mathbf{F}^T \cdot \nabla_0 \boldsymbol{\eta} = \mathbf{S} \cdot \frac{1}{2}(\mathbf{F}^T \cdot \nabla_0 \boldsymbol{\eta} + \nabla_0^T \boldsymbol{\eta} \cdot \mathbf{F}) = \mathbf{S} \cdot \delta\mathbf{E}. \tag{3.29}$$

$\delta\mathbf{E}$ denotes the variation of the Green-Lagrange strain tensor which is obtained as the directional derivative

$$\begin{aligned}
D\mathbf{E} \cdot \boldsymbol{\eta} &= \frac{1}{2} \frac{\mathrm{d}}{\mathrm{d}\alpha} \left[\mathbf{F}^T(\boldsymbol{\varphi} + \alpha\boldsymbol{\eta}) \cdot \mathbf{F}(\boldsymbol{\varphi} + \alpha\boldsymbol{\eta}) - \mathbf{I} \right] \Big|_{\alpha=0} \\
&= \frac{1}{2} \left[\frac{\partial \mathbf{F}^T(\boldsymbol{\varphi} + \alpha\boldsymbol{\eta})}{\partial \alpha} \cdot \mathbf{F}(\boldsymbol{\varphi} + \alpha\boldsymbol{\eta}) + \mathbf{F}^T(\boldsymbol{\varphi} + \alpha\boldsymbol{\eta}) \cdot \frac{\partial \mathbf{F}(\boldsymbol{\varphi} + \alpha\boldsymbol{\eta})}{\partial \alpha} - \frac{\partial \mathbf{I}}{\partial \alpha} \right] \Big|_{\alpha=0} \\
&= \frac{1}{2} \left[\frac{\partial \left[\mathbf{I} + \nabla_0^T(\boldsymbol{\varphi} + \alpha\boldsymbol{\eta}) \right]}{\partial \alpha} \cdot \mathbf{F}(\boldsymbol{\varphi} + \alpha\boldsymbol{\eta}) + \mathbf{F}^T(\boldsymbol{\varphi} + \alpha\boldsymbol{\eta}) \cdot \frac{\partial \left[\mathbf{I} + \nabla_0(\boldsymbol{\varphi} + \alpha\boldsymbol{\eta}) \right]}{\partial \alpha} - \mathbf{0} \right] \Big|_{\alpha=0} \\
&\overset{\alpha=0}{=} \frac{1}{2} \left[(\nabla_0 \boldsymbol{\eta})^T \cdot \mathbf{F}(\boldsymbol{\varphi}) + \mathbf{F}^T(\boldsymbol{\varphi}) \cdot \nabla_0 \boldsymbol{\eta} \right] = \delta\mathbf{E}.
\end{aligned} \tag{3.30}$$

Using the result of Equation (3.29) and Equation (3.30) in Equation (3.28), we have

$$G(\boldsymbol{\varphi}, \boldsymbol{\eta}) := \int_{\mathcal{B}_0} \mathbf{S} \cdot \delta\mathbf{E} \, \mathrm{d}V - \int_{\mathcal{B}_0} \mathbf{b}^p \cdot \boldsymbol{\eta} \, \mathrm{d}V - \int_{\partial \mathcal{B}_{0,t}} \mathbf{t}^p \cdot \boldsymbol{\eta} \, \mathrm{d}A = 0 \quad \forall \boldsymbol{\eta}. \tag{3.31}$$

The first term in Equation (3.31) denotes the internal virtual work performed by the body. The last two terms are the virtual work of the applied traction and the inertia load.

3.4.1 Variational principles

Principle of stationary potential energy: The S.E.F. for the considered hyperelastic material model describes the stored energy in the continuum body. Based on this S.E.F. we can find the equilibrium configuration by the principle of minimum potential energy. The total potential energy of the system Π is the sum of the internal and external potential energies and is defined as

$$\Pi = \Pi_{int} + \Pi_{ext}, \tag{3.32}$$

where

$$\Pi_{int} = \int_{\mathcal{B}_0} \Psi(\mathbf{C}) \, \mathrm{d}V, \tag{3.33}$$

$$\Pi_{ext} = -\int_{\mathcal{B}_0} \mathbf{b}^p \cdot \boldsymbol{\varphi} \, \mathrm{d}V - \int_{\partial\mathcal{B}_{0,t}} \mathbf{t}^p \cdot \boldsymbol{\varphi} \, \mathrm{d}A. \tag{3.34}$$

The value of $\boldsymbol{\varphi}$ which makes Π stationary satisfies the equilibrium configuration, i.e. find $\boldsymbol{\varphi}$ such that $\min_{\boldsymbol{\varphi}} \Pi \rightarrow \text{stat.}$. The stationary value of Equation (3.32) is found by the variation of Π w.r.t. the deformation

$$\begin{aligned} \delta\Pi = D\Pi \cdot \boldsymbol{\eta} = \frac{\partial \Pi}{\partial \mathbf{u}} \cdot \delta\mathbf{u} =: R(\mathbf{u}; \delta\mathbf{u}) \\ = \int_{\mathcal{B}_0} \frac{\partial \Psi(\mathbf{C})}{\partial \mathbf{C}} \cdot D\mathbf{C} \cdot \boldsymbol{\eta} \, \mathrm{d}V - \int_{\mathcal{B}_0} \mathbf{b}^p \cdot \delta\mathbf{u} \, \mathrm{d}V - \int_{\partial\mathcal{B}_{0,t}} \mathbf{t}^p \cdot \delta\mathbf{u} \, \mathrm{d}A = 0 \end{aligned} \tag{3.35}$$

with

$$\frac{\partial \Psi(\mathbf{C})}{\partial \mathbf{C}} = \frac{1}{2}\mathbf{S} \quad \text{and} \quad D\mathbf{C} \cdot \boldsymbol{\eta} = 2 \, D\mathbf{E} \cdot \boldsymbol{\eta} = 2\delta\mathbf{E} \tag{3.36}$$

$$R(\mathbf{u}; \delta\mathbf{u}) = \delta\Pi = \int_{\mathcal{B}_0} \mathbf{S} \cdot \delta\mathbf{E} \, \mathrm{d}V - \int_{\mathcal{B}_0} \mathbf{b}^p \cdot \delta\mathbf{u} \, \mathrm{d}V - \int_{\partial\mathcal{B}_{0,t}} \mathbf{t}^p \cdot \delta\mathbf{u} \, \mathrm{d}A = 0. \tag{3.37}$$

Hence the variational form $R(\mathbf{u}; \delta\mathbf{u})$ in Equation (3.37) is equivalent to the weak form $G(\boldsymbol{\varphi}, \boldsymbol{\eta})$ in Equation (3.31) when the material energy is defined by a strain energy function.

3.5 Linearisation

The variational form R in Equation (3.37) is a non-linear equation. Geometrical non-linearity occurs due to the non-linear Green-Lagrange strain tensor. Linearisations of the associated non-linear terms is necessary in the algorithmic treatment of the solution process for the non-linear boundary value problems. Assuming the state of the system is known at some load or time step t_{n-1}, the linearisation of the non-linear residual R by an iterative solution method (such as Newton-Raphson) is given as:
Find increment $\Delta\mathbf{u}$ such that

$$\mathbf{L}\left[R\right]_{\mathbf{u}_{i+1}=\mathbf{u}_i+\Delta\mathbf{u}_i} = R(\mathbf{u}_i)+D_{\Delta\mathbf{u}}R(\mathbf{u}_i;\delta\mathbf{u})\cdot\Delta\mathbf{u} = R(\mathbf{u}_i)+D^2_{\Delta\mathbf{u},\delta\mathbf{u}}\Pi(\mathbf{u}_i)\cdot\Delta\mathbf{u} = 0, \quad (3.38)$$

where, the value of a quantity at the current iteration i under an iterative solver regime is denoted as $\{\cdot\}^n_i = \{\cdot\}_i$ at the currently unknown state t_n (i.e. the load or time step at n). The incremental change between iterative solver iterations i and $i+1$ is denoted as $\Delta\{\cdot\} := \{\cdot\}_{i+1} - \{\cdot\}_i$.

After a certain convergence criteria is reached at each Newton step, we update the solution at the current load step t_n as $\mathbf{u}_{i+1} = \mathbf{u}_i + \Delta\mathbf{u}$. The tangent matrix $\mathbf{K}$ in Equation (3.38) is given as

$$D^2_{\Delta\mathbf{u},\delta\mathbf{u}}\Pi(\mathbf{u}_i) = D_{\Delta\mathbf{u}}R(\mathbf{u}_i;\delta\mathbf{u})\cdot\Delta\mathbf{u} =: \mathbf{K}(\mathbf{u}_i;\Delta\mathbf{u},\delta\mathbf{u}). \quad (3.39)$$

Assuming dead loading for the sake of simplicity to derive the tangent matrix, i.e. the body load and traction do not change due to the deformation of the body, we have

$$\mathbf{K}(\mathbf{u}_i;\Delta\mathbf{u},\delta\mathbf{u}) = \int_{\mathcal{B}_0} D_{\Delta\mathbf{u}}\left[\mathbf{S}\cdot\delta\mathbf{E}\right]\cdot\Delta\mathbf{u}\,\mathrm{d}V. \quad (3.40)$$

The kinematical quantity Green-Lagrange strain $\mathbf{E}$ and the constitutive relation quantity second Piola-Kirchhoff stress tensor $\mathbf{S}$ are non-linear tensors. In order to form a system of linear equations from Equation (3.40) and the solution of it, we require the linearised forms of the non-linear terms $\mathbf{E}$ and $\mathbf{S}$.

3.5.1 Basic concept of linearisation process

To demonstrate the basic idea of linearisations for non-linear problems, consider a non-linear C^1 mapping $\mathbf{G}:\mathcal{E}\mapsto\mathcal{F}$, where $\overline{\mathbf{x}}$ and $\Delta\mathbf{x}$ are points of the abstract space $\mathcal{E}$. The elements of the spaces $\mathcal{E}$ and $\mathcal{F}$ can be scalar-, vector- or tensor-fields. The Taylor series expansion of this mapping about a point $\overline{\mathbf{x}}+\Delta\mathbf{x}$ is given as

$$\mathbf{G}(\overline{\mathbf{x}}+\Delta\mathbf{x}) = \mathbf{G}(\overline{\mathbf{x}}) + D\mathbf{G}(\overline{\mathbf{x}})\cdot\Delta\mathbf{x} + \mathbf{R}. \quad (3.41)$$

The term $\mathbf{R}$ refers to the higher-order truncated terms. The linear part of the mapping $\mathbf{G}$ at $\overline{\mathbf{x}}$ is

$$\mathbf{L}\left[\mathbf{G}\right]_{\mathbf{x}=\overline{\mathbf{x}}} = \mathbf{G}(\overline{\mathbf{x}}) + D\mathbf{G}(\overline{\mathbf{x}})\cdot\Delta\mathbf{x}. \quad (3.42)$$

Thus, the first-order Taylor series expansion corresponds to the linearisation of the weak form in the finite element applications.

3.5.2 Linearisation of kinematical quantity

The linearisation of the variation of Green-Lagrange strain tensor is

$$\mathbf{L}\left[\mathbf{E}\right] = \mathbf{E}(\overline{\boldsymbol{\varphi}}) + D\mathbf{E}(\boldsymbol{\varphi}) \cdot \Delta\mathbf{u}, \tag{3.43}$$

where the directional derivative in the direction of increment $\Delta\mathbf{u}$ is given as in the result of Equation (3.30)

$$D\mathbf{E}(\boldsymbol{\varphi}) \cdot \Delta\mathbf{u} = \frac{1}{2}\left[\Delta(\nabla_0^T\mathbf{u}) \cdot \mathbf{F} + \mathbf{F}^T \cdot \Delta(\nabla_0\mathbf{u})\right] = \Delta\mathbf{E}, \tag{3.44}$$

with $\Delta\mathbf{E}$ being the increment of the Green-Lagrange deformation tensor.

3.5.3 Linearisation of constitutive equation

The constitutive equation for the hyperelastic Neo-Hookean material model in Section 3.3 was derived in terms of the right Cauchy-Green deformation tensor $\mathbf{C}$ and thus the second Piola-Kirchhoff stress tensor also depends on $\mathbf{C}$. The linearisation of $\mathbf{S}$ is

$$\begin{aligned}\mathbf{L}\left[\mathbf{S}\right]_{\boldsymbol{\varphi}=\overline{\boldsymbol{\varphi}}} &= \mathbf{S}(\overline{\boldsymbol{\varphi}}) + D\mathbf{S}(\boldsymbol{\varphi}) \cdot \Delta\mathbf{u} \\ &= \mathbf{S}(\overline{\boldsymbol{\varphi}}) + \frac{\partial\mathbf{S}}{\partial\mathbf{C}}\Big|_{\boldsymbol{\varphi}=\overline{\boldsymbol{\varphi}}} : \left[D\mathbf{C}(\overline{\boldsymbol{\varphi}}) \cdot \Delta\mathbf{u}\right].\end{aligned} \tag{3.45}$$

Using the results of Equation (3.23) and Equation (3.36) in Equation (3.45), we get

$$\mathbf{L}\left[\mathbf{S}\right]_{\boldsymbol{\varphi}=\overline{\boldsymbol{\varphi}}} = \mathbf{S}(\overline{\boldsymbol{\varphi}}) + \mathfrak{C}(\overline{\boldsymbol{\varphi}}) : \left[\Delta\mathbf{E}(\overline{\boldsymbol{\varphi}})\right]. \tag{3.46}$$

The first term in Equation (3.46) is Equation (3.29) with $\mathbf{F}$ and $\mathbf{S}$ evaluated at the fixed point $\overline{\boldsymbol{\varphi}}$ instead of $\boldsymbol{\varphi}$. With the assumption that the applied load is conservative, the directional derivative in Equation (3.38) can be computed by taking only the first term in Equation (3.29) into account

$$\begin{aligned}D_{\Delta\mathbf{u}}R(\mathbf{u}_i;\Delta\mathbf{u}) \cdot \Delta\mathbf{u} &= \int_{\mathcal{B}_0} \left[D\{\mathbf{F}(\overline{\boldsymbol{\varphi}}) \cdot \mathbf{S}(\overline{\boldsymbol{\varphi}})\} \cdot \Delta\mathbf{u}\right] \cdot \nabla_0\delta\mathbf{u}\, \mathrm{d}V \quad \forall\delta\mathbf{u} \\ &= \int_{\mathcal{B}_0} \left\{\nabla_0(\Delta\mathbf{u}) \cdot \mathbf{S}(\overline{\boldsymbol{\varphi}}) + \mathbf{F}(\overline{\boldsymbol{\varphi}}) \cdot \left[D\mathbf{S}(\overline{\boldsymbol{\varphi}}) \cdot \Delta\mathbf{u}\right]\right\} \cdot \nabla_0\delta\mathbf{u}\, \mathrm{d}V \quad \forall\delta\mathbf{u}.\end{aligned} \tag{3.47}$$

The directional derivative of $\mathbf{S}$ at $\overline{\boldsymbol{\varphi}}$ as taken from the linearisation of constitutive equation in Equation (3.46) is

$$D\mathbf{S}(\overline{\boldsymbol{\varphi}}) \cdot \Delta\mathbf{u} = \mathfrak{C}(\overline{\boldsymbol{\varphi}}) : [\Delta\mathbf{E}(\overline{\boldsymbol{\varphi}})]\,, \tag{3.48}$$

where $\Delta\mathbf{E}$ is the linearisation of kinematical quantity from Equation (3.44) evaluated at the fixed point $\overline{\boldsymbol{\varphi}}$. Substituting Equation (3.48) in Equation (3.47) and by using the symmetry of $\mathfrak{C}$ along with the result of Equation (3.30), we have the final linearised form of the variational formulation as

$$D_{\Delta\mathbf{u}}R(\mathbf{u}_i;\Delta\mathbf{u})\cdot\Delta\mathbf{u} = \int_{\mathcal{B}_0} \Big\{\nabla_0(\Delta\mathbf{u})\cdot\mathbf{S}(\overline{\boldsymbol{\varphi}})\cdot\nabla_0\delta\mathbf{u} + \delta\mathbf{E}(\overline{\boldsymbol{\varphi}})\cdot\mathfrak{C}(\overline{\boldsymbol{\varphi}}) : [\Delta\mathbf{E}(\overline{\boldsymbol{\varphi}})]\Big\}\,\mathrm{d}V \quad \forall\delta\mathbf{u}. \tag{3.49}$$

The final linearised form is symmetric in $\delta\mathbf{u}$ and $\Delta\mathbf{u}$. The first term in Equation (3.49) is known as *the geometrical tangent* due to the direct appearance of stress at the given state. The second term is known as *the material tangent* since it contains along with the incremental constitutive tensor $\mathfrak{C}$, the variation $\delta\mathbf{E} := \frac{1}{2}\Big([\nabla_0\delta\mathbf{u}]^T\cdot\mathbf{F}(\overline{\boldsymbol{\varphi}})+\mathbf{F}^T(\overline{\boldsymbol{\varphi}})\cdot\nabla_0\delta\mathbf{u}\Big)$ and the increment $\Delta\mathbf{E} := \frac{1}{2}\Big([\nabla_0\Delta\mathbf{u}]^T\cdot\mathbf{F}(\overline{\boldsymbol{\varphi}}) + \mathbf{F}^T(\overline{\boldsymbol{\varphi}})\cdot\nabla_0\Delta\mathbf{u}\Big)$ of the Green-Lagrange strain tensor.

3.6 Discretization by the finite element method

For the considered linearised weak formulation at Newton increment i and time step t_n from Equation (3.38)

$$D_{\Delta\mathbf{u}}R(\mathbf{u}_i;\Delta\mathbf{u})\cdot\Delta\mathbf{u} = -R(\mathbf{u}_i), \tag{3.50}$$

with the tangent matrix and the residual evaluated at $\overline{\boldsymbol{\varphi}} = \boldsymbol{\varphi}(t_n, i)$ given by

$$D_{\Delta\mathbf{u}}R(\mathbf{u}_i;\Delta\mathbf{u})\cdot\Delta\mathbf{u} = \int_{\mathcal{B}_0} \Big\{\nabla_0(\Delta\mathbf{u})\cdot\mathbf{S}(\overline{\boldsymbol{\varphi}})\cdot\nabla_0\delta\mathbf{u} + \delta\mathbf{E}(\overline{\boldsymbol{\varphi}})\cdot[\mathfrak{C}(\overline{\boldsymbol{\varphi}}) : \Delta\mathbf{E}(\overline{\boldsymbol{\varphi}})]\Big\}\,\mathrm{d}V \quad \forall\delta\mathbf{u}$$

$$\text{and}\quad R(\mathbf{u}_i;\Delta\mathbf{u}) = \int_{\mathcal{B}_0}\mathbf{S}(\overline{\boldsymbol{\varphi}})\cdot\delta\mathbf{E}(\overline{\boldsymbol{\varphi}})\,\mathrm{d}V - \int_{\partial\mathcal{B}_{0,t}}\mathbf{t}^p\cdot\delta\mathbf{u}\,\mathrm{d}A,$$

we can now discretize it using the finite element approximation: find $\mathbf{u}\in\mathbf{W} = H^1_0(\mathcal{B}_0;\mathbb{R}^{\dim})$ such that for all $\delta\mathbf{u}\in\mathbf{V} = H^1(\mathcal{B}_0;\mathbb{R}^{\dim})$ it holds

$$\int_{\mathcal{B}_0} \Big\{\nabla_0(\Delta\mathbf{u})\cdot\mathbf{S}(\overline{\boldsymbol{\varphi}})\cdot\nabla_0\delta\mathbf{u} + \delta\mathbf{E}(\overline{\boldsymbol{\varphi}})\cdot[\mathfrak{C}(\overline{\boldsymbol{\varphi}}) : \Delta\mathbf{E}(\overline{\boldsymbol{\varphi}})]\Big\}\,\mathrm{d}V = -\int_{\mathcal{B}_0}\mathbf{S}(\overline{\boldsymbol{\varphi}})\cdot\delta\mathbf{E}(\overline{\boldsymbol{\varphi}})\,\mathrm{d}V + \int_{\partial\mathcal{B}_{0,t}}\mathbf{t}^p\cdot\delta\mathbf{u}\,\mathrm{d}A \quad \forall\delta\mathbf{u}. \tag{3.51}$$

The Sobolev space is given as

$$H^1 = \left\{ \mathbf{u} : \Omega \mapsto \mathbb{R} \middle| \int_\Omega \|\mathbf{u}\|^2 + \|\nabla \mathbf{u}\|^2 \, \mathrm{d}\Omega < \infty \right\}. \tag{3.52}$$

The vector-valued function spaces are given as

$$\mathbf{W} = \left\{ \mathbf{u} \in H^1, \mathbf{u}|_{\partial\Omega_D} = \overline{\mathbf{u}} \right\}, \tag{3.53}$$
$$\mathbf{V} = \left\{ \delta\mathbf{u} \in H^1, \delta\mathbf{u}|_{\partial\Omega_D} = \mathbf{0} \right\}. \tag{3.54}$$

The approximates in the discrete function spaces $\mathbf{W}^h \subset \mathbf{W}$ and $\mathbf{V}^h \subset \mathbf{V}$ is given as a linear combination of M vector-valued shape functions

$$\begin{aligned} \mathbf{W}^h &= \left\{ \mathbf{u}^h \in \mathbf{W} : \mathbf{u}^h(\mathbf{x}) = \sum_{I=1}^{M} u_I \, \mathbf{N}_I(\mathbf{x}), \; u_I \in \mathbb{R} \right\}, \\ \mathbf{V}^h &= \left\{ \delta\mathbf{u}^h \in \mathbf{V} : \delta\mathbf{u}^h(\mathbf{x}) = \sum_{J=1}^{M} \delta u_J \, \mathbf{N}_J(\mathbf{x}), \; \delta u_J \in \mathbb{R} \right\}. \end{aligned} \tag{3.55}$$

The increments, derivatives and derivatives of increments of the functions in the function space $\mathbf{W}^h$ are given as

$$\Delta\mathbf{W}^h = \left\{ \Delta\mathbf{u}^h \in \mathbf{W} : \Delta\mathbf{u}^h(\mathbf{x}) = \sum_{I=1}^{M} \Delta u_I \, \mathbf{N}_I(\mathbf{x}), \; \Delta u_I \in \mathbb{R} \right\}, \tag{3.56}$$

$$\nabla\mathbf{W}^h = \left\{ \nabla\mathbf{u}^h \in \mathbf{W} : \nabla\mathbf{u}^h(\mathbf{x}) = \sum_{I=1}^{M} u_I \, \nabla\mathbf{N}_I(\mathbf{x}), \; u_I \in \mathbb{R} \right\}, \tag{3.57}$$

$$\nabla\Delta\mathbf{W}^h = \left\{ \nabla\Delta\mathbf{u}^h \in \mathbf{W} : \nabla\Delta\mathbf{u}^h(\mathbf{x}) = \sum_{I=1}^{M} \Delta u_I \, \nabla\mathbf{N}_I(\mathbf{x}), \; \Delta u_I \in \mathbb{R} \right\}. \tag{3.58}$$

Inserting the descritized approximations $\Delta\mathbf{u} \approx \Delta\mathbf{u}^h$ and $\delta\mathbf{u} \approx \delta\mathbf{u}^h$ in Equation (3.51), we have

$$\begin{aligned} &\int_{\mathcal{B}_0} \left\{ \sum_{I=1}^{M} \Delta u_I \nabla_0 \mathbf{N}_I^T(\mathbf{x}) \cdot \mathbf{S}(\overline{\boldsymbol{\varphi}}) \cdot \sum_{J=1}^{N} \delta u_J \nabla_0 \mathbf{N}_J(\mathbf{x}) + \sum_{I=1}^{M} \sum_{J=1}^{N} \delta\mathbf{E}(\overline{\boldsymbol{\varphi}}) \cdot \left[\mathfrak{C}(\overline{\boldsymbol{\varphi}}) : \Delta\mathbf{E}(\overline{\boldsymbol{\varphi}}) \right]_{IJ} \right\} \mathrm{d}V \\ &= -\int_{\mathcal{B}_0} \sum_{I=1}^{M} \mathbf{S}(\overline{\boldsymbol{\varphi}}) \cdot \delta\mathbf{E}(\overline{\boldsymbol{\varphi}}) \, \mathrm{d}V + \int_{\partial\mathcal{B}_{0,t}} \sum_{I=1}^{M} \delta u_I \left[\mathbf{t}^p \cdot \mathbf{N}_I(\mathbf{x}) \right] \mathrm{d}A \quad \forall \delta\mathbf{u}^h \in \mathbf{V}^h. \end{aligned} \tag{3.59}$$

Applying the Gauss quadrature rule for numerical integration, the final cellwise FE discretized form is given as

$$\sum_{q}\sum_{I,J}\left\{\left(\nabla_0 \mathbf{N}_I^T(q)\cdot\nabla_0\mathbf{N}_J(q)\cdot\mathbf{S}(\overline{\boldsymbol{\varphi}})\right)\Delta u_I\delta u_J J w(q)+\left(\delta\mathbf{E}(\overline{\boldsymbol{\varphi}})\cdot\left[\mathfrak{C}(\overline{\boldsymbol{\varphi}}):\Delta\mathbf{E}(\overline{\boldsymbol{\varphi}})\right]_{IJ}\right)Jw(q)\right\}$$
$$=-\sum_{q}\sum_{I}\left(\mathbf{S}(\overline{\boldsymbol{\varphi}})\cdot\delta\mathbf{E}(\overline{\boldsymbol{\varphi}})\right)J\ w(q)+\sum_{q}\sum_{I}\mathbf{t}^p\cdot\mathbf{N}_I(q)J\ w(q), \tag{3.60}$$

where q are the quadrature points and $w(q)$ their corresponding weights.

3.7 Implementation details

3.7.1 Newton's method for non-linear problems

The discretization of the quasi-static finite strain elasticity problem leads to a non-linear system of algebraic equations. A direct solution of such a non-linear equation is in general not possible and hence iterative solution procedures are considered. One such iterative solution procedure is the Newton's method, also known as the Newton-Raphson method.

Newton's method uses first and second derivatives of the objective function, here the total potential energy function Π. The general idea of this method is: Given an initial guess (close to the minimizer of the objective function), we construct a quadratic approximation to the objective function that matches the first and second derivative values at this point. We then minimize the approximate (quadratic) function instead of the original objective function. We use the minimizer of the approximate function as the starting point in the next iteration step and repeat the procedure iteratively [25].

We will consider here the load controlled Newton-Raphson scheme for this discussion. The term *load control* means that the applied external loads are prescribed and increased in a stepwise manner. For each of these load steps, the unknown displacements are then computed by the non-linear solver. The Newton-Raphson scheme relies on a Taylor series expansion of the non-linear equation $\mathbf{R}(\mathbf{u}) = \mathbf{0}$ at a known state, i.e. at the last known equilibrium state. The Taylor series expansion with linearisation as given in Equation (3.50) can be written as

$$\mathbf{K}_i\cdot d\mathbf{u}+\mathbf{R}(\mathbf{u}_i)=\mathbf{0}, \tag{3.61}$$

for the iteration i. The unknown increment in the solution $\Delta\mathbf{u}$ is the difference in the unknown solution at the current state $\mathbf{u}_{i+1}$ and solution at the known state $\mathbf{u}_i$. This is obtained by the solution of the resulting discretized linear system of equations by direct or iterative solution methods. The updated solution is then derived as

$$\mathbf{u}_{i+1}=\mathbf{u}_i+\Delta\mathbf{u}. \tag{3.62}$$

With the updated solution, the residuum $\mathbf{R}$ is computed again and the procedure is repeated until the norm of the residuum is under a specified numerical tolerance. The algorithm for Newton-Raphson method is presented in Algorithm 3.1.

The rate of convergence of the Newton-Raphson method is given by the inequality $\|\mathbf{u}_{i+1} - \mathbf{u}\| \leq C\|\mathbf{u}_i - \mathbf{u}\|^2$ [17], where $\mathbf{u}$ is the actual solution of $\mathbf{R}(\mathbf{u}) = \mathbf{0}$ and C is a positive constant. The quadratic convergence of this scheme is only valid near the solution point. An advantage of this property is a converged solution is obtained within a few iterations. As a disadvantage, as one can observe in the algorithmic steps in Algorithm 3.1, one needs to assemble the tangent matrix $\mathbf{K}$ and solve the linear system of equations at each iteration step. This can be time consuming and also computationally expensive for a system with large number of unknowns.

Algorithm 3.1: NEWTON-RAPHSON METHOD

Given : Number of load steps n, numerical tolerance value *tol* and maximum Newton-Raphson iterations i_{max}

Return: Equilibrium solution for the total applied load

foreach *Load step* n **do**

- Prescribe the external load for current load step n;
- Compute the residuum $\mathbf{R}(\mathbf{u})^1_{n+1}$;

foreach *Newton-Raphson iteration* $i < i_{max}$ **do**

while $\|\mathbf{R}(\mathbf{u}^{i+1}_{n+1})\| > tol$ **do**

- Impose boundary conditions corresponding to the NR iteration i;
- Assemble the tangent matrix $\mathbf{K}^i_{n+1}$;
- Solve the linear system: $\mathbf{K}^i_{n+1} \cdot \Delta\mathbf{u} = -\mathbf{R}(\mathbf{u}^i_{n+1})$;
- Update solution $\mathbf{u}_{i+1} = \mathbf{u}_i + \Delta\mathbf{u}$;
- Update quadrature point data: $\mathbf{F}$ and corresponding stress, strain measures;
- Compute residuum $\mathbf{R}(\mathbf{u}^{i+1}_{n+1})$;

if $\|\mathbf{R}(\mathbf{u}^{i+1}_{n+1})\| \leq tol$ **then**

Break and move to next load step;

if $i \geq i_{max}$ **then**

No convergence! Break and throw error message;

3.7.2 Transformations needed for axisymmetric problem

The three-dimensional problem can be reduced to a two-dimensional problem if the loading, geometry and material behaviour do not change with a third coordinate. Such a class of problems is called *axisymmetric* where the analysis domain is a three-dimensional body of revolution defined in cylindrical coordinates (r, z, θ) but the deformations are two-dimensional functions of r, z only [27]. The body is three-dimensional but defined by a surface of revolution such that the properties and boundaries are independent of θ coordinate. For the chosen cylindrical coordinate system in the reference configuration

$$\mathbf{X} = \begin{bmatrix} R \\ \Theta \\ Z \end{bmatrix}, \tag{3.63}$$

the displacement field for the (torsionless) axisymmetric problem may be taken as

$$\mathbf{u} = \begin{bmatrix} u_R \\ u_Z \end{bmatrix}. \tag{3.64}$$

The rules for coordinate transformation between Cartesian and Cylindrical coordinate system are

$$\begin{aligned} X = R\cos\Theta,\ Y = R\sin\Theta,\ Z = Z, \\ \mathrm{d}X = \mathrm{d}R,\ \mathrm{d}Y = R\ \mathrm{d}\Theta,\ \mathrm{d}Z = \mathrm{d}Z, \\ \text{with } R = \sqrt{X^2 + Y^2} \text{ and } \tan\Theta = \frac{Y}{X}. \end{aligned} \tag{3.65}$$

The 3D volume integral is then transformed for an axisymmetric formulation as

$$\begin{aligned} \int_{\mathcal{B}_0} \mathrm{d}V = \int_X \int_Y \int_Z \mathrm{d}Z\ \mathrm{d}Y\ \mathrm{d}X = \int_R \int_\Theta \int_Z \mathrm{d}Z\ R\mathrm{d}\Theta\ \mathrm{d}R, \\ \text{with } \int_\Theta \mathrm{d}\Theta = 2\pi \text{ (independent of } \Theta \text{ coordinate)}, \\ \int_{\mathcal{B}_0} \mathrm{d}V = \int_R \int_Z 2\pi\ R\ \mathrm{d}R\ \mathrm{d}Z. \end{aligned} \tag{3.66}$$

For the (torsionless) axisymmetric problem with the given displacement field as in Equation (3.64), the required deformation gradient (a 2^{nd} order tensor) is given as [27]

$$\mathbf{F} = \begin{bmatrix} r_{,R} & r_{,Z} & 0 \\ z_{,R} & z_{,Z} & 0 \\ 0 & 0 & r/R \end{bmatrix} = \begin{bmatrix} (1+u_{r,R}) & u_{r,Z} & 0 \\ u_{z,R} & (1+u_{z,Z}) & 0 \\ 0 & 0 & (1+u_r/R) \end{bmatrix}. \tag{3.67}$$

This results in a 2^{nd} order $[(dim+1)\times(dim+1)]$ tensor $\mathbf{F}$ in a $dim=2$ axisymmetric problem. Further, the derived quantities using the deformation gradient $\mathbf{F}$ such as second Piola-Kirchhoff stress $\mathbf{S}$ and Green-Lagrange strain $\mathbf{E}$ are also 3×3 tensors whereas the fourth order material elasticity tensor $\mathfrak{C}$ is a $3\times3\times3\times3$ tensor in a 2.5D axisymmetric problem.

3.7.3 Data structures employed

3.7.3.1 Constitutive material model (CMM)

As described in depth in Section 3.3, we consider the entire continuum body to be composed of a compressible hyperelastic material. The corresponding Neo-Hookean strain energy density function were stated in Equation (3.16) for a purely non-linear compressible hyperelastic material. We implement this material model using a data structure which is stored at each local quadrature point of the cell/element. Within each object of this data structure we store the current state characterized by the values of solution fields and use these current state values to compute the kinematic, kinetic quantities and the resulting stresses at the given load/time step.

The quantities stored within an object of this material model data structure are as given in Table 3.1. This data structure is provided with two functionalities: to update the material quantities such as the Jacobian J using the deformation dependent data such as deformation gradient $\mathbf{F}$, and to compute the values of the different quantities such as the second Piola-Kirchhoff stress $\mathbf{S}$ and the fourth order material elasticity tensor $\mathfrak{C}$ at the current load/time step. This data structure also has a consistency check for a positive value of the bulk modulus κ and positive Jacobian (to avoid material self-penetration) for each deformation state of the body.

Quantity	Symbol	SI Unit
Shear modulus	μ	Pa
Bulk modulus	κ	Pa
Poisson's ratio	ν	-
Lamé 1st parameter	λ	Pa
Jacobian	J	-

Table 3.1: Material parameters and quantities stored at each local quadrature point

3.7.3.2 Local quadrature point history data (LQPH)

A data structure to store data items at each local quadrature point was used and adapted to our needs from [23]. This data structure stores a pointer (in our case a std::shared_ptr) to the CMM object at each quadrature point. It also stores the material quantities evaluated at the quadrature point such as the deformation gradient $\mathbf{F}$,

the second Piola-Kirchhoff stress and the fourth order material elasticity tensor $\mathfrak{C}$. This data structure is provided with two functionalities: first, to initialize each cell of q number of quadrature points with q copies of this object and set-up the CMM object data at each of these q points with user input material quantities such as shear modulus μ and Poisson's ratio ν. Secondly, update the CMM object using the computed kinematic quantity such as $\mathbf{F}$ from the current solution state. The LQPH data structure also provides "getter" functions to access the current values of quantities such as $\mathbf{F}, \mathbf{S}$ and $\mathfrak{C}$ that can be directly accessed, for e.g., during the assembly of the system matrix and R.H.S. vector.

Using a generic data structure implementation one can have different material models with individual material property values for μ and ν in different regions of the simulation domain. For example, in our modelling case for the quasi-static compressible finite strain elasticity problem, we model the torus-shaped magneto-elastic membrane along with the surrounding free space (through which the magnetic field permeates). Both, the free space and membrane, are considered to be composed of an elastic material. In this scenario one can employ separate material models for the free space and the magneto-elastic membrane and also use comparative values for the material parameters μ and ν (e.g. use low stiffness parameter to idealize the free space as a very complaint elastic solid).

3.7.3.3 Load step

Within the scope of finite strain elasticity, in order to capture the non-linear material behaviour undergoing finite deformations for large loads using a non-linear solver such as Newton Raphson method, it is necessary to apply the total load in small increments considering the quadratic convergence of the Newton Raphson method when near the solution point. Thus, one needs to control the applied load in each load step and such a method is called a load controlled Newton Raphson method. Here, we consider a uniformly increasing load in each load step with a constant load step size. User input parameters taken are the total load $\mathbf{F}_{ext}$ to be applied at the end of the load cycle and the load step size $\Delta\mathbf{F}_{ext}$ that is applied in each of these load steps.

The data structure implemented for the load stepping stores the current load step number, current load value, final/total load to be applied $\mathbf{F}_{ext}$ and the increment of the load $\Delta\mathbf{F}_{ext}$ in each load cycle. Use of this data structure can be observed in Algorithm 3.1 at the first algorithmic loop. Once the Newton Raphson solver has converged (arrived at the equilibrium state of the continuum body) for the applied load increment, the load step data structure increments the current load step number and the current applied load.

3.8 Test models and results

3.8.1 Unit testing with CTest

For consistency checks and reproducibility of the results of the different implementation steps, various unit tests were set up. A **unit test** is a software testing method to test an individual module (in object-oriented programming, a function or a class) to determine whether it is fail-proof and thus fit to use. Unit tests are short code fragments written by a software developer to test the individual blocks of the software and benchmark the functioning of the unit block during a software development cycle. The primary goal of unit testing is to find problems in the early stage of the development cycle. This is performed by isolating individual parts of the program and show that these individual parts function correctly and continue to function properly through the software development cycle. We employ one such testing tool, CTest, that is distributed as a part of CMake build process application.

3.8.2 Mechanical problem test models

Tests with different geometries and loading and boundary conditions were set up to verify the correctness and fail-proof behaviour of the different individual functions implemented. We also set up a test to check the quality of the solution for the finite element used on a simple geometry consisting of few elements for which the exact solution is known and can be manually reproduced. Such a test in the numerical approximation technique such as the finite element method is known as **patch test for finite elements.** The employed finite elements pass the patch test if the finite element solution is the same as or relatively close (under a given tolerance) to the exact known solution. Further tests were set up to check the implementation of the non-linear solution method and the ability of the solver to capture the instability behaviour of the structure for given loads. All of the mentioned tests were performed on some mechanical **axisymmetric** problems. The results are for the total Lagrangian formulation with the loads applied on the undeformed/reference domain.

3.8.2.1 Patch test

We consider an axisymmetric geometry with unit cube cross section which is discretized into nine elements, cf. Figure 3.1a. To check for the discretization error in the numerical solution using a selected finite element, we also have a distorted grid with the grid points in the interior of mesh distorted in a random way, cf. Figure 3.1b. The hyperelastic Neo-Hookean material model as given in Equation (3.16) was considered for the patch material. The material parameters chosen for this test were $\mu = 3e^{-2}$ Pa and $\nu = 0.4$. The considered boundary conditions are: homogeneous Dirichlet boundary condition on the boundary along the axis of symmetry (boundary id $= 0$) and inhomogeneous Dirichlet

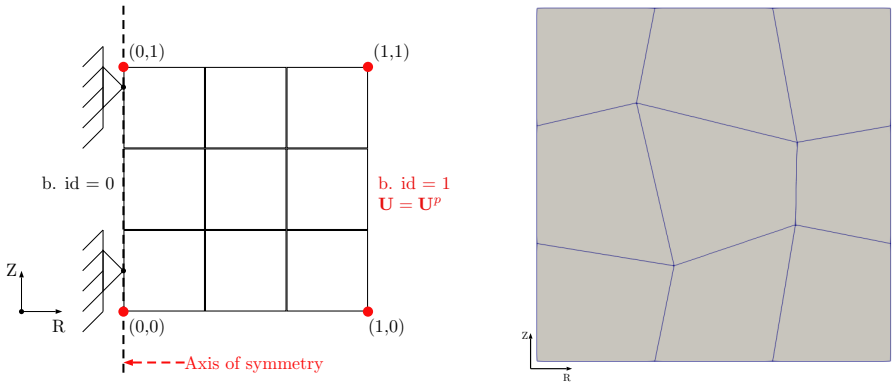

(a) Uniform grid (b) Distorted grid

Figure 3.1: Patch test unit cube geometry

boundary condition (tensile load) on boundary id = 1. The prescribed displacement of 0.1m was applied in a uniformly increasing step of 0.025m. Lagrange finite elements with bi-linear and bi-quadratic shape functions were employed for this patch test. One h-adaptive mesh refinement cycle was performed to compare the quality of solution between the coarse mesh and once h-adaptively refined mesh for the distorted grid geometry.

Comparing the results for the final deformed states for the distorted mesh in Figure 3.2 and the uniform grid patch in Figure 3.3, we can confirm that the employed bi-linear (vector-valued) shape functions ($Q_1 \times Q_1$) for the displacement field lead to qualitatively similar results (under given tolerance) as the ones for the bi-quadratic shape functions ($Q_2 \times Q_2$). In the regions with high solution gradient (here the cells near the boundary with boundary id = 0), an increase in the number of degrees of freedom due to h-adaptive mesh refinement would lead to a higher accuracy solution. Thus, the deformed states after one refinement cycle for the distorted grid are different compared to the uniform grid results. But the nature of the displacement field is similar irrespective of the employed bi-linear or bi-quadratic shape functions.

3.8.2.2 Traction boundary condition test

A unit test to check the traction boundary condition implementation was set up with an axisymmetric beam geometry problem. The considered beam is of length 2 m and height 1 m. The beam is discretized into 8 elements along the length and 4 elements along the height, thus giving a total of 32 elements in the coarse mesh. The hyperelastic Neo-Hookean material model as given in Equation (3.16) was considered for the beam material. The chosen material parameters for this test were $\mu = 3e^{-2}$ Pa and $\nu = 0.4$. The considered boundary conditions are: homogeneous Dirichlet boundary condition on the boundary along the axis of symmetry with boundary id = 0 and a uniformly

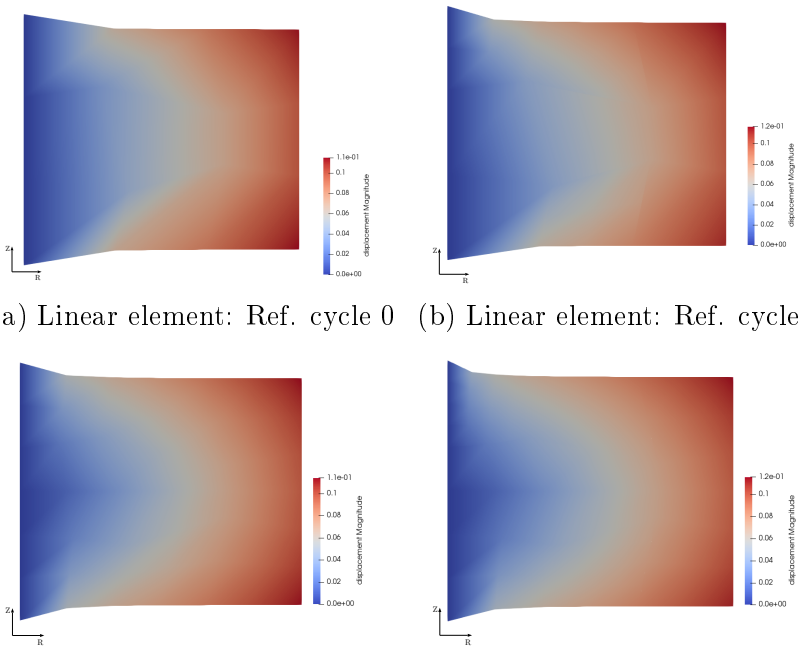

(a) Linear element: Ref. cycle 0 (b) Linear element: Ref. cycle 1

(c) Quadratic element: Ref. cycle 0 (d) Quadratic element: Ref. cycle 1

Figure 3.2: Distorted grid displacement at total load

distributed traction load (-Z) on the right half of the top boundary of the beam with boundary id = 6, cf. Figure 3.4. The considered traction load has a magnitude of $1e^{-3}\frac{\mathrm{N}}{\mathrm{m}}$ distributed uniformly over a length of 1 m. Employing uniformly increasing load stepping, this traction load was applied in four load steps.

In the following, the algorithmic scheme for h-adaptive mesh refinement is highlighted. Due to a high solution gradient in the elements near the axis of symmetry (b.id = 0) in the coarse grid, cf Figure 3.5a, the resulting error in solution is high in these elements. To reduce the error in the solution we need to make the mesh fine where the local (H^2) norm of the solution is large. We compute a local indicator of error η_K for every cell K employing a standard error estimator such as the "**Kelly error estimator**" from the literature [5] which constitutes to an "**a-posteriori**" error estimate. The local Kelly error indicator η_K for each cell is given as

$$\eta_K := h_K^{\frac{1}{2}} \left(\int_{\partial K} |[\![\nabla \mathbf{u_h}]\!]|^2 \right)^{\frac{1}{2}}, \tag{3.68}$$

where h_k is taken to be the greatest length of the diagonals of the cell K, $\nabla \mathbf{u_h}$ is the gradient of the computed FE solution and $[\![\nabla \mathbf{u_h}]\!]$ denotes the jump in the gradient which is an indicator of the second derivative of the solution field.

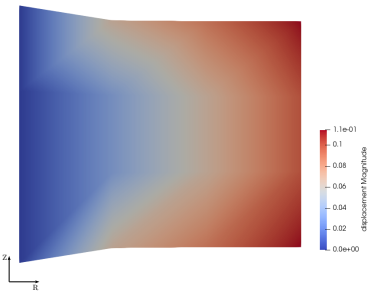

(a) Linear element: Ref. cycle 0

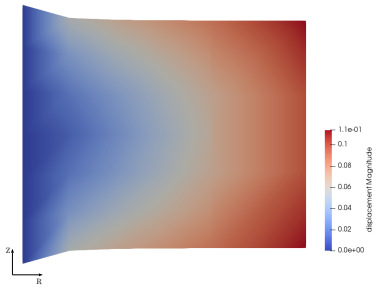

(b) Linear element: Ref. cycle 1

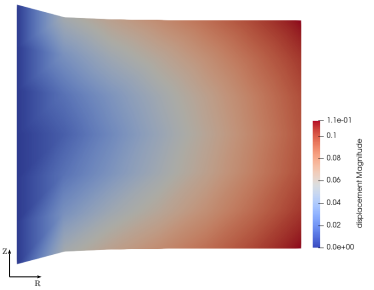

(c) Quadratic element: Ref. cycle 0

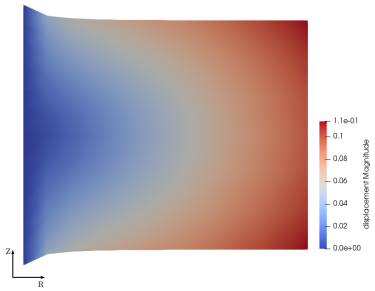

(d) Quadratic element: Ref. cycle 1

Figure 3.3: Uniform grid displacement at total load

Algorithm 3.2 highlights the procedure one carries out to perform h-adaptive mesh refinement. We employ the **SOLVE-ESTIMATE-MARK-REFINE** cycle for adaptive refinement. In the solve phase we assemble the linear system of equations and solve it on the coarse/current mesh. By use of heuristically derived error estimator such as the Kelly error estimator, we estimate the error on each cell of the mesh. In the mark phase, following some chosen strategy we mark the cells with largest error for refinement and coarsening. In the last phase, we refine and coarsen the marked cells and continue this iterative procedure for a user selected number of refinement cycles. More details of the refinement procedure with the mathematical foundations for the error estimator and the different marking strategies one can employ can be found in [40, Chapter 4].

The final deformed state for individual refinement cycles are as observed in Figure 3.5a and Figure 3.5b. As expected, upon mesh refinement we observe the solution field is more accurate and has reduced jump in the gradient of the solution field in the (refined) cells near the axis of symmetry. This test proves the effectiveness of an adaptively refined mesh in computing the solution more accurately and motivates the need of such adaptivity in the region of interest for a complex geometry and multi-physics problem discussed in the further section.

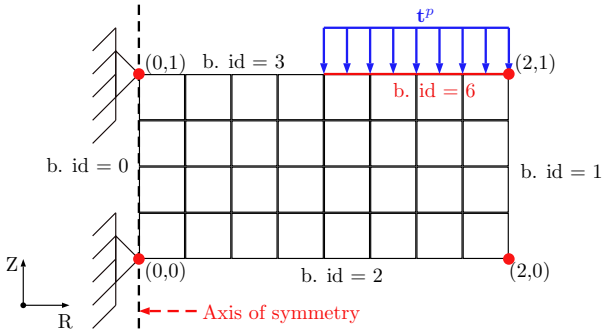

Figure 3.4: Beam problem with traction load

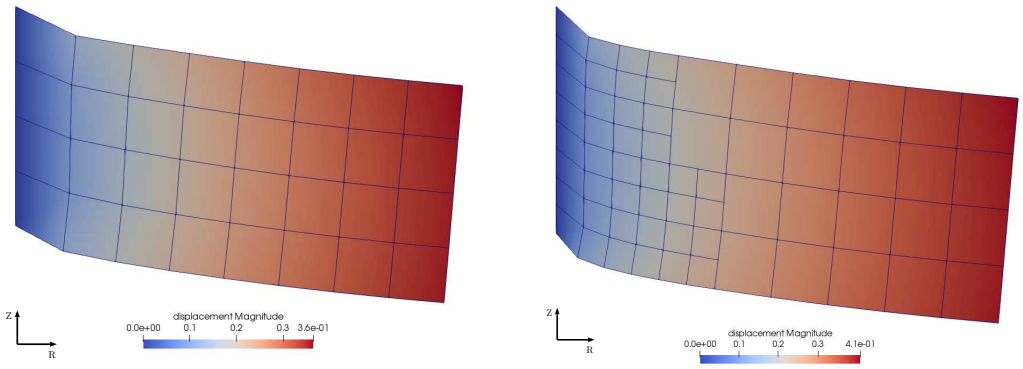

(a) Ref. cycle 0 (b) Ref. cycle 1

Figure 3.5: Beam displacement

Algorithm 3.2: H-ADAPTIVE MESH REFINEMENT CYCLE

1. Start with the coarse mesh
2. Solve on this mesh
3. Compute error indicator η_K for every cell based on the numerical solution
4. Mark a fraction of the cells with largest error
5. Refine the marked cells to get the new mesh
6. Start over at 2

3.8.2.3 Test for instability behaviour

Mechanical instability is an important phenomenon in determining the limit loads a structure can handle before becoming unstable. A stable design of the structure exists

when the deformations increase as the applied load increases; an unstable design occurs when the deformations increase as the load decreases due to loss of stiffness. The study of such finite elastic deformations of structures helps in understanding the limit loads and prevent sudden buckling/snap-through failures of the structure for applied loads. Referring to Figure 3.6 commonly known as the load-deflection plot of the equilibrium path, elastic limit point is the critical point after which the structure/material begins to deform largely even for slightly increasing loads. For a load past the critical limit point (1), the structure undergoes a non-linear buckling which includes a post-buckling instability region. The "snap-through" occurs in the non-linear instability region and the equilibrium path goes from one stable point (1) to another stable point (2). The non-linear behaviour places the next stable point (2) at the same critical limit load as point (1), but this new load limit at point (2) now corresponds to a new structural shape [19]. The slope of the equilibrium path during the snap-through eventually becomes zero. The slope of this curve is also known as "tangent stiffness". From a mathematical point of view the determination of instability points is related to the investigation of tangent stiffness with respect to singularities. At the bifurcation point a secondary equilibrium path branches off the primary equilibrium path. Bifurcation point is the limit point at which the structure immediately becomes unstable and buckles. The structure is unable to support any further loads.

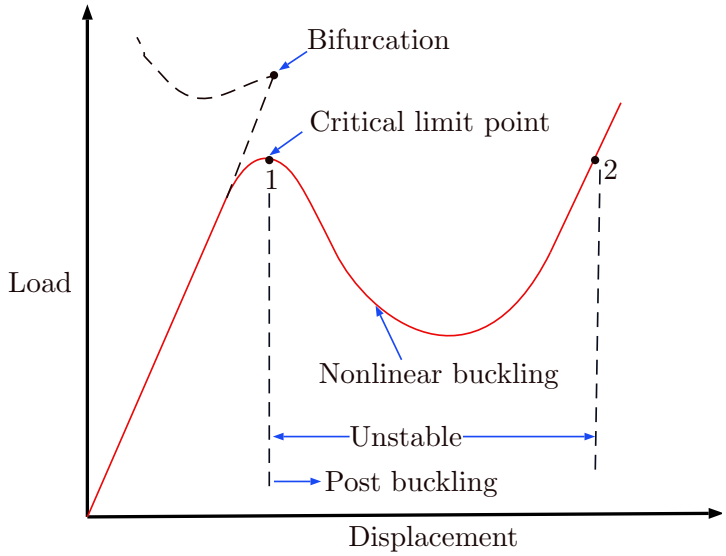

Figure 3.6: Equilibrium paths for non-linear buckling

For the stability analysis two test models were implemented as seen in Figure 3.7a and Figure 3.8. The first mechanical test model was inspired by a commonly occurring tin mint box with round top, Figure 3.7b, that snaps through to open the box. The cap of this box undergoes a sudden large deformation for an applied point load at the middle point of the round cap. This instability mode is a desired deformation to open the box.

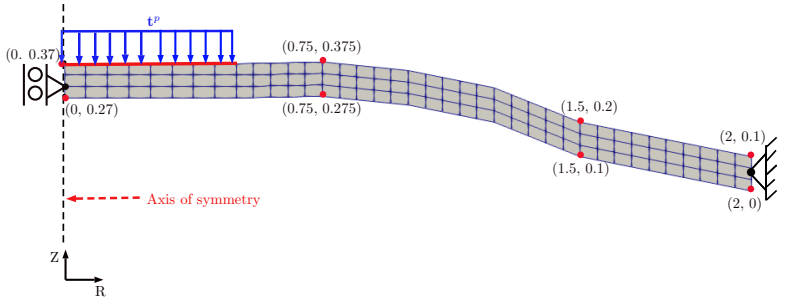

(a) Hooped beam test model

(b) Mint box that exhibits snap through behaviour

Figure 3.7: Mechanical instability test model 1

On application of equal loads on the opposite ends of the cap, the cap snaps back to the original shape/form to close the box. To simulate such a sudden snap through behaviour using robust non-linear solvers we developed the axisymmetric hooped beam test model as illustrated in Figure 3.7a. The out-of-plane displacement of the beam end is fixed by considering pin support (homogeneous Dirichlet boundary condition) and the edge lying on the axis of symmetry has a "sliding" constraint ($u_x = 0, u_y \neq 0$) that preserves the symmetry about the axis of the problem. A uniformly distributed traction load $\mathbf{t}^p = 1.5e^{-4}\ \frac{\mathrm{N}}{\mathrm{m}}$ acts on the top surface of beam as shown in the model. The hyperelastic Neo-Hookean material model as stated in Equation (3.16) was considered for the hooped beam with material parameters $\mu = 3e^{-2}$ Pa and $\nu = 0.4$.

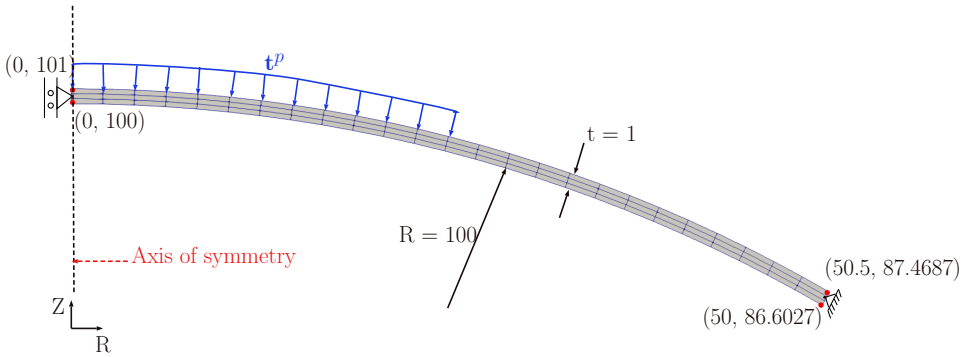

Figure 3.8: Crisfield beam test model

The second test model to perform stability analysis of structures is the Crisfield beam, cf. Figure 3.8, which is used as a standard benchmark test model to study instability modes [see 17, page 170] and [19]. The considered beam has an inner radius of 100 m and

outer radius of 101 m and the included angle of 30°. For this test model, same boundary conditions were considered as used for the hooped beam test model. A uniformly distributed traction load $\mathbf{t}^p = 2e^{-4}\ \frac{\mathrm{N}}{\mathrm{m}}$ was applied as illustrated in the representative figure. Same material parameter values were considered as employed in the hooped beam model.

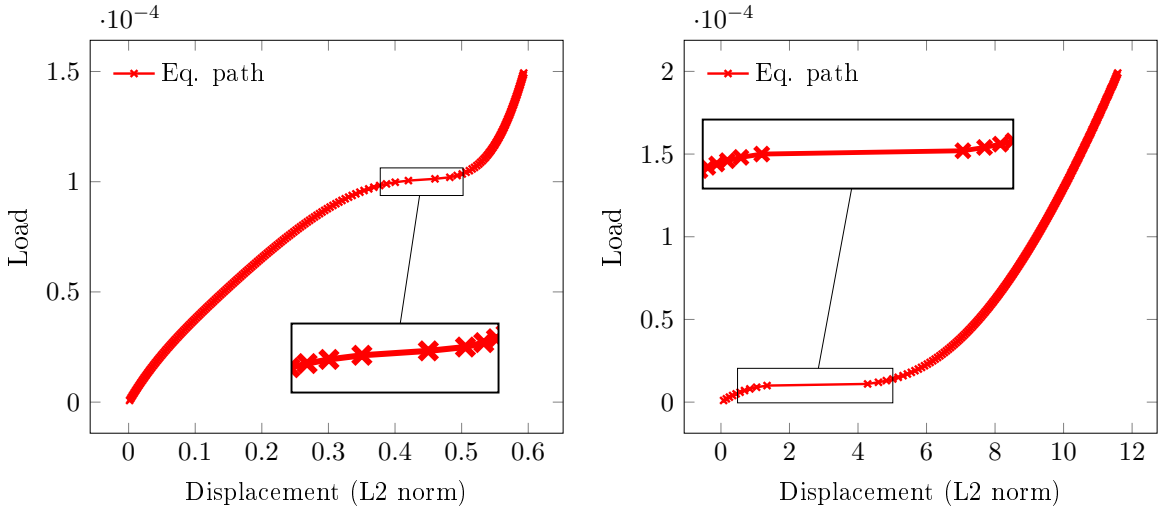

(a) Hooped beam test

(b) Crisfield beam test

Figure 3.9: Equilibrium paths for test models

The results using the Newton-Raphson solution method for the solution of the non-linear test models are presented in Figure 3.11. The resulting load-displacement plots, also known as the equilibrium path, for the point $(0, 0.27)$ in the hooped beam test and the point $(0, 100)$ in the crisfield beam test are depicted in Figure 3.9 (lower edge points on the boundary along the axis of symmetry). For the hooped beam test, as observed in Figure 3.9a, in the early stages of loading, for each load increment of size $7.5e^{-7}$ N there is a proportional increase in the resulting displacement. We observe a linear relation between the load and displacement in this stage which one can identify as the initial linear response of a hyperelastic material. After a certain load limit is reached, we observe for a small load increment a resulting large displacement identified by the jumps in the cross marked points in the zoomed view in Figure 3.9a. This is also clearly observable in the results of Figure 3.11a. Between the load step number 134 and 135 corresponding to the zoomed region of interest, the structure undergoes a sudden large deformation for a small increment in the applied load. A similar result is also observed for the crisfield beam test in the early stages of loading cycle. The large jump in the displacement from $\approx$ 1.3 m to $\approx$ 4.3 m for a small increment of load of size $1e^{-6}$ N in Figure 3.9b indicates that the structure has undergone unstable deformation. This significantly large displacement is clearly illustrated in Figure 3.11b between the load step 10 and 11. This work softening of the structure is due to the reduced material

stiffness after reaching a certain limit load point that leads to material instability and buckling.

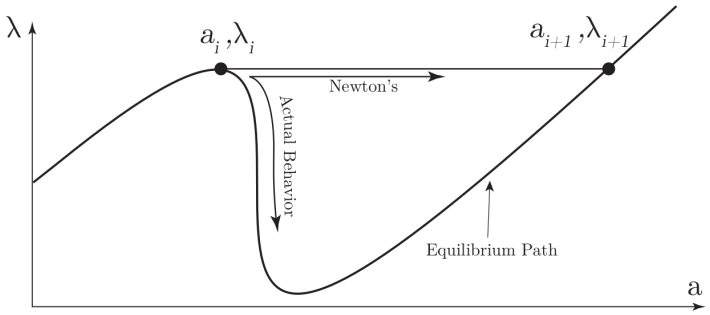

Figure 3.10: Failure of Newton's method to accurately capture the solution after a limit point is reached [33]

As observed in both the Figures 3.9a and 3.9b in the region of interest near the limit point, the tangent to the equilibrium path, also known as the tangent stiffness, approaches to zero. As already pointed out in the literature [3], [4] and [33], a major drawback of the employed Newton's method is the failure of the method to accurately follow the equilibrium path once the tangent stiffness reaches zero. This happens due to the formulation of Newton's method, and in particular that it restricts the load parameter to change monotonically in every increment [33]. This problem is better visualized in Figure 3.10. The jump from one stable point to another without following the actual unstable buckling path is clearly identified in the result for the crisfield beam equilibrium path in Figure 3.9b. Thus, the failure of the Newton method after the limit point was verified by our tests and it should be noted that the method was not able to capture the material instability resulting in incorrect deformations after the limit point. Employing a robust non-linear path-following solution method from the literature [4] (such as the Arc-Length method) can be seen as the logical extension to study the instability behaviour of such structures.

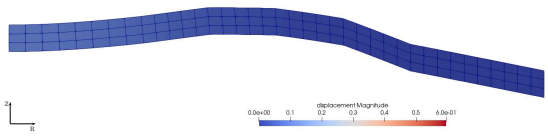

Load step 50

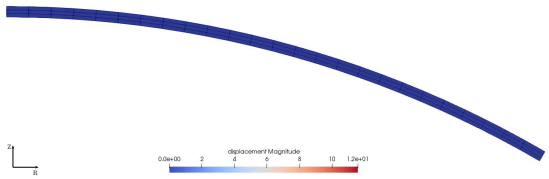

Load step 0

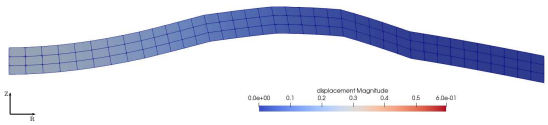

Load step 100

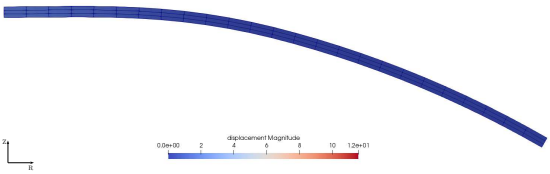

Load step 10

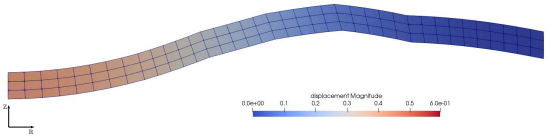

Load step 134

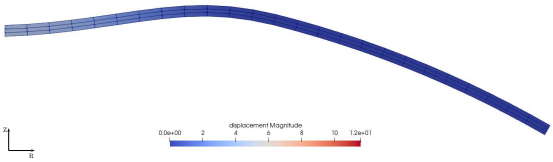

Load step 11

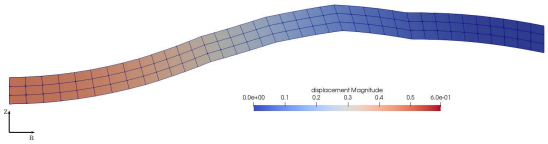

Load step 135

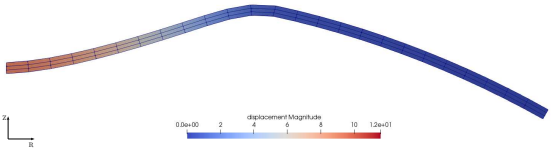

Load step 99

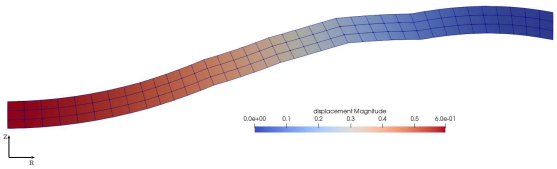

Load step 199

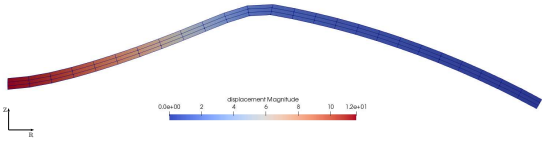

Load step 199

(a) Hooped beam deformations

(b) Crisfield beam deformations

Figure 3.11: Instability test results

3.9 Numerical results for the finite deformations of torus membrane with free space

For the geometry of our interest as observed in Figure 3.12a, we now study the elastic finite deformations of the torus magneto-elastic membrane with initial circular cross-section under a quasi-static inflating pressure load. The membrane is modelled as a non-linear elastic material employing the hyperelastic Neo-Hookean material model, cf. Equation (3.16). The material parameter values for the magneto-elastic membrane were taken as $\mu = 3e^4$ Pa, $\nu = 0.4$. The surrounding free space (vacuum) through which the magnetic field $\mathbb{H}$ permeates is also modelled as a relatively less stiff elastic material, employing the same Neo-Hookean material model but with different material parameter values of $\mu = 3e^{-2}$ Pa and $\nu = 0.3$. Employing the total Lagrangian formulation, the inflating pressure load was applied on the undeformed/reference domain in uniformly increasing load steps as

$$\mathbf{t}^p = \mathbf{P}\mathbf{N} = [p_0\mathbf{I}]\,\mathbf{N} = p_0\mathbf{N}, \tag{3.69}$$

where $\mathbf{P}$ is the 1^{st} Piola-Kirchhoff stress, p_0 is the inflating pressure load (scalar) and $\mathbf{N}$ is the referential unit inward pointing normal vector for any point on the inner interface of the torus membrane. The inflating pressure load was taken as $p_0 = 1e^3 \frac{\mathrm{N}}{\mathrm{m}^2}$. Homogeneous Dirichlet boundary condition was considered for the boundary of the free space domain.

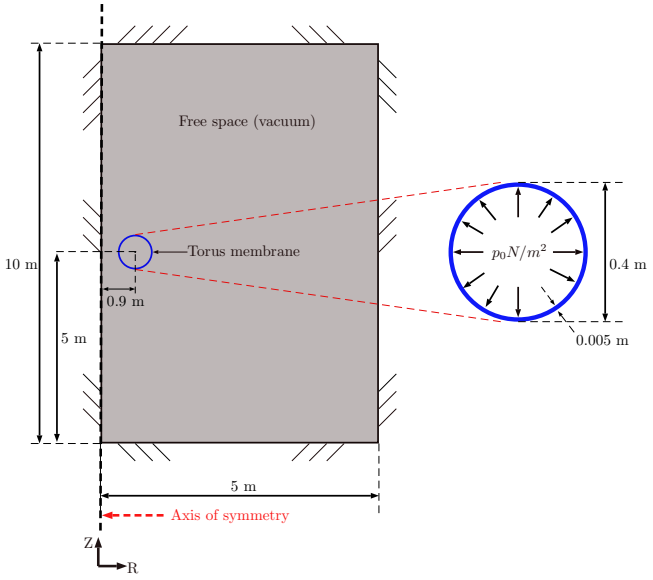

(a) Problem description

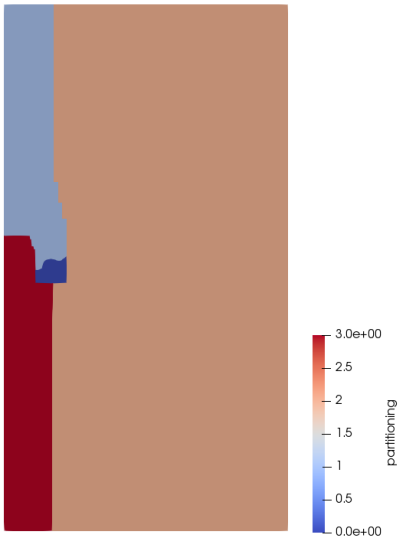

(b) Domain decomposition for 4 MPI processes

Figure 3.12: Magneto-elastic membrane under uniform inflating pressure load

The result of the above described uniformly inflating membrane problem is as observed in the Figure 3.13. Due to the applied mechanical load, here quasi-static uniform inflat-

ing pressure load on inner interface of the membrane, large deformations are observed in the membrane and the surrounding elements of the free space. The deformations in the free space region far away from the torus membrane are small/negligible compared to the deformations in the elements belonging to the torus membrane. As observed in the displacement field of the deformed membrane (lower right image in Figure 3.13), the deformations in the membrane are relatively large on the right half of the circular cross section when compared to the left half. This is due to the dependence of the deformation gradient $\mathbf{F}$ (component F_{33}) on the radial distance of the respective point on the membrane from the axis of symmetry, cf. Equation (3.67). Thus, for any point on the torus membrane, with increasing radial distance the resulting displacements increase.

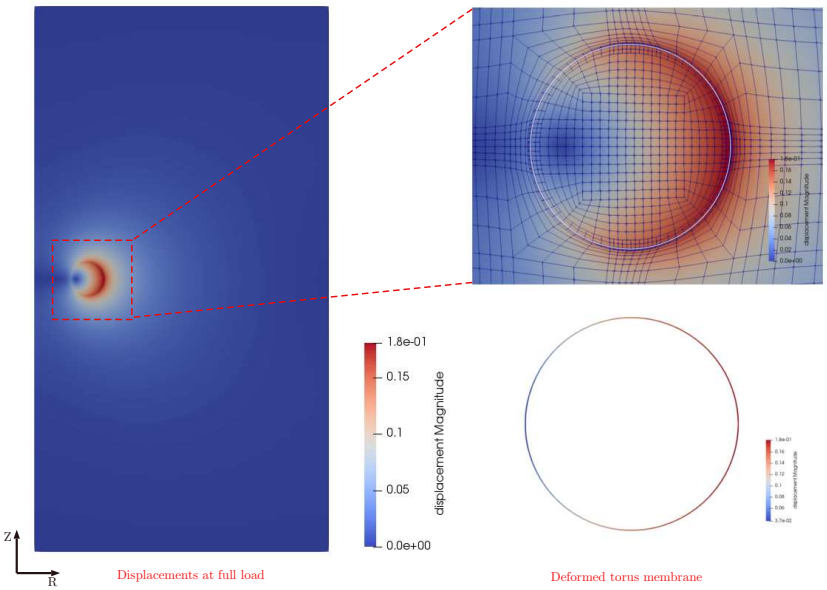

Figure 3.13: Deformations at full load

For the considered free space parameters of $\mu = 3e^{-2}$ Pa and $\nu = 0.3$, one can observe that the free space material modelled with relatively less stiffness acts as a very complaint elastic material. This complaint elastic free space material allows for a free inflation of the membrane without any considerable reactive force/pressure load exerted by the free space material on the inflating membrane. The degree of deformations of the free space elements for increasing pressure load can be observed in Figure 3.14. The torus membrane elements are ignored from the visualization and thus we observe a white circular section in the presented results.

Element-wise volume averaged Cauchy stress $\boldsymbol{\sigma}$ components (radial component σ_{rr} and theta component $\sigma_{\theta\theta}$) were also computed to have an understanding of the resulting engineering stress in the torus membrane. The element-wise volume averaged stress was

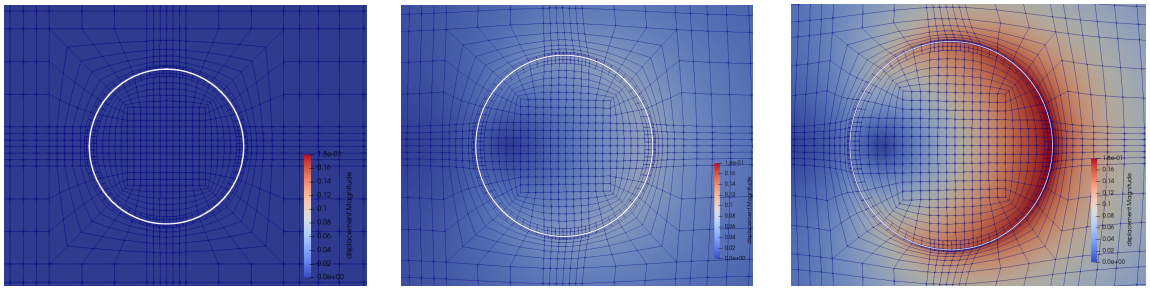

(a) Load step 0 (no load) (b) Load step 9 (Half load) (c) Load step 19 (Full load)

Figure 3.14: Free space (vacuum) deformations

computed as

$$\langle \boldsymbol{\sigma} \rangle_e := \frac{\int\limits_{\Omega_e} \boldsymbol{\sigma} \mathrm{d}V_e}{\int\limits_{\Omega_e} \mathrm{d}V_e} = \frac{\sum\limits_q \boldsymbol{\sigma}(q) * J(q) * w(q)}{\sum\limits_q J(q) * w(q)}. \tag{3.70}$$

The resulting element averaged Cauchy stress components can be observed in Figure 3.15. The dependence of the stress component $\sigma_{\theta\theta}$ on the radial distance of the point on the membrane from the axis of symmetry is clearly observed in Figure 3.15b. Thus, we observe a symmetry in the stress component field $\sigma_{\theta\theta}$ about the centre line cutting the membrane horizontally. Whereas a symmetry in the stress component field σ_{rr} about the centre line cutting the membrane vertically can be observed in Figure 3.15a.

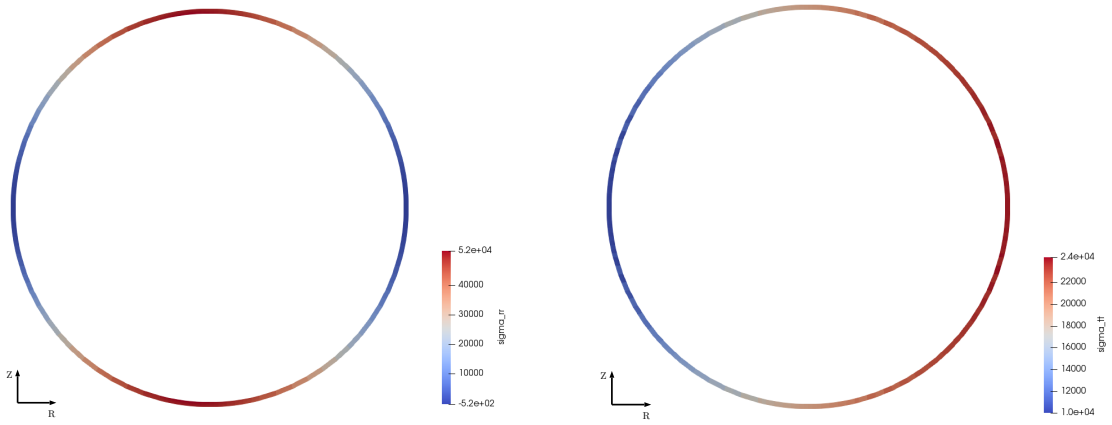

(a) σ_{rr} (b) $\sigma_{\theta\theta}$

Figure 3.15: Element averaged Cauchy stress components for torus membrane

3.9.1 Parametric study of free space parameter μ

To model the free space material surrounding the torus membrane as a very compliant elastic we needed to select the elastic stiffness of the free space material such that there would be no reactive force by the free space material on the inflating torus membrane. For a selected less stiffer free space material one could then assume the torus membrane to inflate freely, adhering to the reality of the physics. Thus, a parametric study of the free space shear modulus μ was carried out for the finite strain axisymmetric torus elasticity problem. For the given inflating pressure load of $p_0 = 1e^3 \frac{\mathrm{N}}{\mathrm{m}^2}$, torus membrane parameters $\mu = 3e^4$ Pa and $\nu = 0.4$, along with fixed value for the Poisson's ratio of the free space material as $\nu = 0.3$, the free space shear modulus μ was varied between $\mu_1 = 3e1$ Pa and $\mu_2 = 3e^{-2}$ Pa.

As expected and observed in Figure 3.16, with higher value of the free space shear modulus $\mu = 3e^1$ Pa the free space material acts more stiff and we observe the effect of this increased stiffness on the deformation of the torus membrane for the same applied pressure load. The resultant deformed state of the torus membrane in Figure 3.16b for the value of μ_1, the stiffer free space material obstructs the free inflation of the membrane. Thus, we have relatively less deformed membrane when compared to the deformed state for μ_2.

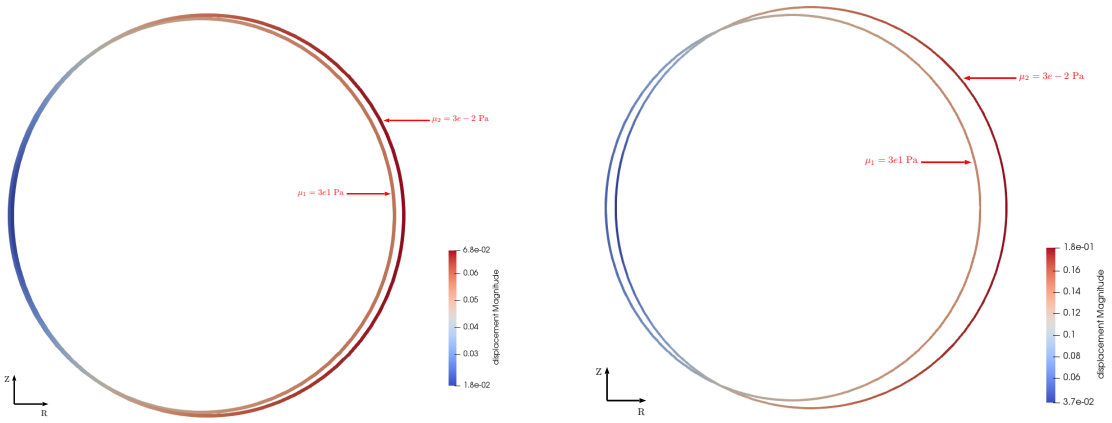

(a) Load step 9 (Half load)

(b) Load step 19 (Full load)

Figure 3.16: Deformations of torus membrane for different free space material parameter value μ

The resulting element averaged Cauchy stress components can be observed in Figure 3.17. The developed stress due to larger deformations of the membrane for less stiffer (μ_2) free space material is higher than the resulting stress for the more stiffer (μ_1) free space material.

For appropriate modelling of the membrane and free space with considered assumptions, it is necessary that we choose the material values for the free space such that we

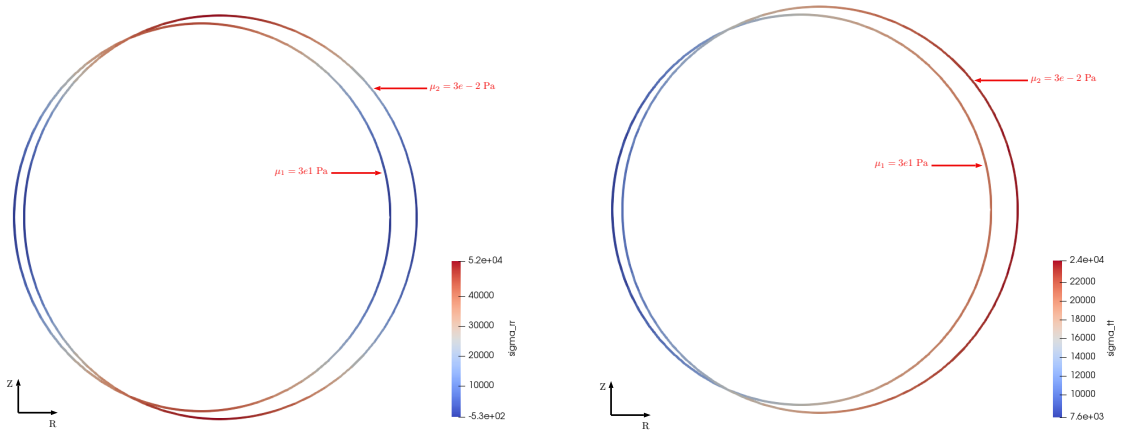

(a) σ_{rr} (b) $\sigma_{\theta\theta}$

Figure 3.17: Element averaged Cauchy stress components of torus membrane for different free space material parameter value μ

can closely approximate our free space material as being a compliant solid with negligible stiffness and thus exerting negligible loads on the inflating elastic torus membrane geometry of our interest. For values of $\mu < 3e^{-2}$ Pa, we observed negligible differences in the resulting deformed states and stress when compared to the results for the value of $\mu = 3e^{-2}$ Pa. Thus, a chosen value of $\mu \approx 3e^{-2}$ Pa can be considered as appropriate to model the free space.

3.10 Extensions planned for coupled problem

The planned extensions for the next chapter are introducing the coupled problem and multi-physics employing a material model for the magneto-elastic material of our interest. The to be considered Neo-Hookean material model for the magneto-elastic material is given as

$$\Psi \equiv \frac{\mu}{2}[\mathbf{C} : \mathbf{I} - \mathbf{I} : \mathbf{I} - 2\ln J] + \frac{\lambda}{2}(\ln J)^2 - \frac{\mu_0 \mu_r}{2}\left[J\ \mathbf{C}^{-1} : \mathbb{H} \otimes \mathbb{H}\right]. \tag{3.71}$$

The additional highlighted term takes into account the energy stored in the body due to applied external magnetic load $\mathbb{H}$ and the response of the coupled interaction between the displacement field and the magnetic field. The loads to be applied would be the uniformly distributed inflating pressure load on the inner interface of the torus membrane and the static magnetic field as mentioned in the results of previous Chapter 2. Furthermore, we would then consider the solution field to be comprised of two blocks, the scalar magnetic potential ϕ and the vector-valued displacement field $\mathbf{u}$. The corresponding linear algebra concepts for such a multi-physics problem are mentioned in further sections.

Vector-valued problem

The solution in the elasticity problem discussed here is not just a single scalar function but has displacements $\mathbf{u} := \{u_x, u_y, u_z\}^T$ in each euclidean direction, thus we have a vector system which is a set of scalar functions and thus is also addressed as *vector-valued solution*. When considering the coupled magneto-elastic problem, the resulting vector-valued solution has elements $\{\phi, u_x, u_y, u_z\}^T$. These elements of the vector-valued solution can be grouped into *blocks*, where for the coupled magneto-elastic problem we have two blocks at each global degree of freedom in the finite element mesh, one block for the magnetic scalar potential function ϕ and the second block for the vector displacement function $\mathbf{u}$ with three individual components u_x, u_y, u_z in 3D. This way one is able to access all the components/elements of the vector field such as displacement together without splitting them into their individual components.

Block linear algebra

Use of the block structure also proves advantageous in terms of linear algebra and solution methods. One can think of the global linear system of equation $\mathbf{Ax} = \mathbf{b}$ as

$$\begin{bmatrix} \mathbf{A}_{\phi\phi} & \mathbf{A}_{\phi\mathbf{u}} \\ \mathbf{A}_{\mathbf{u}\phi} & \mathbf{A}_{\mathbf{uu}} \end{bmatrix} \begin{bmatrix} \phi \\ \mathbf{u} \end{bmatrix} = \begin{bmatrix} \mathbf{F}_{\text{Œ}} \\ \mathbf{F}_{\mathbf{u}} \end{bmatrix},$$

where ϕ and $\mathbf{u}$ are the values of the scalar magnetic potential field and the displacement field. $\mathbf{A}_{\phi\phi}$ denotes the matrix contributions arising from the linearisation of the magnetic problem and $\mathbf{A}_{\mathbf{uu}}$ describes the tangent matrix contribution from the elasticity problem. $\mathbf{A}_{\phi\mathbf{u}}$ and $\mathbf{A}_{\mathbf{u}\phi}$ are the coupled interaction contributions. One can solve the complete system considering as a single unit which can be convenient for the assembly of the matrix and right-hand-side vector for some class of problems. When employing the Gauss elimination rather than solving the problem monolithically, depending upon the properties of the (block) matrices for individual problem, one can then define individual preconditioners that best suite the operators present in the system of equations rather than defining a single preconditioner for the global matrix $\mathbf{A}$.

Vector-valued finite elements

We shall consider here in all the discussions only *primitive finite elements*. A finite element is said to be primitive if there is a unique relation from the shape function number to the vector component of the vector-valued element. This means for a primitive element we have exactly one non-zero component for each shape function of the vector-valued element. The Lagrangian elements that we shall employ are primitive elements. For the considered vector-valued coupled magneto-elastic problem we build the vector-valued finite element from simpler base elements using tensor product of the base elements. We take multiple simple elements (eg. scalar linear Lagrange elements Q_1)

and connect them to have an element with more than one block. For the vector-valued displacement field in 2D, we can construct a vector-valued finite element using two Q_1 elements (each constituting to a single component u_x and u_y) to form using a tensor product $Q_1 \times Q_1$ element with two components. This will form a single block in our coupled problem where the second block for the scalar magnetic potential will have only a single component such as a quadratic element Q_2. Thus, the vector-valued element we shall employ, for e.g., can be represented in block form as $(Q_1 \times Q_1, Q_2)$ which will have in total $\dim + 1$ individual components in 2D as $[u_x, u_y, \phi]$.

4 Coupled magneto-elasticity

4.1 Kinematics

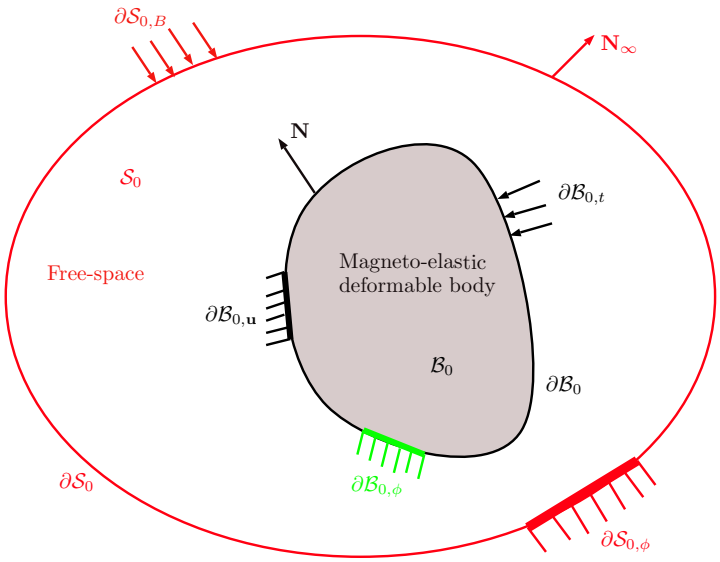

Figure 4.1: Domain definition: Deformable magneto-elastic solid $\mathcal{B}_0$ immersed in an electromagnetically permeable free space ($\mathcal{S}_0$).

We consider a compressible magneto-elastic deformable solid $\mathcal{B}_0$ with a boundary $\partial\mathcal{B}_0$ in a reference state of no stress and no deformation. In this state, the free space surrounding the deformable solid is denoted as $\mathcal{S}_0$ with the topologically constant/fixed boundary $\partial\mathcal{S}_0$. We denote the entire domain containing the magneto-elastic and the surrounding free space domain as $\mathcal{D}_0 := \mathcal{B}_0 \cup \mathcal{S}_0$. On application of a combined static mechanical and magnetic load, the body deforms and occupies the current state $\mathcal{B}_t$ with boundary $\partial\mathcal{B}_t$. In the current configuration the free space is denoted as $\mathcal{S}_t$, the free space boundary due to fixed constraints stays constant with $\partial\mathcal{S}_0 = \partial\mathcal{S}_t$ and the entire domain is denoted as $\mathcal{D}_t := \mathcal{B}_t \cup \mathcal{S}_t$. Any point in the deformed/current configuration $\mathbf{x} \in \mathcal{D}_t$ is identified by a one-to-one non-linear deformation map $\boldsymbol{\varphi}$ to $\mathbf{X} \in \mathcal{D}_0$ as $\mathbf{x} := \boldsymbol{\varphi}(\mathbf{X})$. We define the associated deformation gradient relative to reference configuration $\mathcal{D}_0$ as $\mathbf{F} := \nabla_0 \boldsymbol{\varphi}$ and its determinant $J := \det\mathbf{F} > 0$ to ensure that $\boldsymbol{\varphi}$ remains invertible and it also avoid the material self-penetration. Here, the gradient w.r.t. $\mathcal{D}_0$ is denoted as ∇_0 and that w.r.t. $\mathcal{D}_t$ is denoted as ∇. $\mathbf{N}$ describes the unit outward normal to

$\partial\mathcal{B}_0$ and $\mathbf{N}_\infty$ describes the unit outward normal to the boundary $\partial\mathcal{S}_0$. We denote the portion of boundary $\partial\mathcal{B}_{0,\mathbf{u}}$ as the boundary with prescribed deformations and $\partial\mathcal{B}_{0,t}$ as the boundary with prescribed mechanical traction load. The portion $\partial\mathcal{B}_{0,\phi}$ denotes the boundary with prescribed magnetic scalar-valued potential. We assume the boundary $\partial\mathcal{S}_{0,\mathbf{u}} = \partial\mathcal{S}_0$ to be prescribed with homogeneous Dirichlet boundary condition for the deformations (fixing the free space boundary topology). We apply a prescribed magnetic scalar-valued potential $\overline{\phi}$ on the portion $\partial\mathcal{S}_{0,\phi}$ to generate a magnetic vector field $\mathbb{H}$ in $\mathcal{D}_0$. Let the associated referential magnetic induction vector be $\mathbb{B}$ and the magnetization vector be $\mathbb{M}$.

We proceed with the assumption that there exists no free electric currents and thus, no electric fields in the complete computational domain. As already explained in detail in Chapter 2, due to the magnetic vector fields such as $\mathbb{H}$ which is discontinuous over boundaries and material interfaces, for the purpose of finite element modelling we proceed with a magnetic scalar potential formulation. We assume a fictitious quantity ϕ and define the curl-free magnetic field $\mathbb{H}$ as [21, 28]

$$\mathbb{H} := -\nabla_0\phi \text{ in } \mathcal{D}_0. \tag{4.1}$$

The continuity condition associated with potential ϕ is

$$[\![\phi]\!] = 0 \text{ on } \partial\mathcal{B}_0, \tag{4.2}$$

and the Dirichlet and Neumann boundary conditions are

$$\phi = \overline{\phi} \text{ on } \partial\mathcal{S}_{0,\phi}, \quad \mathbb{B}_\infty \cdot \mathbf{N}_\infty = \overline{b} \text{ on } \partial\mathcal{S}_{0,B}, \tag{4.3}$$

where $\overline{b}$ is the prescribed magnetic flux on the far-field boundary.

4.2 Constitutive material model for coupled problem

The material response is characterised by a Helmholtz free energy density function. For the considered magneto-elastic material, in addition to the dependence on the deformation gradient $\mathbf{F}$ and the Jacobian J (as already seen in quasi-static finite strain compressible elasticity, Chapter 3), the free energy density function now also depends on the referential magnetic vector field. The strain energy function (S.E.F.) is given as

$$\Psi = \widetilde{\Psi}(J, \mathbf{F}, \mathbb{H}) = \Psi(J, \mathbf{C}, \mathbb{H}). \tag{4.4}$$

Using the symmetry argument from the definition of the right Cauchy-Green deformation tensor $\mathbf{C} := \mathbf{F}^T \cdot \mathbf{F}$, the dependence of $\mathbf{F}$ is simplified to a dependence on $\mathbf{C}$. The isotropic hyperelastic material response when $\mathbf{C}$ is used to describe the S.E.F. is given by the constitutive relation as

$$\mathbf{S} = 2\frac{\partial\Psi(J, \mathbf{C}, \mathbb{H})}{\partial\mathbf{C}}. \tag{4.5}$$

The referential magnetic induction vector field $\mathbb{B}$ is modelled in terms of the referential magnetic vector field $\mathbb{H}$, taking $\mathbb{H}$ as the independent field

$$\mathbb{B} = \mathbb{B}(\mathbb{H}), \tag{4.6}$$

which is termed as the alternative formulation in [8]. With $\mathbb{H}$ chosen as the independent field, its components can be chosen to satisfy the vector equation $\mathrm{Curl}\mathbb{H} = \mathbf{0}$ and then the resulting $\mathbb{B}$ has to satisfy the scalar equation $\mathrm{Div}\mathbb{B} = 0$. This alternative formulation does not put restrictions on the admissible class of constitutive laws (which arise if one were to proceed with $\mathbb{B}$ as the independent field) and also avoids the complexities of a vector-valued magnetic field from the finite element modelling aspects. The fundamental constitutive equation that relates the magnetic quantities $\mathbb{B}, \mathbb{H}$ and the magnetization vector $\mathbb{M}$ is given as [8, 11]

$$J^{-1}\mathbf{C} \cdot \mathbb{B} = \mu_0 \left[\mathbb{H} + \mathbb{M}\right]. \tag{4.7}$$

The magnetization vector field exists only in the solid magneto-elastic material and vanishes in the free space. $\mathbb{B}$ is given by another constitutive relation as [8]

$$\mathbb{B} = -\frac{\partial \Psi(J, \mathbf{C}, \mathbb{H})}{\partial \mathbb{H}}. \tag{4.8}$$

The S.E.F corresponding to a compressible coupled magneto-elastic Neo-Hookean material is given as

$$\Psi(J, \mathbf{C}, \mathbb{H}) = \frac{\mu}{2}\left[\mathbf{C} : \mathbf{I} - \mathbf{I} : \mathbf{I} - 2\ln J\right] + \frac{\lambda}{2}(\ln J)^2 - \frac{\mu_0 \mu_r}{2}[J\mathbf{C}^{-1} : \mathbb{H} \otimes \mathbb{H}], \tag{4.9}$$

$$= \Psi^{\mathrm{elas}}(\mathbf{C}) + \mu_r M_0(J, \mathbf{C}, \mathbb{H}), \tag{4.10}$$

$$\text{with } M_0(J, \mathbf{C}, \mathbb{H}) := -\frac{\mu_0}{2}[J\mathbf{C}^{-1} : \mathbb{H} \otimes \mathbb{H}], \tag{4.11}$$

where μ and ν are the Lamé parameters, $\mu_0 = 4\pi \times 10^{-7}\ \mathrm{Hm}^{-1}$ is the free space (vacuum) magnetic permeability and μ_r is the relative magnetic permeability of the magneto-elastic material ($\mu_r = 1$ characterises the free space material). The term highlighted in red takes into account the energy stored in the body due to applied external magnetic load $\mathbb{H}$ and the response of the coupled interaction between the displacement field and the magnetic field. The term $\Psi^{\mathrm{elas}}(\mathbf{C})$ describes the purely elastic response of the material and the term $M_0(J, \mathbf{C}, \mathbb{H})$ describes the total energy per unit volume stored in the magnetic fields in the free space [8]. The constant $\mu_r > 1$ characterises a magnetisable material such as the membrane.

The second Piola-Kirchhoff stress $\mathbf{S}$ for the considered S.E.F. as stated in Equation (4.11) is derived below.

$$\begin{aligned}\mathbf{S} &= 2\frac{\partial \Psi(J, \mathbf{C}, \mathbb{H})}{\partial \mathbf{C}} \\ &= 2\left[\frac{\mu}{2}\left\{\frac{\partial[\mathbf{C} : \mathbf{I}]}{\partial \mathbf{C}} - 2\frac{\partial \ln J}{\partial \mathbf{C}}\right\} + \frac{\lambda}{2}\frac{\partial(\ln J)^2}{\partial \mathbf{C}} - \frac{\mu_0 \mu_r}{2}\frac{\partial[J\mathbf{C}^{-1} : \mathbb{H} \otimes \mathbb{H}]}{\partial \mathbf{C}}\right]\end{aligned}$$

Side calculation 1:

$$\begin{aligned}
\frac{\partial[\mathbf{C}:\mathbf{I}]}{\partial\mathbf{C}} &= \mathbf{I},\\
\frac{\partial \ln J}{\partial\mathbf{C}} &= \frac{1}{J}\frac{\partial J}{\partial\mathbf{C}},\\
\frac{\partial(\ln J)^2}{\partial\mathbf{C}} &= 2\ \ln J\ \frac{\partial \ln J}{\partial\mathbf{C}},\\
\frac{\partial J}{\partial\mathbf{C}} &= \frac{1}{2}J\mathbf{C}^{-1}\quad \text{c.f. [see 17, page 46 Equation (3.124)].}
\end{aligned}$$

$$\mathbf{S} = \mu\mathbf{I} - \mu\mathbf{C}^{-1} + \lambda \ln J\mathbf{C}^{-1} - \mu_0\mu_r\frac{\partial[J\mathbf{C}^{-1}:\mathbb{H}\otimes\mathbb{H}]}{\partial\mathbf{C}}$$

Side calculation 2: Note $\mathbf{C} := \mathbf{F}^T\cdot\mathbf{F}$ is symmetric $\implies$ $\mathbf{C}^{-1}$ is also symmetric

$$\begin{aligned}
\frac{\partial[J\mathbf{C}^{-1}:\mathbb{H}\otimes\mathbb{H}]}{\partial\mathbf{C}} &= \frac{\partial[JC^{-1}_{IJ}H_IH_J]}{\partial C_{KL}}\ \mathbf{E}_K\otimes\mathbf{E}_L\\
&= C^{-1}_{IJ}\ H_I\ H_J\ \frac{\partial J}{\partial C_{KL}}\ \mathbf{E}_K\otimes\mathbf{E}_L + J\ H_I\ H_J\ \frac{\partial C^{-1}_{IJ}}{\partial C_{KL}}\ \mathbf{E}_K\otimes\mathbf{E}_L\\
&= C^{-1}_{IJ}\ H_I\ H_J\ \frac{J}{2}\ C^{-1}_{KL}\ \mathbf{E}_K\otimes\mathbf{E}_L + J\ H_I\ H_J\ \frac{\partial C^{-1}_{IJ}}{\partial C_{KL}}\ \mathbf{E}_K\otimes\mathbf{E}_L
\end{aligned}$$

c.f. [see 17, page 519]:

$$\frac{\partial C^{-1}_{IJ}}{\partial C_{KL}} = -\frac{1}{2}[C^{-1}_{IK}\ C^{-1}_{LJ} + C^{-1}_{IL}\ C^{-1}_{KJ}]$$

$$\begin{aligned}
\frac{\partial[J\mathbf{C}^{-1}:\mathbb{H}\otimes\mathbb{H}]}{\partial\mathbf{C}} &= \frac{J}{2}C^{-1}_{IJ}H_IH_JC^{-1}_{KL}\mathbf{E}_K\otimes\mathbf{E}_L + \frac{-J}{2}\left[C^{-1}_{IK}C^{-1}_{LJ}H_IH_J + C^{-1}_{IL}C^{-1}_{KJ}H_IH_J\right]\mathbf{E}_K\otimes\mathbf{E}_L\\
&= \frac{J}{2}C^{-1}_{IJ}H_IH_JC^{-1}_{KL}\mathbf{E}_K\otimes\mathbf{E}_L - \frac{J}{2}\left[C^{-1}_{KI}H_IC^{-1}_{LJ}H_J + C^{-1}_{LI}H_IC^{-1}_{KJ}H_J\right]\mathbf{E}_K\otimes\mathbf{E}_L\\
&= \frac{J}{2}\ C^{-1}_{IJ}\ H_I\ H_J\ C^{-1}_{KL}\ \mathbf{E}_K\otimes\mathbf{E}_L - J[C^{-1}_{KI}\ H_I\ C^{-1}_{LJ}\ H_J]^{sym}\ \mathbf{E}_K\otimes\mathbf{E}_L\\
&= \frac{J}{2}[\mathbf{C}^{-1}:\mathbb{H}\otimes\mathbb{H}]\mathbf{C}^{-1} - J[(\mathbf{C}^{-1}\cdot\mathbb{H})\otimes(\mathbf{C}^{-1}\cdot\mathbb{H})]^{sym}
\end{aligned}$$

$$\begin{aligned}
\mathbf{S} = \mu\mathbf{I} &- [\mu - \lambda\ln J]\mathbf{C}^{-1} - \frac{\mu_0\mu_r}{2}\ J\ [\mathbf{C}^{-1}:\mathbb{H}\otimes\mathbb{H}]\mathbf{C}^{-1}\\
&+ \mu_0\mu_r\ J\ [(\mathbf{C}^{-1}\cdot\mathbb{H})\otimes(\mathbf{C}^{-1}\cdot\mathbb{H})]^{sym}
\end{aligned} \tag{4.12}$$

The referential magnetic induction vector field is given as

$$\begin{aligned}
\mathbb{B} &= -\frac{\partial \Psi(J,\mathbf{C},\mathbb{H})}{\partial \mathbb{H}} = -\frac{\partial M_0(J,\mathbf{C},\mathbb{H})}{\partial \mathbb{H}} \\
&= \frac{\mu_0\mu_r}{2}\frac{\partial [J\ \mathbf{C}^{-1} : \mathbb{H}\otimes\mathbb{H}]}{\partial \mathbb{H}} \\
&= \frac{\mu_0\mu_r}{2}\frac{\partial [J\ C^{-1}_{IJ}\ H_I\ H_J]}{\partial H_K}\mathbf{E}_K \\
&= \frac{\mu_0\mu_r}{2}\left[J\ C^{-1}_{IJ}\frac{\partial H_I}{\partial H_K}\ H_J + J\ C^{-1}_{IJ}\ H_I\frac{\partial H_J}{\partial H_K}\right]\mathbf{E}_K \\
&= \frac{\mu_0\mu_r}{2}\left[J\ C^{-1}_{IJ}\ \delta_{IK}\ H_J + J\ C^{-1}_{IJ}\ H_I\ \delta_{JK}\right]\mathbf{E}_K \\
&= \frac{\mu_0\mu_r}{2}J\left[\ C^{-1}_{JI}\ \delta_{IK}\ H_J + \ C^{-1}_{IJ}\ \delta_{JK}\ H_I\right]\mathbf{E}_K \\
&= \frac{\mu_0\mu_r}{2}J\left[\ C^{-1}_{JK}\ H_J + \ C^{-1}_{IK}\ H_I\right]\mathbf{E}_K \\
&= \frac{\mu_0\mu_r}{2}J\left[\ C^{-1}_{KJ}\ H_J + \ C^{-1}_{KI}\ H_I\right]\mathbf{E}_K
\end{aligned}$$

$$\boxed{\mathbb{B} = \mu_0\mu_r\ J\ [\mathbf{C}^{-1}\cdot\mathbb{H}].} \tag{4.13}$$

Now the different tangent tensors of the S.E.F. that are required in the linearisation process are described and derived below. The referential material elasticity tangent $\mathfrak{C}$ is defined as

$$\mathfrak{C} := 2\frac{\partial \mathbf{S}(J,\mathbf{C},\mathbb{H})}{\partial \mathbf{C}} = 4\frac{\partial^2 \Psi(J,\mathbf{C},\mathbb{H})}{\partial \mathbf{C}\otimes\partial \mathbf{C}}. \tag{4.14}$$

Using the result of Equation (4.12), $\mathfrak{C}$ is derived as follows.

$$
\begin{aligned}
\mathfrak{C} &= 2\frac{\partial \mathbf{S}}{\partial \mathbf{C}} \\
&= 2\frac{\partial S_{KL}}{\partial C_{MN}}\ \mathbf{E}_K \otimes \mathbf{E}_L \otimes \mathbf{E}_M \otimes \mathbf{E}_N \\
&= 2\left\{-\mathbf{C}^{-1} \otimes \frac{\partial[\mu - \lambda \ln J]}{\partial \mathbf{C}} - [\mu - \lambda \ln J]\frac{\partial \mathbf{C}^{-1}}{\partial \mathbf{C}} - \frac{\mu_0\mu_r}{2}[\mathbf{C}^{-1} : \mathbb{H} \otimes \mathbb{H}]\ \mathbf{C}^{-1} \otimes \frac{\partial J}{\partial \mathbf{C}}\right\} \\
&\quad + 2\left\{-\frac{\mu_0\mu_r}{2}\ J\ \mathbf{C}^{-1} \otimes \frac{\partial[\mathbf{C}^{-1} : \mathbb{H} \otimes \mathbb{H}]}{\partial \mathbf{C}} - \frac{\mu_0\mu_r}{2}\ J\ [\mathbf{C}^{-1} : \mathbb{H} \otimes \mathbb{H}]\frac{\partial \mathbf{C}^{-1}}{\partial \mathbf{C}}\right\} \\
&\quad + 2\left\{\mu_0\mu_r[(\mathbf{C}^{-1} \cdot \mathbb{H}) \otimes (\mathbf{C}^{-1} \cdot \mathbb{H})]^{sym} \otimes \frac{\partial J}{\partial \mathbf{C}} + \mu_0\mu_r\ J\ \frac{\partial[(\mathbf{C}^{-1} \cdot \mathbb{H}) \otimes (\mathbf{C}^{-1} \cdot \mathbb{H})]^{sym}}{\partial \mathbf{C}}\right\} \\
&= 2\left\{C^{-1}_{KL}\ \frac{\lambda}{J}\frac{\partial J}{\partial C_{MN}} - [\mu - \lambda \ln J]\left\{\frac{-1}{2}\left(C^{-1}_{KM}\ C^{-1}_{NL} + C^{-1}_{KN}\ C^{-1}_{ML}\right)\right\}\right\} \\
&\quad \mathbf{E}_K \otimes \mathbf{E}_L \otimes \mathbf{E}_M \otimes \mathbf{E}_N \\
&\quad + 2\left\{-\frac{\mu_0\mu_r}{2}\ [C^{-1}_{IJ}\ H_I\ H_J]C^{-1}_{KL}\frac{1}{2}\ J\ C^{-1}_{MN} - \frac{\mu_0\mu_r}{2}J\ C^{-1}_{KL}\frac{\partial[C^{-1}_{IJ}\ H_I\ H_J]}{\partial C_{MN}}\right\} \\
&\quad \mathbf{E}_K \otimes \mathbf{E}_L \otimes \mathbf{E}_M \otimes \mathbf{E}_N \\
&\quad + 2\left\{-\frac{\mu_0\mu_r}{2}\ J\ [C^{-1}_{IJ}\ H_I\ H_J]\left\{\frac{-1}{2}(C^{-1}_{KM}\ C^{-1}_{NL} + C^{-1}_{KN}\ C^{-1}_{ML})\right\}\right\}\mathbf{E}_K \otimes \mathbf{E}_L \otimes \mathbf{E}_M \otimes \mathbf{E}_N \\
&\quad + 2\left\{\mu_0\mu_r[C^{-1}_{KI}\ H_I\ C^{-1}_{LJ}\ H_J]^{sym}\ \frac{1}{2}J\ C^{-1}_{MN} + \mu_0\mu_r\ J\ \frac{\partial[C^{-1}_{KI}\ H_I\ C^{-1}_{LJ}\ H_J]^{sym}}{\partial C_{MN}}\right\} \\
&\quad \mathbf{E}_K \otimes \mathbf{E}_L \otimes \mathbf{E}_M \otimes \mathbf{E}_N \\
&= \lambda\ C^{-1}_{KL}\ C^{-1}_{MN} + [\mu - \lambda \ln J]\left(C^{-1}_{KM}\ C^{-1}_{NL} + C^{-1}_{KN}\ C^{-1}_{ML}\right) - \frac{\mu_0\mu_r}{2}\ J\ [C^{-1}_{IJ}\ H_I\ H_J]C^{-1}_{KL}\ C^{-1}_{MN} \\
&\quad - \mu_0\mu_r J\ C^{-1}_{KL}\ \frac{\partial[C^{-1}_{IJ}\ H_I\ H_J]}{\partial C_{MN}} + \frac{\mu_0\mu_r}{2}\ J\ [C^{-1}_{IJ}\ H_I\ H_J](C^{-1}_{KM}\ C^{-1}_{NL} + C^{-1}_{KN}\ C^{-1}_{ML}) \\
&\quad + \mu_0\mu_r\ J\ [C^{-1}_{KI}\ H_I\ C^{-1}_{LJ}\ H_J]^{sym}\ C^{-1}_{MN} + 2\mu_0\mu_r\ J\ \frac{\partial[C^{-1}_{KI}\ H_I\ C^{-1}_{LJ}\ H_J]^{sym}}{\partial C_{MN}} \\
&\quad \mathbf{E}_K \otimes \mathbf{E}_L \otimes \mathbf{E}_M \otimes \mathbf{E}_N
\end{aligned}
$$

Side calculation 1:

$$\begin{aligned}
\frac{\partial [C^{-1}_{IJ}\ H_I\ H_J]}{\partial C_{MN}} &= H_I\ H_J\ \frac{\partial C^{-1}_{IJ}}{\partial C_{MN}} \\
&= \frac{-1}{2}\ H_I\ H_J\ [C^{-1}_{IM}\ C^{-1}_{NJ} + C^{-1}_{IN}\ C^{-1}_{MJ}] \\
&= \frac{-1}{2}[C^{-1}_{MI}\ H_I\ C^{-1}_{NJ}\ H_J + C^{-1}_{NI}\ H_I\ C^{-1}_{MJ}\ H_J] \\
&= -[C^{-1}_{MI}\ H_I\ C^{-1}_{NJ}\ H_J]^{sym} \\
&= -[(\mathbf{C}^{-1}\cdot\mathbb{H})\otimes(\mathbf{C}^{-1}\cdot\mathbb{H})]^{sym}
\end{aligned}$$

Side calculation 2:

$$\begin{aligned}
\frac{\partial [C^{-1}_{KI}\ H_I\ C^{-1}_{LJ}\ H_J]^{sym}}{\partial C_{MN}} &= \frac{1}{2}\frac{\partial \left[C^{-1}_{KI}\ H_I\ C^{-1}_{LJ}\ H_J + C^{-1}_{LI}\ H_I\ C^{-1}_{KJ}\ H_J\right]}{\partial C_{MN}} \\
&= \frac{1}{2}\frac{\partial C^{-1}_{KI}}{\partial C_{MN}}\ H_I\ C^{-1}_{LJ}\ H_J + \frac{1}{2}C^{-1}_{KI}\ H_I\ \frac{\partial C^{-1}_{LJ}}{\partial C_{MN}}\ H_J \\
&\quad + \frac{1}{2}\frac{\partial C^{-1}_{LI}}{\partial C_{MN}}\ H_I\ C^{-1}_{KJ}\ H_J + \frac{1}{2}C^{-1}_{LI}\ H_I\ \frac{\partial C^{-1}_{KJ}}{\partial C_{MN}}\ H_J \\
&= \frac{1}{2}\frac{-1}{2}\left[C^{-1}_{KM}C^{-1}_{NI} + C^{-1}_{KN}C^{-1}_{MI}\right]\ H_I\ C^{-1}_{LJ}\ H_J \\
&\quad + \frac{1}{2}\frac{-1}{2}C^{-1}_{KI}\ H_I\left[C^{-1}_{LM}C^{-1}_{NJ} + C^{-1}_{LN}C^{-1}_{MJ}\right]\ H_J \\
&\quad + \frac{1}{2}\frac{-1}{2}\left[C^{-1}_{LM}C^{-1}_{NI} + C^{-1}_{LN}C^{-1}_{MI}\right]\ H_I\ C^{-1}_{KJ}\ H_J \\
&\quad + \frac{1}{2}\frac{-1}{2}C^{-1}_{LI}\ H_I\left[C^{-1}_{KM}C^{-1}_{NJ} + C^{-1}_{KN}C^{-1}_{MJ}\right]\ H_J \\
&= -\frac{1}{4}\left[C^{-1}_{KM}\ C^{-1}_{NI}\ H_I\ C^{-1}_{LJ}\ H_J + C^{-1}_{KN}\ C^{-1}_{MI}\ H_I\ C^{-1}_{LJ}\ H_J\right] \\
&\quad - \frac{1}{4}\left[C^{-1}_{KI}\ H_I\ C^{-1}_{LM}\ C^{-1}_{NJ}\ H_J + C^{-1}_{KI}\ H_I\ C^{-1}_{LN}\ C^{-1}_{MJ}\ H_J\right] \\
&\quad - \frac{1}{4}\left[C^{-1}_{LM}\ C^{-1}_{NI}\ H_I\ C^{-1}_{KJ}\ H_J + C^{-1}_{LN}\ C^{-1}_{MI}\ H_I\ C^{-1}_{KJ}\ H_J\right] \\
&\quad - \frac{1}{4}\left[C^{-1}_{LI}\ H_I\ C^{-1}_{KM}\ C^{-1}_{NJ}\ H_J + C^{-1}_{LI}\ H_I\ C^{-1}_{KN}\ C^{-1}_{MJ}\ H_J\right] \\
&= -\mathbb{X} - \mathbb{Y}
\end{aligned}$$

The tensors

$$\mathbb{X} := \frac{1}{4}\left[C^{-1}_{KI}H_IC^{-1}_{LM}C^{-1}_{NJ}H_J + C^{-1}_{KI}H_IC^{-1}_{LN}C^{-1}_{MJ}H_J + C^{-1}_{LI}H_IC^{-1}_{KM}C^{-1}_{NJ}H_J + C^{-1}_{LI}H_IC^{-1}_{KN}C^{-1}_{MJ}H_J\right]$$

$$\mathbb{Y} := \frac{1}{4}\left[C^{-1}_{KM}C^{-1}_{NI}H_IC^{-1}_{LJ}H_J + C^{-1}_{KN}C^{-1}_{MI}H_IC^{-1}_{LJ}H_J + C^{-1}_{LM}C^{-1}_{NI}H_IC^{-1}_{KJ}H_J + C^{-1}_{LN}C^{-1}_{MI}H_IC^{-1}_{KJ}H_J\right]$$

with basis matrix $\mathbf{E}_K \otimes \mathbf{E}_L \otimes \mathbf{E}_M \otimes \mathbf{E}_N$ are both symmetric rank-4 tensors such that for given symmetric rank-2 tensors $\mathbf{M}, \mathbf{N}, \mathbf{P}, \mathbf{Q}$, we have

$$\begin{aligned} \mathbf{N} &= \mathbb{X} : \mathbf{M}, \\ \mathbf{Q} &= \mathbb{Y} : \mathbf{P}. \end{aligned}$$

$$\begin{aligned} \mathfrak{C} = \lambda\ \mathbf{C}^{-1} \otimes \mathbf{C}^{-1} - 2[\mu - \lambda \ln J]\ \frac{\partial \mathbf{C}^{-1}}{\partial \mathbf{C}} \\ - \frac{\mu_0 \mu_r}{2}\ J\ [\mathbf{C}^{-1} : \mathbb{H} \otimes \mathbb{H}](\mathbf{C}^{-1} \otimes \mathbf{C}^{-1}) + \mu_0 \mu_r\ J\ (\mathbf{C}^{-1} \otimes [(\mathbf{C}^{-1} \cdot \mathbb{H}) \otimes (\mathbf{C}^{-1} \cdot \mathbb{H})]^{sym}) \\ - \mu_0 \mu_r\ J\ [\mathbf{C}^{-1} : \mathbb{H} \otimes \mathbb{H}]\ \frac{\partial \mathbf{C}^{-1}}{\partial \mathbf{C}} + \mu_0 \mu_r\ J\ ([(\mathbf{C}^{-1} \cdot \mathbb{H}) \otimes (\mathbf{C}^{-1} \cdot \mathbb{H})]^{sym} \otimes \mathbf{C}^{-1}) \\ - 2\mu_0 \mu_r\ J\ (\mathbb{X} + \mathbb{Y}) \end{aligned}$$

For given symmetric rank 2 tensors $\mathbf{A}$ and $\mathbf{B}$, we know: $\mathbf{A} \otimes \mathbf{B} = \mathbf{B} \otimes \mathbf{A}$.

$$\begin{aligned} \mathfrak{C} = \lambda\ \mathbf{C}^{-1} \otimes \mathbf{C}^{-1} - 2[\mu - \lambda \ln J]\ \frac{\partial \mathbf{C}^{-1}}{\partial \mathbf{C}} \\ - \frac{\mu_0 \mu_r}{2}\ J\ [\mathbf{C}^{-1} : \mathbb{H} \otimes \mathbb{H}](\mathbf{C}^{-1} \otimes \mathbf{C}^{-1}) - \mu_0 \mu_r\ J\ [\mathbf{C}^{-1} : \mathbb{H} \otimes \mathbb{H}]\ \frac{\partial \mathbf{C}^{-1}}{\partial \mathbf{C}} \\ + 2\mu_0 \mu_r\ J\ (\mathbf{C}^{-1} \cdot \mathbb{H}) \otimes (\mathbf{C}^{-1} \cdot \mathbb{H})]^{sym} \otimes \mathbf{C}^{-1}) - 2\mu_0 \mu_r\ J\ (\mathbb{X} + \mathbb{Y}) \end{aligned} \tag{4.15}$$

The fourth-order referential material elasticity tensor possess both major and minor symmetries, i.e. $\mathfrak{C} = C_{KLMN} = C_{MNKL} = C_{KLNM} = C_{LKMN}$.

The derivation for the magneto-static tangent $\mathbf{D} := \dfrac{\partial^2 \Psi(J, \mathbf{C}, \mathbb{H})}{\partial \mathbb{H} \otimes \partial \mathbb{H}}$ is as follows:

$$\begin{aligned} \mathbf{D} &= \frac{\partial \mathbb{B}}{\partial \mathbb{H}} \\ &= \frac{\partial [\mu_0 \mu_r\ J\ (\mathbf{C}^{-1} \cdot \mathbb{H})]}{\partial \mathbb{H}} \\ &= \mu_0 \mu_r\ J\ \frac{\partial (C^{-1}_{IJ}\ H_J)}{\partial H_K}\ \mathbf{E}_I \otimes \mathbf{E}_K \\ &= \mu_0 \mu_r\ J\ C^{-1}_{IJ}\ \frac{\partial H_J}{\partial H_K}\ \mathbf{E}_I \otimes \mathbf{E}_K \\ &= \mu_0 \mu_r\ J\ C^{-1}_{IJ}\ \delta_{JK}\ \mathbf{E}_I \otimes \mathbf{E}_K \\ &= \mu_0 \mu_r\ J\ C^{-1}_{IK}\ \mathbf{E}_I \otimes \mathbf{E}_K \end{aligned}$$

$$\mathbf{D} = \mu_0 \mu_r\ J\ \mathbf{C}^{-1}. \tag{4.16}$$

The magneto-elasticity tangent tensor that defines the sensitivity of the second Piola-Kirchhoff stress $\mathbf{S}$ w.r.t. the applied referential magnetic field $\mathbb{H}$ can be derived as follows:

$$\mathbb{P} = -\frac{\partial \mathbf{S}}{\partial \mathbb{H}} = -\frac{\partial}{\partial \mathbb{H}}\left(2\frac{\partial \Psi(J,\mathbf{C},\mathbb{H})}{\partial \mathbf{C}}\right) = -2\,\frac{\partial^2 \Psi(J,\mathbf{C},\mathbb{H})}{\partial \mathbf{C}\otimes\partial \mathbb{H}}.$$

Employing the result of Equation (4.12) for $\mathbf{S}$, we have

$$\mathbb{P} = \frac{\mu_0\mu_r}{2}\,J\,\left[\mathbf{C}^{-1}\otimes\frac{\partial}{\partial\mathbb{H}}\left(\mathbf{C}^{-1}:\mathbb{H}\otimes\mathbb{H}\right)\right] - \mu_0\mu_r\,J\,\frac{\partial[(\mathbf{C}^{-1}\cdot\mathbb{H})\otimes(\mathbf{C}^{-1}\cdot\mathbb{H})]^{sym}}{\partial\mathbb{H}}.$$

Side calculation 1:

$$\begin{aligned}
\frac{\partial\left(\mathbf{C}^{-1}:\mathbb{H}\otimes\mathbb{H}\right)}{\partial\mathbb{H}} &= \frac{\partial\left(C^{-1}_{IJ}\;H_I\;H_J\right)}{\partial H_K}\mathbf{E}_K\\
&= \left[C^{-1}_{IJ}\;\delta_{IK}\;H_J + C^{-1}_{IJ}\;H_I\;\delta_{JK}\right]\;\mathbf{E}_K\\
&= \left[C^{-1}_{JI}\;\delta_{IK}\;H_J + C^{-1}_{IJ}\;\delta_{JK}\;H_I\right]\;\mathbf{E}_K\\
&= \left[C^{-1}_{JK}\;H_J + C^{-1}_{IK}\;H_I\right]\;\mathbf{E}_K\\
&= \left[C^{-1}_{KJ}\;H_J + C^{-1}_{KI}\;H_I\right]\;\mathbf{E}_K\\
&= 2[\mathbf{C}^{-1}\cdot\mathbb{H}].
\end{aligned}$$

Side calculation 2:

$$\begin{aligned}
\frac{\partial[(\mathbf{C}^{-1}\cdot\mathbb{H})\otimes(\mathbf{C}^{-1}\cdot\mathbb{H})]^{sym}}{\partial\mathbb{H}} &= \frac{1}{2}\frac{\partial\left[C^{-1}_{IM}\;H_M\;C^{-1}_{JN}\;H_N + C^{-1}_{JM}\;H_M\;C^{-1}_{IN}\;H_N\right]}{\partial H_K}\;\mathbf{E}_I\otimes\mathbf{E}_J\otimes\mathbf{E}_K\\
&= \frac{1}{2}\left[C^{-1}_{IM}\;\delta_{MK}\;C^{-1}_{JN}\;H_N + C^{-1}_{IM}\;H_M\;C^{-1}_{JN}\;\delta_{NK}\right]\;\mathbf{E}_I\otimes\mathbf{E}_J\otimes\mathbf{E}_K\\
&\quad + \frac{1}{2}\left[C^{-1}_{JM}\;\delta_{MK}\;C^{-1}_{IN}\;H_N + C^{-1}_{JM}\;H_M\;C^{-1}_{IN}\;\delta_{NK}\right]\;\mathbf{E}_I\otimes\mathbf{E}_J\otimes\mathbf{E}_K\\
&= \frac{1}{2}\left[C^{-1}_{IK}\;C^{-1}_{JN}\;H_N + C^{-1}_{IM}\;H_M\;C^{-1}_{JK}\right]\;\mathbf{E}_I\otimes\mathbf{E}_J\otimes\mathbf{E}_K\\
&\quad + \frac{1}{2}\left[C^{-1}_{JK}\;C^{-1}_{IN}\;H_N + C^{-1}_{JM}\;H_M\;C^{-1}_{IK}\right]\;\mathbf{E}_I\otimes\mathbf{E}_J\otimes\mathbf{E}_K
\end{aligned}.$$

Observing the symmetry over the indices I and J, we have

$$\begin{aligned}
&= \left[C^{-1}_{IK}\;C^{-1}_{JN}\;H_N + C^{-1}_{IM}\;H_M\;C^{-1}_{JK}\right]\;\mathbf{E}_I\otimes\mathbf{E}_J\otimes\mathbf{E}_K\\
&= \mathbf{C}^{-1}\otimes(\mathbf{C}^{-1}\cdot\mathbb{H}) + (\mathbf{C}^{-1}\cdot\mathbb{H})\otimes\mathbf{C}^{-1}
\end{aligned}$$

$$\boxed{\mathbb{P} = \mu_0\mu_r\;J\;\left[\mathbf{C}^{-1}\otimes(\mathbf{C}^{-1}\cdot\mathbb{H})\right] - \mu_0\mu_r\;J\;\left[\mathbf{C}^{-1}\otimes(\mathbf{C}^{-1}\cdot\mathbb{H}) + (\mathbf{C}^{-1}\cdot\mathbb{H})\otimes\mathbf{C}^{-1}\right].} \tag{4.17}$$

4.3 Variational formulation

The corresponding system of partial differential equations (the strong forms of the local balance equations) for each field, the scalar-valued magnetic potential field in Chapter 2 and the vector-valued displacement field for an axisymmetric solid in Chapter 3, were described in detail. The required boundary conditions to formulate a boundary-value problem were also mentioned for both the individual field (decoupled) problems. We now consider the fully-coupled problem of the (axisymmetric) magneto-elastic membrane immersed in a free space. The strong form of the complete system for the coupled problem in the total Lagrangian formulation is as follows:

$$\text{Kinematics} : \mathbb{H},\ \mathbf{F},\ \mathbf{C} := \mathbf{F}^T \cdot \mathbf{F},\ \mathbf{E} := \frac{1}{2}(\mathbf{C} - \mathbf{I}), \tag{4.18}$$

$$\text{Equilibrium} : \text{Div}\mathbb{B} = 0, \tag{4.19}$$

$$\text{Div}(\mathbf{F} \cdot \mathbf{S}) + \mathbf{b}^p = \mathbf{0}, \tag{4.20}$$

$$\text{Constitutive equation} : \mathbb{B} = -\frac{\partial \Psi(J, \mathbf{C}, \mathbb{H})}{\partial \mathbb{H}}, \tag{4.21}$$

$$\mathbf{S} = 2\frac{\partial \Psi(J, \mathbf{C}, \mathbb{H})}{\partial \mathbf{C}}. \tag{4.22}$$

The boundary conditions to be enforced for each field are:

$$\phi = \overline{\phi} \text{ on } \partial\mathcal{S}_{0,\phi}, \tag{4.23}$$

$$\mathbf{N} \cdot [\![\mathbb{B}]\!] = \overline{b} \text{ on } \partial\mathcal{S}_{0,B}, \tag{4.24}$$

$$\mathbf{u} = \mathbf{0} \text{ on } \partial\mathcal{S}_{0,\mathbf{u}}, \tag{4.25}$$

$$\mathbf{F} \cdot \mathbf{S} \cdot \mathbf{N} = \mathbf{t}^p \text{ on } \partial\mathcal{B}_{0,t}. \tag{4.26}$$

Equation (4.23) is the prescribed magnetic potential on the free space bounding surface in order to generate a magnetic field. Equation (4.24) at the bounding surface of the free space material prescribes the normal component of the referential magnetic induction vector field. This is a natural boundary condition in the undeformed configuration. Equation (4.25) is the homogeneous Dirichlet boundary condition for the displacement field. Here, the displacements on the free space boundary are constrained to zero. Equation (4.26) is the traction on the inner interface of the circular cross-section torus magneto-elastic membrane. From a mechanical perspective, this constitutes to a quasi-static inflating pressure load on the membrane and is analogous to an effect such as the air blown in a toy balloon to inflate the balloon.

Principle of stationary potential energy:
Based on the S.E.F. Equation (4.11), to derive the weak form of the governing equations,

we define the total potential energy function as

$$\Pi = \Pi_{int} + \Pi_{ext}, \tag{4.27}$$

$$\text{with } \Pi_{int} = \int_{\mathcal{D}_0} \Psi(J, \mathbf{C}, \mathbb{H})\, \mathrm{d}V = \int_{\mathcal{B}_0} \left[\Psi^{\text{elas}}(\mathbf{C}) + \mu_r M_0(J, \mathbf{C}, \mathbb{H})\right] \mathrm{d}V + \int_{\mathcal{S}_0} M_0(J, \mathbf{C}, \mathbb{H}) \mathrm{d}V, \tag{4.28}$$

$$\text{and } \Pi_{ext} = -\int_{\mathcal{B}_0} \mathbf{u} \cdot \mathbf{b}^p \mathrm{d}V - \int_{\partial\mathcal{B}_{0,t}} \mathbf{u} \cdot \mathbf{t}^p \mathrm{d}A - \int_{\partial\mathcal{S}_{0,B}} \phi \left[\mathbb{B}_\infty \cdot \mathbf{N}_\infty\right] \mathrm{d}A. \tag{4.29}$$

The internal energy contribution Equation (4.28) is a sum of total potential energy per unit volume due to the magneto-elastic material's deformation and magnetisation and the magnetic energy stored in the free space. The external energy contribution Equation (4.29) accounts for the referential mechanical body and traction forces respectively, and the last term describes the magnetic induction prescribed on the far-field boundary of the free space material. Since we do not prescribe any non-zero flux $\overline{b}$ on the boundary $\partial\mathcal{S}_{0,B}$, the last term in Π_{ext} drops out.

The stationary (saddle-)point $\min_{\mathbf{u}} \max_{\phi} \Pi \implies \delta\Pi$ describes the equilibrium solution to the coupled boundary value problem. The stationary point $\min_{\mathbf{u}} \max_{\phi} \Pi$ is that point at which all the directional derivatives of the total potential energy vanish. Using the Gâteaux derivative we have

$$\delta\Pi = \delta\Pi_{int} + \delta\Pi_{ext} = D_{\delta\mathbf{u}}\Pi_{int} + D_{\delta\phi}\Pi_{int} + D_{\delta\mathbf{u}}\Pi_{ext} + D_{\delta\phi}\Pi_{ext} = 0. \tag{4.30}$$

The components of the variation of the internal potential energy are given as [32]

$$D_{\delta\mathbf{u}}\Pi_{int} = \int_{\mathcal{D}_0} \delta\mathbf{E} : \mathbf{S}\, \mathrm{d}V, \tag{4.31}$$

$$D_{\delta\phi}\Pi_{int} = -\int_{\mathcal{D}_0} \delta\mathbb{H} \cdot \mathbb{B}\, \mathrm{d}V, \tag{4.32}$$

and that of the external potential energy are

$$D_{\delta\mathbf{u}}\Pi_{ext} = -\int_{\mathcal{B}_0} \delta\mathbf{u} \cdot \mathbf{b}^p \mathrm{d}V - \int_{\partial\mathcal{B}_{0,t}} \delta\mathbf{u} \cdot \mathbf{t}^p \mathrm{d}A, \tag{4.33}$$

$$D_{\delta\phi}\Pi_{ext} = 0. \tag{4.34}$$

The variations of the kinematic quantities are defined as

$$\delta\mathbf{F} = \nabla_0 \delta\mathbf{u}, \tag{4.35}$$

$$\delta\mathbf{E} = \left[\mathbf{F}^T \cdot \delta\mathbf{F}\right]^{\text{sym}}, \tag{4.36}$$

$$\delta\mathbb{H} = -\nabla_0 \delta\phi \quad \text{from Equation (4.1)}. \tag{4.37}$$

The second Piola-Kirchhoff stress $\mathbf{S}$ in Equation (4.31) can further be split into two components, the combined mechanical and magnetization stress within the elastic body (membrane) and the Maxwell stress contribution from the free space (non-magnetisable) material respectively, as follows:

$$\mathbf{S} = \mathbf{S}^{\text{mech+mag}} + \mathbf{S}^{\text{max}} =: 2\frac{\partial \Psi(J, \mathbf{C}, \mathbb{H})}{\partial \mathbf{C}}, \tag{4.38}$$

$$\text{with } \mathbf{S}^{\text{mech+mag}} = 2\frac{\partial \Psi^{\text{elas}}(\mathbf{C})}{\partial \mathbf{C}} + 2\left[\mu_r - 1\right]\frac{M_0(J, \mathbf{C}, \mathbb{H})}{\partial \mathbf{C}}, \tag{4.39}$$

$$\text{and } \mathbf{S}^{\text{max}} = 2\frac{M_0(J, \mathbf{C}, \mathbb{H})}{\partial \mathbf{C}}. \tag{4.40}$$

Similarly, the referential magnetic induction vector $\mathbb{B}$ in Equation (4.32) can be split into the magnetization induction within the elastic solid and the Maxwell induction in the free space material as

$$\mathbb{B} = \mathbb{B}^{\text{mag}} + \mathbb{B}^{\text{max}} =: -\frac{\partial \Psi(J, \mathbf{C}, \mathbb{H})}{\partial \mathbb{H}}, \tag{4.41}$$

$$\text{with } \mathbb{B}^{\text{mag}} = -\frac{\partial \Psi^{\text{elas}}(\mathbf{C})}{\partial \mathbb{H}} - \left[\mu_r - 1\right]\frac{M_0(J, \mathbf{C}, \mathbb{H})}{\partial \mathbb{H}}, \tag{4.42}$$

$$\text{and } \mathbb{B}^{\text{max}} = -\frac{M_0(J, \mathbf{C}, \mathbb{H})}{\partial \mathbb{H}}. \tag{4.43}$$

Equations (4.30) to (4.34) collectively represent the equivalent weak form of the equilibrium equations of our interest as mentioned in Equations (4.19) and (4.20). The continuity of the normal magnetic induction as given in Equation (4.24) at the material interfaces is also satisfied within this formulation.
The variations in Equations (4.32) and (4.33) belong to the following space

$$\delta\mathbf{u} \in H^1(\mathcal{D}_0), \quad \delta\phi \in H^1(\mathcal{D}_0), \tag{4.44}$$

with the constraints

$$\delta\mathbf{u} = \mathbf{0} \text{ on } \partial\mathcal{B}_{0,\mathbf{u}} \cup \partial\mathcal{S}_0, \quad \delta\phi = 0 \text{ on } \partial\mathcal{S}_{0,\phi}. \tag{4.45}$$

As the employed material law for the magneto-elastic material is non-linear Neo-Hookean, the linearisation of Equations (4.31) and (4.32) ($\delta\Pi_{int}$) is required within an iterative solution scheme such as the Newton-Raphson method to find the stationary point of the saddle-point system.

4.4 Linearisation of the coupled problem

Assuming the state of the system is known at some load or time step t_{n-1}, the linearisation by employing the first-order Taylor expansion of the variation of total potential

energy is given as: Find $\Delta\mathbf{u}$ and $\Delta\phi$ such that

$$\mathbf{L}\left[\delta\Pi\right]_{\phi_{i+1},\mathbf{u}_{i+1}} = \delta\Pi\Big|_{\phi_i,\mathbf{u}_i} + D_{\Delta\phi}\Big[D_{\delta\phi}\Pi_{int} + D_{\delta\mathbf{u}}\Pi_{int}\Big] + D_{\Delta\mathbf{u}}\Big[D_{\delta\phi}\Pi_{int} + D_{\delta\mathbf{u}}\Pi_{int}\Big], \quad (4.46)$$

where $\Delta\{\cdot\} := \{\cdot\}_{i+1} - \{\cdot\}_i$ is the incremental change between the iterative solver iterations i and $i+1$ and the value of a quantity at the current Newton iteration at the currently unknown load/time state t_n is denoted as $\{\cdot\}_i^n = \{\cdot\}_i$.

Assuming dead load ($\mathbf{b}^p = \mathbf{0}$), the direct terms of linearisation are given as

$$D^2_{\Delta\phi,\delta\phi}\Pi_{int} = -\int_{\mathcal{D}_0} \delta\mathbb{H}\cdot\mathbf{D}\cdot\Delta\mathbb{H}\,\mathrm{d}V, \quad (4.47)$$

$$D^2_{\Delta\mathbf{u},\delta\mathbf{u}}\Pi_{int} = \int_{\mathcal{D}_0} \Delta\delta\mathbf{E}:\mathbf{S}\,\mathrm{d}V + \int_{\mathcal{D}_0} \delta\mathbf{E}:\mathfrak{C}:\Delta\mathbf{E}\,\mathrm{d}V, \quad (4.48)$$

where $\Delta\delta\mathbf{E} = \left[\Delta\mathbf{F}^T\cdot\delta\mathbf{F}\right]^{\mathrm{sym}}$, $\mathbf{D} := \dfrac{\partial\mathbb{B}}{\partial\mathbb{H}} = -\dfrac{\partial^2\Psi(J,\mathbf{C},\mathbb{H})}{\partial\mathbb{H}\otimes\partial\mathbb{H}}$ is the rank-2 magneto-static tensor and $\mathfrak{C} := 2\dfrac{\partial\mathbf{S}}{\partial\mathbf{C}} = 4\dfrac{\partial^2\Psi(J,\mathbf{C},\mathbb{H})}{\partial\mathbf{C}\otimes\partial\mathbf{C}}$ is the referential elastic tangent as derived earlier in Equation (4.15). The detailed linearisation of the kinematical quantity $\mathbf{E}$, i.e. the Green-Lagrange strain tensor, and the constitutive equation $\mathbf{S}$, the second Piola-Kirchhoff stress tensor is already discussed in Chapter 3 and the same result applies here.

The coupled terms arising from the linearisation are

$$D^2_{\Delta\phi,\delta\mathbf{u}}\Pi_{int} = -\int_{\mathcal{D}_0} \delta\mathbf{E}:\mathbb{P}\cdot\Delta\mathbb{H}\,\mathrm{d}V, \quad (4.49)$$

$$D^2_{\Delta\mathbf{u},\delta\phi}\Pi_{int} = -\int_{\mathcal{D}_0} \delta\mathbb{H}\cdot\mathbb{P}^T:\Delta\mathbf{E}\,\mathrm{d}V, \quad (4.50)$$

where $\mathbb{P} := -\dfrac{\partial\mathbf{S}}{\partial\mathbb{H}} = -2\dfrac{\partial^2\Psi(J,\mathbf{C},\mathbb{H})}{\partial\mathbf{C}\otimes\mathbb{H}}$ and $\mathbb{P}^T := 2\dfrac{\partial\mathbb{B}}{\partial\mathbf{C}} = -2\dfrac{\partial^2\Psi(J,\mathbf{C},\mathbb{H})}{\partial\mathbb{H}\otimes\partial\mathbf{C}}$ are the referential magneto-elasticity tensors. The derived form of the different tangents is mentioned in Section 4.2.

The final linear form of Equation (4.30) can be written as

$$\begin{aligned} D_{\delta\phi}\Pi + D^2_{\Delta\phi,\delta\phi}\Pi + D^2_{\Delta\phi,\delta\mathbf{u}}\Pi &= \mathbf{0}, \\ D_{\delta\mathbf{u}}\Pi + D^2_{\Delta\mathbf{u},\delta\mathbf{u}}\Pi + D^2_{\Delta\mathbf{u},\delta\phi}\Pi &= \mathbf{0}. \end{aligned} \quad (4.51)$$

4.5 Discretization by the finite element method

We now discretize the variational form Equation (4.51) by introducing the standard Lagrangian finite element basis for the scalar-valued magnetic potential ϕ and the vector-

valued displacement $\mathbf{u}$ as

$$\phi(\mathbf{X}) \approx \phi^h(\mathbf{X}) = \sum_I \phi_I N_I(\mathbf{X}), \qquad \mathbf{u}(\mathbf{X}) \approx \mathbf{u}^h(\mathbf{X}) = \sum_I u_I \mathbf{N}_I(\mathbf{X}), \tag{4.52}$$

$$\nabla_0\phi(\mathbf{X}) \approx \nabla_0\phi^h(\mathbf{X}) = \sum_I \phi_I \nabla_0 N_I(\mathbf{X}), \quad \nabla_0\mathbf{u}(\mathbf{X}) \approx \nabla_0\mathbf{u}^h(\mathbf{X}) = \sum_I u_I \nabla_0 \mathbf{N}_I(\mathbf{X}), \tag{4.53}$$

with $\phi_I \in \mathbb{R}$ and $u_I \in \mathbb{R}$. N_I and $\mathbf{N}_I$ are, respectively, the scalar-valued and vector-valued shape functions corresponding to the global degree of freedom (support point) I. Let the collective solution vector be called as $\mathbf{d} = \{\phi; \mathbf{u}\}^T$. The shape functions belong to the Sobolev space which is defined as

$$H^1(\mathcal{D}_0; \mathbb{R}^{\dim}) = \left\{ \mathbf{d} : \mathcal{D}_0 \mapsto \mathbb{R} \Big| \int_{\mathcal{D}_0} \|\mathbf{d}\|^2 + \|\nabla \mathbf{d}\|^2 \, \mathrm{d}\mathcal{D}_0 < \infty \right\}. \tag{4.54}$$

The discrete function spaces for the solution fields are given as

$$S^h = \left\{ \phi^h \in H^1, \ \phi^h|_{\partial\mathcal{S}_{0,\phi}} = \overline{\phi^h} \right\}, \tag{4.55}$$

$$\mathbf{W}^h = \left\{ \mathbf{u}^h \in H^1, \ \mathbf{u}^h|_{\partial\mathcal{B}_{0,\mathbf{u}} \cup \partial\mathcal{S}_{0,\mathbf{u}}} = \overline{\mathbf{u}^h} \right\}. \tag{4.56}$$

The variations and linearization of the discretized fields are given as

$$\delta\phi^h(\mathbf{X}) = \sum_I \delta\phi_I N_I(\mathbf{X}), \qquad \delta\mathbf{u}^h(\mathbf{X}) = \sum_I \delta u_I \mathbf{N}_I(\mathbf{X}), \tag{4.57}$$

$$\Delta\phi^h(\mathbf{X}) = \sum_I \Delta\phi_I N_I(\mathbf{X}), \quad \Delta\mathbf{u}^h(\mathbf{X}) = \sum_I \Delta u_I \mathbf{N}_I(\mathbf{X}), \tag{4.58}$$

with $\delta\phi_I, \Delta\phi_I \in \mathbb{R}$ and $\delta u_I, \Delta u_I \in \mathbb{R}$.
The discrete function spaces for the variation of the solution fields are given as

$$T^h = \left\{ \delta\phi^h \in H^1, \ \delta\phi^h|_{\partial\mathcal{S}_{0,\phi}} = 0 \right\}, \tag{4.59}$$

$$\mathbf{V}^h = \left\{ \delta\mathbf{u}^h \in H^1, \ \delta\mathbf{u}^h|_{\partial\mathcal{B}_{0,\mathbf{u}} \cup \partial\mathcal{S}_{0,\mathbf{u}}} = \mathbf{0} \right\}. \tag{4.60}$$

The derivatives of the increments of the solution fields are given as

$$\nabla_0\Delta\phi^h(\mathbf{X}) = \sum_I \Delta\phi_I \nabla_0 N_I(\mathbf{X}), \quad \nabla_0\Delta\mathbf{u}^h(\mathbf{X}) = \sum_I \Delta u_I \nabla_0 \mathbf{N}_I(\mathbf{X}). \tag{4.61}$$

The resulting discretized system of equations for the final linearised variational form Equation (4.51) employing the results from Equations (4.31) to (4.34), Equations (4.47) to (4.50) and the definitions for the variations Equation (4.37) can be written as follows:

$$
\begin{aligned}
D^2_{\Delta\phi,\delta\phi}\Pi &= -\sum_I \sum_J \delta\phi_I \int_{\mathcal{D}_0} [\nabla_0 N_I(\mathbf{X}) \cdot \mathbf{D} \cdot \nabla_0 N_J(\mathbf{X})] \cdot \Delta\phi_J \, \mathrm{d}V, \\
D^2_{\Delta\phi,\delta\mathbf{u}}\Pi &= \sum_I \sum_J \delta u_I \int_{\mathcal{D}_0} \left[\left[\mathbf{F}^T \cdot \nabla_0 \mathbf{N}_I(\mathbf{X})\right] : \mathbb{P} \cdot \nabla_0 N_J(\mathbf{X})\right] \cdot \Delta\phi_J \, \mathrm{d}V, \\
D^2_{\Delta\mathbf{u},\delta\phi}\Pi &= \sum_I \sum_J \delta\phi_I \int_{\mathcal{D}_0} \left[\nabla_0 N_I(\mathbf{X}) \cdot \mathbb{P}^T : \left[\mathbf{F}^T \cdot \nabla_0 \mathbf{N}_J(\mathbf{X})\right]\right] \cdot \Delta u_J \, \mathrm{d}V, \\
D^2_{\Delta\mathbf{u},\delta\mathbf{u}}\Pi &= \sum_I \sum_J \delta u_I \int_{\mathcal{D}_0} \left[\left[\nabla_0 \mathbf{N}_I^T(\mathbf{X}) \cdot \nabla_0 \mathbf{N}_J(\mathbf{X})\right]^{\mathrm{sym}} : \mathbf{S}\right] \cdot \Delta u_J \, \mathrm{d}V \\
&\quad + \sum_I \sum_J \delta u_I \int_{\mathcal{D}_0} \left[\left[\mathbf{F}^T \cdot \nabla_0 \mathbf{N}_I(\mathbf{X})\right]^{\mathrm{sym}} : \mathfrak{C} : \left[\mathbf{F}^T \cdot \nabla_0 \mathbf{N}_J(\mathbf{X})\right]^{\mathrm{sym}}\right] \cdot \Delta u_J \, \mathrm{d}V.
\end{aligned}
\tag{4.62}
$$

$$
\begin{aligned}
D_{\delta\mathbf{u}}\Pi_{int} &= -\sum_I \delta u_I \int_{\mathcal{D}_0} \left[\left[\mathbf{F}^T \cdot \nabla_0 \mathbf{N}_I(\mathbf{X})\right]^{\mathrm{sym}} : \mathbf{S}\right] \, \mathrm{d}V, \\
D_{\delta\mathbf{u}}\Pi_{ext} &= \sum_I \delta u_I \int_{\partial\mathcal{B}_{0,t}} [\mathbf{N}_I(\mathbf{X}) \cdot \mathbf{t}^p] \, \mathrm{d}A, \\
D_{\delta\phi}\Pi &= -\sum_I \delta\phi_I \int_{\mathcal{D}_0} [\nabla_0 N_I(\mathbf{X}) \cdot \mathbb{B}] \, \mathrm{d}V.
\end{aligned}
\tag{4.63}
$$

The resulting discretized Equations (4.62) and (4.63) must hold for all arbitrary variations $\delta\phi_I$ and δu_I. The algebraic system to be solved at time/load step t_n and Newton iterate i is

$$
\begin{bmatrix} \mathbf{K}_{\phi\phi} & \mathbf{K}_{\phi\mathbf{u}} \\ \mathbf{K}_{\mathbf{u}\phi} & \mathbf{K}_{\mathbf{uu}} \end{bmatrix} \begin{bmatrix} \Delta\mathbf{d}_\phi \\ \Delta\mathbf{d}_\mathbf{u} \end{bmatrix} = \begin{bmatrix} -\mathbf{R}_\phi \\ -\mathbf{R}_\mathbf{u} \end{bmatrix} \implies \mathbf{K} \cdot \Delta\mathbf{d} = -\mathbf{R}. \tag{4.64}
$$

The solution update is then performed as follows

$$
\mathbf{d}^n_{i+1} = \mathbf{d}^n_i + \Delta\mathbf{d}^n. \tag{4.65}
$$

Applying the Gauss quadrature rule for the numerical integration and also considering the transformation needed for the axisymmetric formulation (as previously discussed in

Chapter 2 and Chapter 3), the final cell wise FE assembly is given as follows:

$$\begin{aligned} K_{IJ} = &- \sum_q \left[\nabla_0 N_I(q) \cdot \mathbf{D} \cdot \nabla_0 N_J(q)\right] \ \alpha \ J \ w(q) \\ &+ \sum_q \left[\left[\mathbf{F}^T \cdot \nabla_0 \mathbf{N}_I(q)\right] : \mathbb{P} \cdot \nabla_0 N_J(q)\right] \ \alpha \ J \ w(q) \\ &+ \sum_q \left[\nabla_0 N_I(q) \cdot \mathbb{P}^T : \left[\mathbf{F}^T \cdot \nabla_0 \mathbf{N}_J(q)\right]\right] \ \alpha \ J \ w(q) \\ &+ \sum_q \left[\left[\nabla_0 \mathbf{N}_I^T(q) \cdot \nabla_0 \mathbf{N}_J(q)\right]^{\text{sym}} : \mathbf{S}\right] \ \alpha \ J \ w(q) \\ &+ \sum_q \left[\left[\mathbf{F}^T \cdot \nabla_0 \mathbf{N}_I(q)\right]^{\text{sym}} : \mathfrak{C} : \left[\mathbf{F}^T \cdot \nabla_0 \mathbf{N}_J(q)\right]^{\text{sym}}\right] \ \alpha \ J \ w(q), \end{aligned} \tag{4.66}$$

and with $\mathbf{f} := -\mathbf{R}$

$$\begin{aligned} f_I = &- \sum_q \left[\left[\mathbf{F}^T \cdot \nabla_0 \mathbf{N}_I(q)\right]^{\text{sym}} : \mathbf{S}\right] \ \alpha \ J \ w(q) \\ &- \sum_q \left[\nabla_0 N_I(q) \cdot \mathbb{B}\right] \ \alpha \ J \ w(q) \\ &+ \sum_{q \in \mathcal{B}_0} \left[\mathbf{N}_I(q) \cdot \mathbf{t}^p\right] \ \alpha \ J \ w(q), \end{aligned} \tag{4.67}$$

where q are the local quadrature points with corresponding weights $w(q)$ and the scalar $\alpha := 2\pi R$ is the co-ordinate scaling factor arising from the transformation of the 3D integrals to the axisymmetric (2.5D) integrals. R is the axial component of the distance of the local quadrature point q from the axis of symmetry. Equations (4.66) and (4.67) represents the final FE assembly we have implemented for the axisymmetric fully-coupled magneto-elastic problem of our interest.

4.6 Implementation details

4.6.1 Saddle point system

At any Newton iteration i and time/load step t_n the algebraic equations to solve are as represented in Equation (4.64). Consider the scalar-valued magnetic potential solution block vector $\mathbf{d}_\phi$ be of size p and the vector-valued displacement solution block vector $\mathbf{d}_\mathbf{u}$ for an axisymmetric formulation be of size q. Then the total number of unknowns, called as number of global DoFs, will be $n_{dofs} = p + q$. For the case where the same order finite elements are employed for both the fields, for e.g., for a total number of support points n_d, for linear Lagrange finite element (Q_1) used for the solution field ϕ with $p = n_d$ and bi-linear Lagrange finite elements ($Q_1 \times Q_1$) for the solution field $\mathbf{u}$

with $q = 2n_d$, then the total number of unknowns would be $n_{dofs} = 3n_d$. By definition, a support point is a point p_i such that for a shape function N_j (finite element families based on the Lagrange interpolation) it holds $N_j(p_i) = \delta_{ij}$. The corresponding tangent matrix blocks will be of the following dimensions:

$$\mathbf{K}_{\phi\phi} \in \mathbb{R}^{p\times p},\ \mathbf{K}_{\phi\mathbf{u}} \in \mathbb{R}^{p\times q},\ \mathbf{K}_{\mathbf{u}\phi} \in \mathbb{R}^{q\times p},\ \mathbf{K}_{\mathbf{uu}} \in \mathbb{R}^{q\times q}. \tag{4.68}$$

The block system of equations in Equation (4.64) represents a saddle point system for the coupled multi-physics problem of our interest. Saddle point systems arise when a certain quantity such as the energy of a continuum body has to be minimized, subject to a set of linear constraints. The constraints typically represent some basic conservation law such as the balance law of linear momentum in our case of non-linear solid mechanics. Because saddle point systems can be derived as equilibrium conditions for a physical system, they are sometimes also referred to a *equilibrium equations* [10]. We therefore briefly discuss the saddle point systems.

A general block system

$$\begin{bmatrix}\mathbf{A} & \mathbf{B}\\ \mathbf{C} & \mathbf{D}\end{bmatrix}\begin{bmatrix}\mathbf{x}\\ \mathbf{y}\end{bmatrix} = \begin{bmatrix}\mathbf{f}\\ \mathbf{g}\end{bmatrix} \implies \mathbf{K}\cdot\mathbf{v} = \mathbf{s} \tag{4.69}$$

equivalent to Equation (4.64) can be classified as a (generalized) saddle point problem [10]. Consider the following minimization problem:

$$M(\mathbf{v}) = \frac{1}{2}\langle \mathbf{K}\cdot\mathbf{v}, \mathbf{v}\rangle - \langle \mathbf{s}, \mathbf{v}\rangle, \tag{4.70}$$

subject to

$$\mathbf{C}\cdot\mathbf{x} = \mathbf{g}, \tag{4.71}$$

with $\langle\cdot,\cdot\rangle$ denoting the standard inner product in $\mathbb{R}^{p+q}$. Note that

$$\nabla M(\mathbf{v}) = \mathbf{K}\cdot\mathbf{v} - \mathbf{s}. \tag{4.72}$$

Any solution $(\mathbf{x}_*, \mathbf{y}_*)^T$ of the general case Equation (4.69), is a saddle point of the Lagrangian defined as

$$\mathcal{L}(\mathbf{x},\mathbf{y}) = \frac{1}{2}\langle \mathbf{K}\cdot\mathbf{v}, \mathbf{v}\rangle - \langle \mathbf{s}, \mathbf{v}\rangle + (\mathbf{C}\cdot\mathbf{x} - \mathbf{g})^T\cdot\mathbf{y}. \tag{4.73}$$

The saddle point $(\mathbf{x}_*, \mathbf{y}_*)^T \in \mathbb{R}^{p+q}$ satisfies

$$\mathcal{L}(\mathbf{x}_*, \mathbf{y}) \le \mathcal{L}(\mathbf{x}_*, \mathbf{y}_*) \le \mathcal{L}(\mathbf{x}, \mathbf{y}_*)\ \forall \mathbf{x} \in \mathbb{R}^p\ \&\ \forall \mathbf{y} \in \mathbb{R}^q, \tag{4.74}$$

or equivalently,

$$\min_{\mathbf{x}}\max_{\mathbf{y}} \mathcal{L}(\mathbf{x},\mathbf{y}) = \mathcal{L}(\mathbf{x}_*,\mathbf{y}_*) = \max_{\mathbf{x}}\min_{\mathbf{y}} \mathcal{L}(\mathbf{x},\mathbf{y}). \tag{4.75}$$

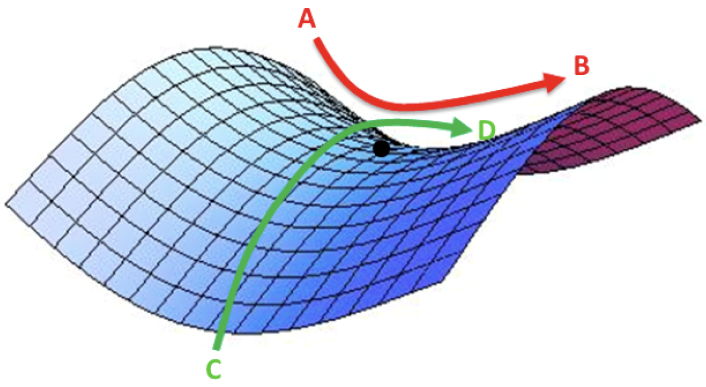

Figure 4.2: Saddle point over a 3D surface [37]

A better understanding of Equations (4.74) and (4.75) can be observed in Figure 4.2. Depending upon how one cuts the surface moving along the direction A to B or from C to D (orthogonal direction to A to B), the critical point looks like a local minima or a local maxima, but in reality it is neither. It is a saddle point.

Equation (4.64) for the coupled multi-physics problem of magneto-elastic membrane in free space is a special case of the (generalized) saddle point system. Here, we minimize for the displacement field $\mathbf{u}$ and maximize for the magnetic scalar potential ϕ.

4.6.2 Numerical solution of block systems

To solve the linear system of equations Equation (4.64), one of the following approach can be taken:

- Direct solver solving the complete system monolithically.
- Global iterative solver with a global preconditioner constructed for the tangent matrix $\mathbf{K}$.
- Sequentially solve for each unknown field ϕ and $\mathbf{u}$ exploiting the tangent matrix's block structure.

Below we explain the direct solver and the iterative solution method exploiting the block structure that were implemented. Before we discuss the details of the solution methods, it is important to highlight the properties of each block in the tangent matrix $\mathbf{K}$. This will also explain the motive for the choice of block to proceed with iterative solution method detailed in the further section.

As observed in the finite element discretized form for the coupled problem, the block for purely magnetic scalar potential contribution $\mathbf{K}_{\phi\phi} = -\int_{\mathcal{D}_0} \nabla_0 N_I \cdot \mathbf{D} \cdot \nabla_0 N_J$ results in

a symmetric negative-definite matrix of size $p \times p$. The block for purely non-linear elastic contribution $\mathbf{K_{uu}} = \int\limits_{\mathcal{D}_0} \left[\left[\nabla_0^T \mathbf{N}_I \cdot \nabla_0 \mathbf{N}_J\right] : \mathbf{S} + \left[\mathbf{F}^T \cdot \nabla_0 \mathbf{N}_I\right] : \mathfrak{C} : \left[\mathbf{F}^T \cdot \nabla_0 \mathbf{N}_J\right]\right]$ represents a symmetric positive-definite matrix of size $q \times q$. For the considered axisymmetric problem, we know that for any given total number of support points n_d, $p < q$ given that we solve for a single scalar-valued magnetic potential ϕ and a vector-valued displacement $(u_r, u_z)^T$. Thus, the size of block $\mathbf{K}_{\phi\phi}$ is always less than the block $\mathbf{K_{uu}}$ (unless we solve for a 1D problem). The blocks resulting from the coupling between the two fields, namely $\mathbf{K}_{\phi\mathbf{u}}$ and $\mathbf{K}_{\mathbf{u}\phi}$ are matrices with sizes $p \times q$ and $q \times p$, respectively and are transposes of each other. Thus, one can assemble one block and store the other as the transpose of the assembled block to save computations. Due to the sparsity arising in each individual block, the structure of the tangent matrix $\mathbf{K}$ is an unsymmetric sparse banded block matrix.

4.6.2.1 Direct solver

This category of solvers is also known as '*coupled*' or 'all at once' methods. Coupled solvers deal with the system such as Equation (4.64) as a whole, computing both the fields ϕ and $\mathbf{u}$ simultaneously and without making any explicit use of reduced systems. In most cases, due to the ease of implementation, the direct solver is employed. One doesn't have to care about the properties of the tangent matrix $\mathbf{K}$ and also about the properties of individual blocks.

We use a sparse direct solver called UMFPACK [7], which is part of the SuiteSparse library [30]. Interface to this solver is provided in the `deal.II` [39] library in the form of the class SparseDirectUMFPACK. UMFPACK is a set of routines for solving unsymmetric sparse linear systems of the form $\mathbf{A} \cdot \mathbf{x} = \mathbf{b}$. It employs the unsymmetric multifrontal method and direct sparse LU factorization. It is heavily used as a built-in routine in MATLAB® and appears as lu and $\mathbf{x} = \mathbf{A} \setminus \mathbf{b}$ (backslash operator). It is important to note that this solver is a serial solver and therefore one cannot employ parallel (MPI) data structures for the vectors and reap the benefits of distributed memory parallelism for a large system of equations. Thus, the solution time for a large system using such a serial direct solver would be high compared to a parallelized iterative solver in most cases. But for our problem of interest, in the axisymmetric formulation it was observed that the computation time for the total solution was comparable to that of a parallelized iterative solver mentioned in the next section.

4.6.2.2 Segregated iterative solver using Schur complement reduction

The other category of solvers is the so called segregated solver which computes both the unknown fields ϕ and $\mathbf{u}$ separately. This approach involves the solution of two linear systems of size smaller than $p + q$ which are termed as *reduced systems*. One reduced system is formed for the field ϕ and the other reduced system for the field $\mathbf{u}$. Depending upon the number of unknown fields, for example, in cases of a Lagrange multiplier, a

separate reduced system for that unknown field is also formed and solved. Here, we shall look at one of the representatives of such a segregated approach known as the Schur complement reduction which we implemented for the solution of the fully-coupled magneto-elastic problem of our interest.

The Schur complement reduction is based on the Gauss elimination of the sparse block tangent matrix $\mathbf{K}$. Consider the saddle point system of our interest from Equation (4.64):

$$\mathbf{K}_{\phi\phi} \cdot \Delta\mathbf{d}_{\phi} + \mathbf{K}_{\phi\mathbf{u}} \cdot \Delta\mathbf{d}_{\mathbf{u}} = -\mathbf{R}_{\phi}, \quad \mathbf{K}_{\mathbf{u}\phi} \cdot \Delta\mathbf{d}_{\phi} + \mathbf{K}_{\mathbf{uu}} \cdot \Delta\mathbf{d}_{\mathbf{u}} = -\mathbf{R}_{\mathbf{u}}. \tag{4.76}$$

The matrix $\mathbf{S}$ called the Schur complement of block $\mathbf{K}_{\phi\phi}$ in $\mathbf{K}$ is defined as

$$\mathbf{S} = \mathbf{K}_{\mathbf{uu}} - \mathbf{K}_{\mathbf{u}\phi}\mathbf{K}_{\phi\phi}^{-1}\mathbf{K}_{\phi\mathbf{u}} \equiv \mathbf{D} - \mathbf{C}\mathbf{A}^{-1}\mathbf{B} \text{ from Equation (4.69).} \tag{4.77}$$

With the magnetic potential stiffness block $\mathbf{K}_{\phi\phi}$ and the total stiffness matrix $\mathbf{K}$ being square and invertible, the Schur complement $\mathbf{S}$ is also invertible. Pre-multiplying both the sides of the first equation in Equation (4.76) by $\mathbf{K}_{\mathbf{u}\phi}\mathbf{K}_{\phi\phi}^{-1}$, we obtain

$$\mathbf{K}_{\mathbf{u}\phi} \cdot \Delta\mathbf{d}_{\phi} + \mathbf{K}_{\mathbf{u}\phi}\mathbf{K}_{\phi\phi}^{-1}\mathbf{K}_{\phi\mathbf{u}} \cdot \Delta\mathbf{d}_{\mathbf{u}} = -\mathbf{K}_{\mathbf{u}\phi}\mathbf{K}_{\phi\phi}^{-1} \cdot \mathbf{R}_{\phi}. \tag{4.78}$$

Using $\mathbf{K}_{\mathbf{u}\phi} \cdot \Delta\mathbf{d}_{\phi} = -\mathbf{R}_{\mathbf{u}} - \mathbf{K}_{\mathbf{uu}} \cdot \Delta\mathbf{d}_{\mathbf{u}}$ from the second equation in Equation (4.76), after rearranging we see

$$\left(\mathbf{K}_{\mathbf{uu}} - \mathbf{K}_{\mathbf{u}\phi}\mathbf{K}_{\phi\phi}^{-1}\mathbf{K}_{\phi\mathbf{u}}\right) \cdot \Delta\mathbf{d}_{\mathbf{u}} = \mathbf{K}_{\mathbf{u}\phi}\mathbf{K}_{\phi\phi}^{-1} \cdot \mathbf{R}_{\phi} - \mathbf{R}_{\mathbf{u}} \implies \mathbf{S} \cdot \Delta\mathbf{d}_{\mathbf{u}} = \mathbf{R}_{\mathbf{u}}^{'}, \tag{4.79}$$

with the modified right-hand side vector $\mathbf{R}_{\mathbf{u}}^{'} := \mathbf{K}_{\mathbf{u}\phi}\mathbf{K}_{\phi\phi}^{-1} \cdot \mathbf{R}_{\phi} - \mathbf{R}_{\mathbf{u}}$ arising from the condensation step. In terms of the general representation as in Equation (4.69), we arrive at

$$\left(\mathbf{D} - \mathbf{C}\mathbf{A}^{-1}\mathbf{B}\right) \cdot \mathbf{y} = \mathbf{g} - \mathbf{C}\mathbf{A}^{-1}\mathbf{f} \implies \mathbf{S} \cdot \mathbf{y} = \mathbf{g}^{'}. \tag{4.80}$$

Equations (4.79) and (4.80) represent a reduced system of order q for the solution update in displacement field $\Delta\mathbf{d}_{\mathbf{u}}$. It is important to note that unless $-\mathbf{R}_{\phi} \equiv \mathbf{f} = \mathbf{0}$, pre-processing the condensed right-hand side vector $\mathbf{R}_{\mathbf{u}}^{'} \equiv \mathbf{g}^{'}$ requires solving another linear system of equation of the form $\mathbf{A} \cdot \mathbf{v} = \mathbf{f}$. Once the solution (or an approximation) $\Delta\mathbf{d}_{\mathbf{u}}$ of the reduced system Equation (4.79) is computed, we then post-process the solution update for the other field $\Delta\mathbf{d}_{\phi}$ using the solution from the first update $\Delta\mathbf{d}_{\mathbf{u}}$ as

$$\mathbf{K}_{\phi\phi} \cdot \Delta\mathbf{d}_{\phi} = -\mathbf{R}_{\phi} - \mathbf{K}_{\phi\mathbf{u}} \cdot \Delta\mathbf{d}_{\mathbf{u}}. \tag{4.81}$$

Equation (4.81) represents the other reduced system of size p that needs to be solved for the magnetic potential solution update. Algorithm 4.1 highlights the algorithmic steps needed to solve any saddle point system using the segregated iterative solver. The algorithm is explained for the fully-coupled magneto-elastic problem of our interest, solving for the displacement field first and then for the magnetic potential, but can be applied for any general saddle point system such as Equation (4.69).

Algorithm 4.1: SCHUR COMPLEMENT REDUCTION

1. Define the inverse $\mathbf{K}_{\phi\phi}^{-1}$ using a solver with preconditioner.
2. Define the Schur complement $\mathbf{S} = \mathbf{K}_{\mathbf{uu}} - \mathbf{K}_{\mathbf{u}\phi}\mathbf{K}_{\phi\phi}^{-1}\mathbf{K}_{\phi\mathbf{u}}$.
3. Define the inverse of the Schur complement $\mathbf{S}^{-1}$ using another solver with a preconditioner to compute the approximate inverse operation of $\mathbf{S}$.
4. Perform the pre-processing step to condense the right-hand side vector $\mathbf{R}_{\mathbf{u}}^{'} := \mathbf{K}_{\mathbf{u}\phi}\mathbf{K}_{\phi\phi}^{-1} \cdot \mathbf{R}_{\phi} - \mathbf{R}_{\mathbf{u}}$.
5. Solve for the solution update $\Delta\mathbf{d}_{\mathbf{u}}$: $\Delta\mathbf{d}_{\mathbf{u}} = \mathbf{S}^{-1} \cdot \mathbf{R}_{\mathbf{u}}^{'}$.
6. Post-process the solution for the other field: $\Delta\mathbf{d}_{\phi} = \mathbf{K}_{\phi\phi}^{-1}\left(-\mathbf{R}_{\phi} - \mathbf{K}_{\phi\mathbf{u}} \cdot \Delta\mathbf{d}_{\mathbf{u}}\right)$.

Choice of the block to compute the Schur complement of K:

The choice of the block $\mathbf{K}_{\phi\phi}$ of size $p \times p$ to proceed with the Schur complement of $\mathbf{K}$ is due to the small size of the block compared to the other diagonal block $\mathbf{K}_{\mathbf{uu}}$ of size $q \times q$, with $p < q$ as mentioned in the previous section. The motive behind the choice of the block of small size is the need to compute the inverse of the chosen block in computing the Schur complement $\mathbf{S}$ as observed in Equation (4.77). Computational cost of computing the inverse of a matrix of size $q \times q$ exceeds that of the cost for a matrix of size $p \times p$. One also needs to take into account the lower bandwidth of the scalar magnetic potential stiffness matrix block compared to that of the displacement stiffness matrix block [36].

Typically this inversion of the chosen block matrix is performed by using a robust Krylov subspace iterative solver such as the Conjugate Gradient method with some form of preconditioning. The CG method works on only symmetric positive-definite matrices [25]. Whereas the block $\mathbf{K}_{\phi\phi}$ and $\mathbf{K}_{\phi\mathbf{u}}$ of the first equation in Equation (4.76) are symmetric negative-definite matrices. In order to compute the inverse $\mathbf{K}_{\phi\phi}^{-1}$ using the CG iterative solver we need to transform the matrix $\mathbf{K}_{\phi\phi}$ to a positive-definite matrix. We do this by multiplying the first equation in Equation (4.76) by a factor of -1. This leads to a system of equations as

$$-\mathbf{K}_{\phi\phi} \cdot \Delta\mathbf{d}_{\phi} - \mathbf{K}_{\phi\mathbf{u}} \cdot \Delta\mathbf{d}_{\mathbf{u}} = \mathbf{R}_{\phi}, \tag{4.82}$$

with symmetric positive-definite matrix blocks. The matrix block $\mathbf{K}_{\phi\phi}$ is preconditioned to reduce the condition number and thus have a good convergence rate within the iterative solver computing an approximation to the inverse $\mathbf{K}_{\phi\phi}^{-1}$. We have employed the Trilinos [12] linear algebra suite for the parallel and efficient data structures of vectors,

matrices, preconditioners and solvers. Jacobi, SSOR and the Algebraic Multigrid (AMG) [14] preconditioners were used from the Trilinos suite. Depending on a user input parameter one of the three would be used. To compute the inverse $\mathbf{K}_{\phi\phi}^{-1}$ a reduced-iteration CG solver was employed. The linear transformations such as the scaling of matrix with a factor of -1, forming the inverse operator $\mathbf{K}_{\phi\phi}^{-1}$ and the Schur complement $\mathbf{S}$ was carried out using the class LinearOperator from the `deal.II` library. Lazy evaluation of linear transformations and expressions using vectors and matrices is performed by this class. The lazy evaluation of an expression helps in avoiding any intermediate storage of temporary objects. The class stores the sequence of operations that need to be performed on the vector/matrix object and executes them only when the value of the object is required. The class LinearOperator provides several member functions that aid the user implementing a Schur complement reduction solver. The member function linear_operator() was used on each block of the tangent matrix $\mathbf{K}$ to transform the underlying Trilinos sparse matrix to a LinearOperator data structure. The function inverse_operator(), which takes the matrix of which inverse is to be computed, the iterative linear solver and the preconditioner for the matrix as arguments, was employed to form the inverse operator $\mathbf{K}_{\phi\phi}^{-1}$. The Schur complement was defined using the member function schur_complement() which takes the four matrix blocks as arguments required to define the Schur complement $\mathbf{S} := \mathbf{D} - \mathbf{C}\mathbf{A}^{-1}\mathbf{B}$.

Another reduced-iteration CG solver was used with one of the three precondtioner to define the inverse operator for the Schur complement $\mathbf{S}^{-1}$. To pre-process the condensed right-hand side vector as mentioned in Algorithm 4.1, the member function condense_schur_rhs() of the class LinearOperator was employed. To post-process the solution update for the second field the member function postprocess_schur_solution() was employed. Thus, in total two different iterative solvers with respective preconditioners were implemented within the Schur complement reduction method. An inner solver to compute $\mathbf{K}_{\phi\phi}^{-1}$ and an outer solver to compute $\mathbf{S}^{-1}$.

4.7 Problem set up

4.7.1 Set up for the magnetic field $\mathbb{H}$

Following the results obtained in Chapter 2 and Chapter 3, the problem set up for the coupled magneto-elasticity problem is updated in view of modelling the instabilities arising in the torus membrane. The same geometry of the axisymmetric torus membrane immersed in free space is used as in the Chapter 2 and Chapter 3.

In Chapter 2 of the thesis (a purely magneto-static problem), we considered a rectangular permanent magnet placed at the center and along the axis of symmetry to generate a circulating magnetic field $\mathbb{H}$ in $\mathcal{D}_0$. A linearly varying potential function was applied to this permanent magnet region, c.f. Figure 4.4a. The dimension of this rectangular permanent magnet region and the potential difference per unit length to be applied were

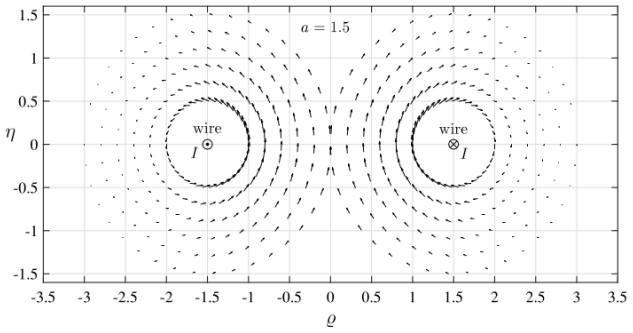

(a) Desired distribution [38]

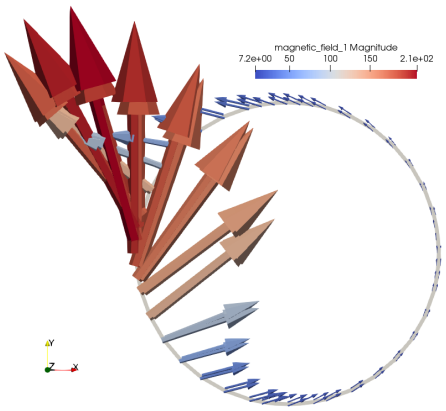

(b) Modelled distribution

Figure 4.3: Resulting magnetic field in torus membrane

taken as user input parameters. It was observed in the results for Chapter 2 that the size of the magnet and the potential applied influenced the resulting magnetic field generated in the domain. A small study for this was also carried out and presented in Chapter 2. The important finding of this study was that the direction of the resulting magnetic field in the tours membrane did not change irrespective of increasing the magnet size and the applied potential value. The resulting magnetic field, c.f. Figure 4.3b, in the torus membrane on the left section (in close proximity to the permanent magnet and axis of symmetry) was comparatively high in magnitude than on the other sections of the membrane. The orientation of this large magnetic field on the left section was the same as that observed on the right section. The orientation of the magnetic field did not meet the desired result as observed in Figure 4.3a from [38]. The main reason for this discrepancy was the different modelling approach taken by us to generate the magnetic field compared to the approach taken in [38]. In [38], a thin current carrying wire placed along the centre line of the torus membrane was considered to generate the field $\mathbb{H}$. This approach is not possible from the perspective of finite element modelling and thus we had employed a permanent magnet region to generate a similar effect.

Due to such a concentrated magnetic field on one section of the membrane, modelling of instabilities arising from the coupled mechanical and magnetic static loading would not be possible. The instability behaviour of our interest is witnessed at large mechanical loads and under an uniformly distributed magnetic field of large magnitude [38, 41]. Thus, to generate a uniformly distributed magnetic field in the coupled problem and to study the instabilities, a different approach was undertaken. In the new approach, we considered the top and bottom boundary of the free space $\partial\mathcal{S}_0$ as the south and the north pole of a permanent magnet, respectively. A constant potential $\overline{\phi}$ of same magnitude but opposite polarities was prescribed at the top and the bottom boundary as observed in Figure 4.4b. The resulting magnetic field in Figure 4.5b is uniformly

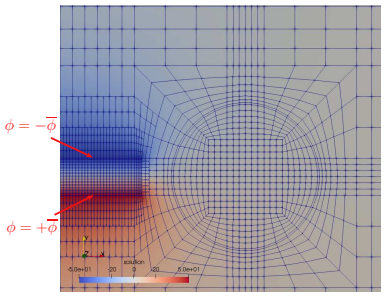

(a) Permanent magnet used in Chapter 2 (purely magneto-static problem)

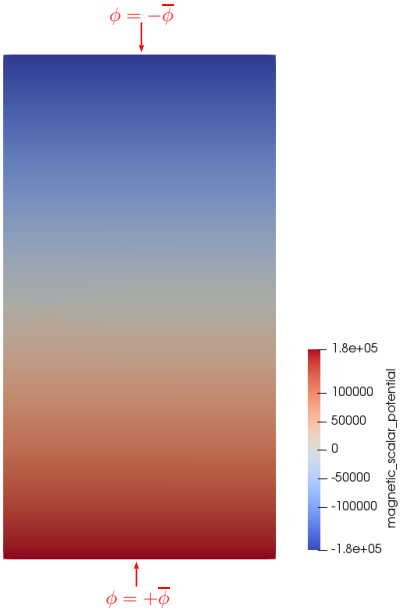

(b) For the coupled problem

Figure 4.4: Applied potential difference per unit length

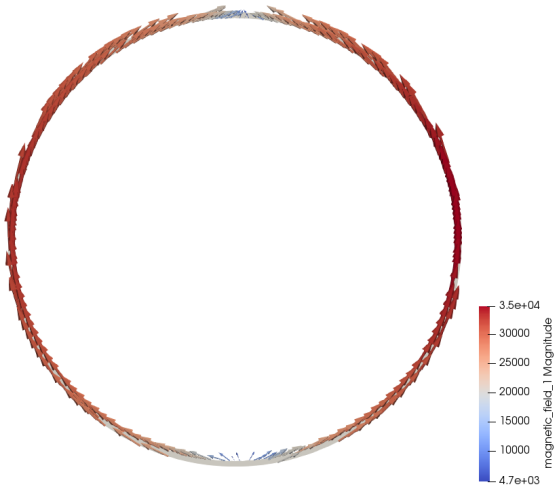

(a) Modelled distribution of $\mathbb{H}$ in torus membrane (in the undeformed configuration)

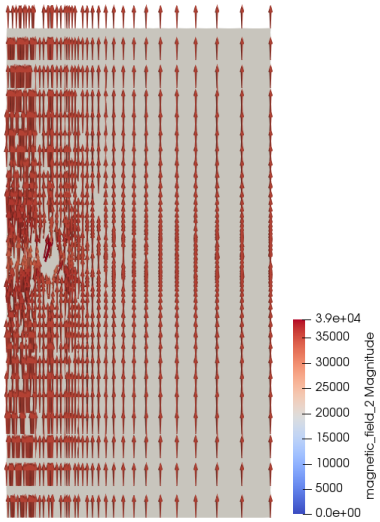

(b) Uniformly distributed magnetic field in $\mathcal{D}_0$

Figure 4.5: Resulting magnetic field $\mathbb{H}$ for the coupled problem (Vectors are coloured and scaled to the magnitude of the magnetic field $\mathbb{H}$)

distributed in the far-field region and vertically aligned. The important outcome of this approach, comparing Figure 4.5a to Figure 4.3b, is the absence of a concentrated

magnetic field of high magnitude on any section of the torus membrane. Using the new approach we were able to generate a more equally distributed magnetic field in the torus membrane. Comparing the modelled distribution in Figure 4.5a with the desired distribution in Figure 4.3a, we were able to generate a more equally distributed tangential field. This will prove more suitable to study the instability behaviour under a quasi-static mechanical load.

4.7.2 Problem geometry and load application set up

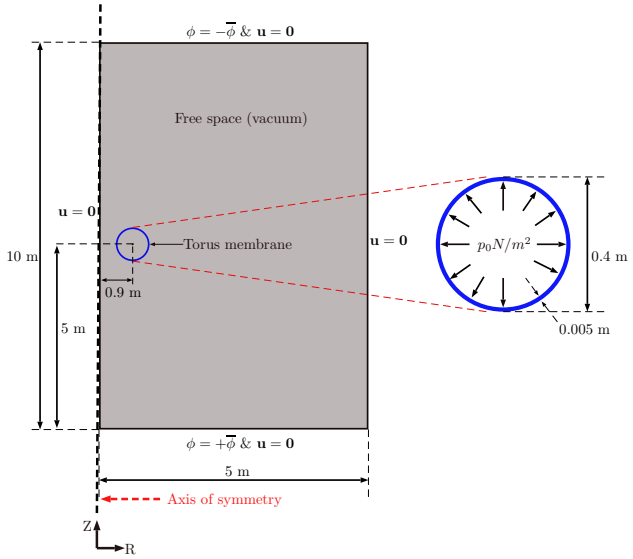

(a) Representative geometry description

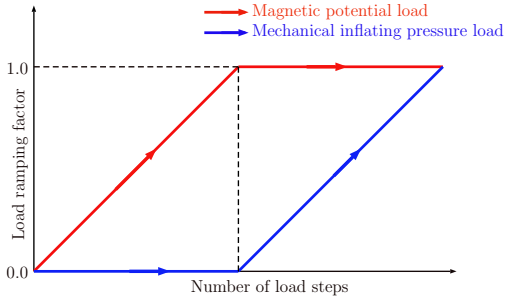

(b) Load application cycle

Figure 4.6: Coupled problem geometry and applied load set up

The problem geometry shown in Figure 4.6a is same as used in Chapter 2 and Chapter 3. However, now along with the finite elastic deformations of the circular cross-section torus membrane, we also model the magnetic scalar potential problem and study the coupled finite strain magneto-elastic deformations of this membrane immersed in the surrounding free space. The interactions between the displacement and magnetic fields and the response of the material for the coupled loads will be examined. We consider the external load application in uniformly increasing load steps as shown in Figure 4.6b. For the study of instabilities arising due to coupled loads, following [38], we first apply the scalar magnetic potential load $\phi = \overline{\phi}$ on the far-field free space boundary $\partial\mathcal{S}_0$ in the first half of the total number of load steps. The magnetic potential is increased linearly until the total desired magnetic potential is reached. In the next half of the total load cycle, the externally applied magnetic potential is kept constant. Thus, the established magnetic field $\mathbb{H}$ from the first half load cycle remains constant in the second half cycle. A uniformly distributed inflating pressure load is applied on the inner interface of the torus

magneto-elastic membrane as observed in Figure 4.6a. No mechanical load is applied in the first half of the total load application cycle. The mechanical inflating load is linearly increased with each load step in the second half of the remaining load steps until the total desired mechanical load value is reached. To model the instability behaviour with a simple set up and obtain initial understanding of the physics, we avoid the complex combined increasing load application here. Once the desired unstable deformations for a simple set up is achieved, one can then increase the complexities considered in the modelling and examine the behaviour.

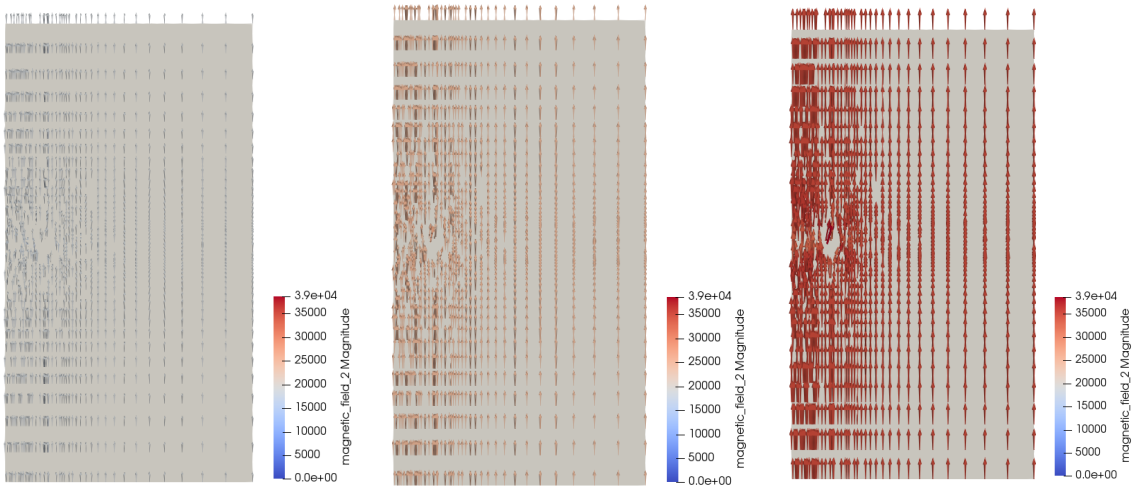

(a) Load step 25 (b) Load step 35 (c) Load step 50 (Half load)

Figure 4.7: Magnetic field $\mathbb{H}$ increasing with each load step in first half of the total load application cycle

The resulting magnetic field is observed in Figures 4.7a to 4.7c. One can observe the resulting magnetic field in the far-field region is uniformly distributed and equal in magnitude. The field in the region neighbouring the torus membrane is more involved and not aligned in the vertical direction exactly, rather we observe it to be tangential to the circular cross-section membrane. As already stated, we observe the quadratic convergence of Newton solver only in close vicinity to the solution. The main advantage of the approach of linearly increasing the applied magnetic potential in small increments is that for each small increment the non-linear Newton solver would converge to a solution. Whereas if one were to apply such a large magnetic load in a single load step, we would observe no convergence and no solution corresponding to this large load value.

4.8 Test model and results

A unit test was set up for the coupled problem with load application cycle mentioned in Section 4.7.2. Referring to Figure 4.8a, the boundary along the axis of symmetry

and the bottom horizontal boundary has a sliding constraint for the displacement field. We prescribe the top boundary with a negative magnetic potential and the bottom boundary with an equal magnitude positive magnetic potential, c.f. Figure 4.8b. A uniformly distributed mechanical traction load was applied on the top boundary of the unit cube.

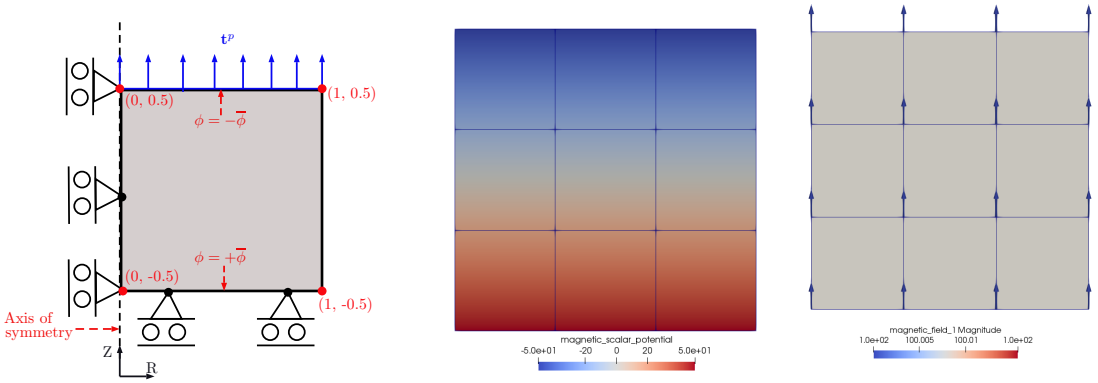

(a) Representative geometry (b) Prescribed potential ϕ (c) Resulting $\mathbb{H}$ orientation

Figure 4.8: Unit test for coupled problem

Load step	**Applied magnetic potential difference**	**Applied mechanical traction p_0**
25%	500	0
50%	1000	0
75%	1000	5e-3
100%	1000	1e-2

Table 4.1: Load values at different load steps for coupled unit test problem

The constitutive law stated in Equation (4.11) was employed to describe the material response for the coupled unit test problem and the chosen values for the material parameters are $\mu = 3e^{-2}$ Pa, $\nu = 0.4$ and relative permeability $\mu_r = 6.0$. A magnetic potential difference of 1000 per unit length was applied in first half of total load cycle and a prescribed traction load $\mathbf{t}^p = 1e^{-2}\frac{\mathrm{N}}{\mathrm{m}}$ was applied in the second half of total load application cycle. The corresponding loads at different load steps is mentioned in Table 4.1.

In reference to the resulting deformations at different load steps in Figures 4.9a and 4.9b, in the first half cycle with the magnetic load application we observe the geometry undergoes compression. Due to the prescribed magnetic potentials at the top and bottom boundaries a vertically aligned magnetic field is generated as observed in Figure 4.8c. With no deformations in the initial reference configuration ($\mathbf{F} = \mathbf{C} = \mathbf{I}$

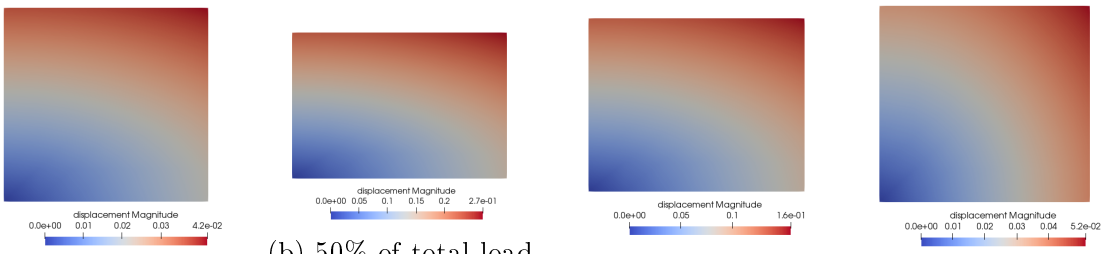

(a) 25% of total load (b) 50% of total load (c) 75% of total load (d) Total load

Figure 4.9: Deformations of the unit cube under coupled magnetic and mechanical load (Scale of each result is to be noted)

and $J = 1 \implies \Psi^{\text{elas}} = 0$) following Equation (4.11), we have a high negative definite contribution to $\mathfrak{C}$ from $\mu_0 M_0$. Due to this effect the material softens and becomes less stiff at high magnetic loads. With no mechanical load in the first phase of loading, the vertically aligned magnetic field induces compressive stresses aligned with the magnetic field. This leads to a compression of the material. After the full magnetic load is applied, the material then experiences a tensile load due to the mechanical traction load applied on the top surface in the second half load cycle. For the considered material stiffness parameters, a small traction load is required to overcome the compression developed by the high magnetic load. Thus, the material extends back to its original form as observed in Figure 4.9d.

4.8.1 Dependence of material response on the direction of magnetic field

To test the dependence of the field $\mathbb{H}$ direction on the material response, the prescribed magnetic potential was reversed, i.e. a positive potential $\phi = +\overline{\phi}$ on the top boundary and a negative potential $\phi = -\overline{\phi}$ on the bottom boundary was prescribed as seen in Figure 4.10a. The resulting magnetic field direction in Figure 4.10b is opposite when compared to Figure 4.8c. It was observed that irrespective of the magnetic field direction the resulting material response remained unchanged. For the reversed field direction the material experienced same compression and resulted in same deformed states as observed in Figure 4.9. This helps understand that the alignment of the resulting magnetic field w.r.t. the axisymmetric geometry is of importance rather than the direction in which it points. It also points out that the magnetic field leads to a compressive response of the magneto-elastic material for high magnetic loads (when modelled with no free space).

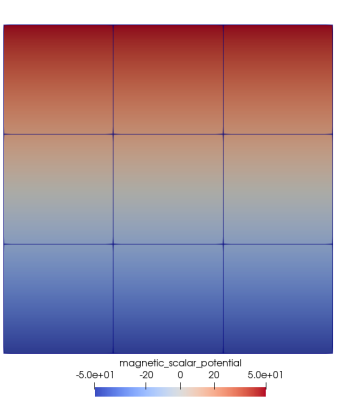

(a) Reversed potential ϕ prescribed

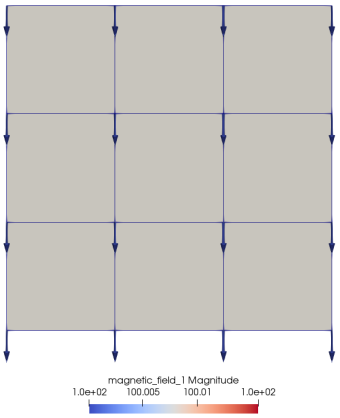

(b) Resulting field $\mathbb{H}$ direction

Figure 4.10: Test for reversed magnetic field direction

4.9 Numerical results for coupled magneto-elastic torus membrane with free space

We now examine the coupled problem of the torus magneto-elastic membrane with the surrounding free space as mentioned in Section 4.7. The load application explained in Section 4.7.2 is to be considered unless another load application set up is mentioned. The membrane is modelled as a non-linear hyperelastic material employing the constitutive material model Equation (4.11) with coupling between the magnetic and the elastic quantities. We consider the neighbouring free space as a complaint elastic material modelled with the same material model but with relatively low elastic stiffness. The material parameters considered for the membrane are $\mu = 3e^4$ Pa and $\nu = 0.4$, whereas the free space material parameters considered are $\mu = 3e^1$ Pa and $\nu = 0.3$. The quasi-static inflating traction load applied was $p_0 = 1500$ Pa. A high magnetic potential difference of $3.5e^5$ per unit length was prescribed in the first half of total load cycle. The load values at different load steps are mentioned in Table 4.2.

Load step	**Applied magnetic potential difference**	**Applied mechanical traction p_0**
25%	$1.75e^5$	0
50%	$3.5e^5$	0
75%	$3.5e^5$	750
100%	$3.5e^5$	1500

Table 4.2: Load values at different load steps for torus magneto-elastic membrane with free space problem

4.9.1 Deformations of the membrane under combined loads

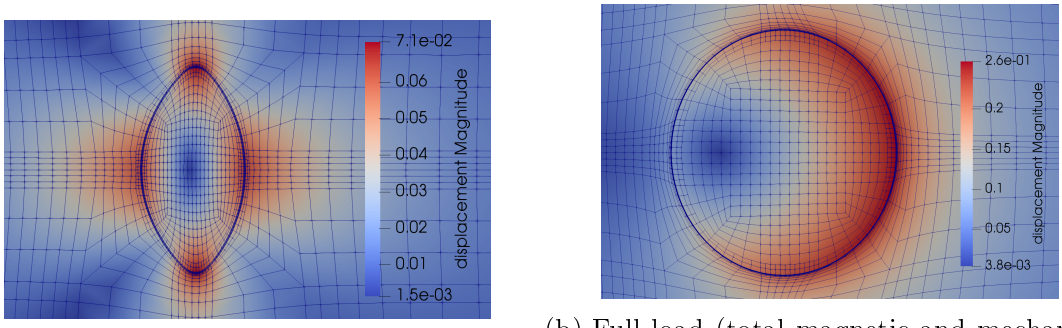

(a) Half load (total magnetic load applied)

(b) Full load (total magnetic and mechanical load)

Figure 4.11: Deformations of the membrane and neighbouring free space for coupled problem

We observe the deformed states of the domain at the end of the magnetic load application in Figure 4.11a and at the end of the total magnetic and mechanical load application in Figure 4.11b, respectively. As found out from the unit test result in Section 4.8, on the application of high magnetic loads the material undergoes compression for the vertically aligned magnetic field. We observe a similar effect on the magneto-elastic membrane in the first half of total load cycle (linearly increasing magnetic load and zero mechanical load). The membrane undergoes finite deformations in the lateral and longitudinal directions. The centre of the membrane shifts by negligible magnitude along the radial direction. The membrane thickness also has negligible change at this state. The displacements in the membrane sections along the cylindrical co-ordinate axes direction are significantly high compared to the other sections.

In the second phase of loading, the membrane starts to inflate on the application of high inflating pressure load, c.f. Figure 4.11b. The applied high traction load overcomes the effect of the compressive forces developed by the magnetic load. The membrane expands back to a circular topology within first few traction application load steps. On further load application, the membrane then inflates to a larger radius. The torus minor radius at the end of total load application has increased from 0.195 m to $\approx$ 0.38 m. The centre of the torus has also shifted by a significant distance of 0.1 m to the right. The membrane thickness due to the large stretch has reduced from $5e^{-3}$ m to $\approx 2.8e^{-3}$ m. As was explained in the quasi-static finite strain elasticity results in Chapter 3, the strains on the right half of the circular cross-section are relatively large compared to the left half. This is due to the dependence of $\mathbf{F}$ (component F_{33}) on the radial distance of the respective point from the axis of symmetry.

It is important to note that the current load values were chosen to demonstrate the finite deformations the membrane can undergo before the onset of any mechanical instability in the membrane (or the complaint free space). On further increasing the magnetic

and mechanical pressure load, it was observed that either the Newton solver would not converge or we would observe material instability in the free space elements in close vicinity to the deforming membrane.

4.9.2 Comparative study of deformations under two different load set ups

To demonstrate the finite deformations of the membrane for the considered loads of chosen values, we now study the deformations under a reversed load application cycle. Until now we have employed the method mentioned in Section 4.7.2 in Figure 4.6b. We shall refer to this as 'Load set up 1'. We now consider another load application cycle with the mechanical load applied in initial phase followed by the magnetic load; here referred to as 'Load set up 2'. We examine the deformed states of the magneto-elastic membrane under the two different load set ups. It is important to note that the magnitude of magnetic and the mechanical loads are kept same (as mentioned in Section 4.9) but the order of application of the respective loads is changed. The load values for 'Load set up 2' are mentioned in Table 4.3.

Load step	**Applied magnetic potential difference**	**Applied mechanical traction p_0**
25%	0	750
50%	0	1500
75%	$1.75e^5$	1500
100%	$3.5e^5$	1500

Table 4.3: Load values for reversed load cycle in the torus magneto-elastic membrane with free space problem

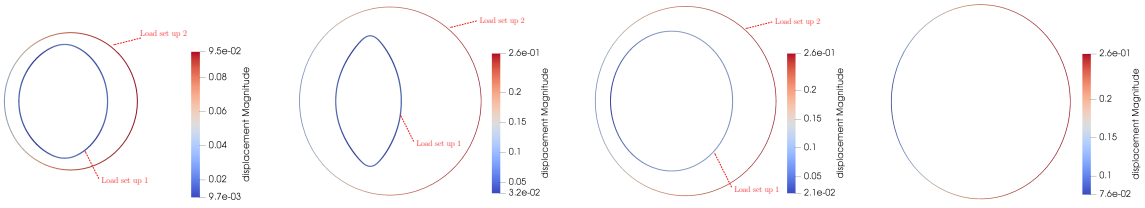

(a) 25% of total load (b) 50% of total load (c) 75% of total load (d) Total load

Figure 4.12: Comparison between deformed states of magneto-elastic membrane for two different (equal in magnitude) load application set ups

We observe the comparative results for the deformed states of the membrane at different load steps in Figure 4.12. One can easily identify the differences in the results under different load set up from Figures 4.12a to 4.12c. It is interesting to point out that

irrespective of the order in which one applies the loads (before any material instability is observed), the final deformed states for both the load set ups are exactly identical as observed in Figure 4.12d. For the employed hyperelastic material model, this is exactly what one would expect. As for hyperelastic materials under a quasi-static loading the obtained deformation would be same irrespective of the load application path, i.e. if one were to take more load steps or a different load application cycle with the final applied load of same magnitude, we would have same deformed state. The resulting stresses developed in the membrane under both the load set ups also matched and verified the observed phenomena. For the 'Load set up 2', it is evident that the applied magnetic load in second phase is not large enough to observe finite deformations of the new inflated membrane geometry.

We compare the load-displacement history for two points on the membrane inner radius in Figure 4.13. First point is at the position (1.095, 0) located at $\Theta = 0°$ (on the right section of the membrane) and the second point of interest is at position (0.9, 0.195) located at $\Theta = 90°$, both measured anti-clockwise respectively. Though the equilibrium paths for both the load set ups are different, the final displacements in both the cases are same. The observed "kinks" in the graph for 'Load set up 1' is due to the reversed direction of deformation on the application of inflating pressure load in the second half cycle. The first kink is due to the membrane regaining its circular topology. The second kink observed is the result of the expansion of the membrane upon increasing pressure load. It is important to note that the equilibrium path in the second phase of loading in 'Load set up 1' is linearly increasing, thus indicating that the observed large deformations are still in stable regime and that the elastic critical limit point at which the tangent stiffness approaches to zero, hasn't arrived yet. Thus, we do not observe any buckling instability for the considered load values. For the further instability modes study, we shall continue with the 'Load set up 1' where the magnetic load is applied in first phase.

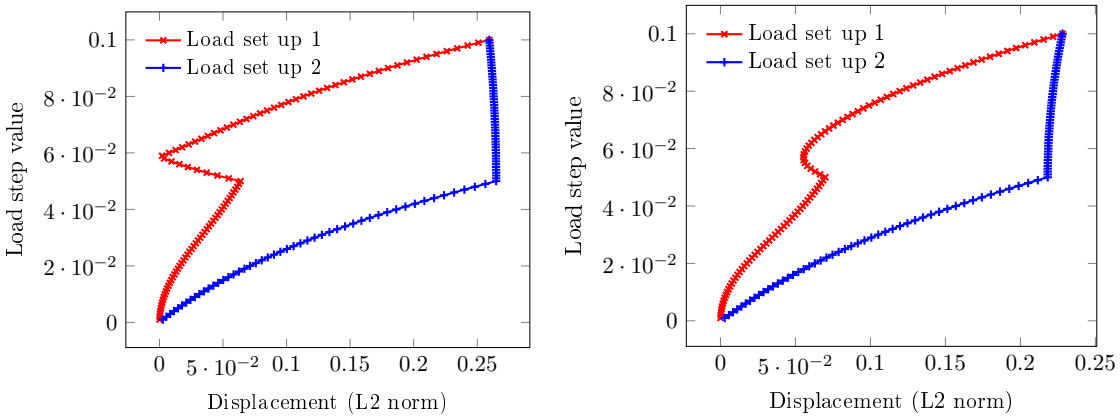

(a) Point 1 at $\Theta = 0°$ (b) Point 2 at $\Theta = 90°$

Figure 4.13: Equilibrium paths

4.9.3 Study of unstable deformations of the membrane

The thickness of a structure affects the bending stiffness of the structure. Bending stiffness is the resistance offered by the structure against any bending deformation. It is a function of the elastic modulus E of the structure and the second moment area (also known as area moment of inertia) I of the structure cross-section about the axis of interest. Bending stiffness in beams is also termed as **flexural rigidity**. Since the second moment area I depends on the cross-section dimensions of the structure, thickness of the structure thus plays a role in observing the unstable buckling deformations of our interest. Thus, to study the membrane unstable deformations leading to the buckling of the membrane we consider a membrane of reduced thickness. The magneto-elastic membrane thickness was reduced by half to 0.0025 m. The corresponding membrane minor inner and outer radii are 0.195 m and 0.1975 m, respectively. The reduced thickness of membrane was spatially discretized into four elements along the thickness to get high accuracy of the results in the membrane when observing the buckling behaviour.

The material parameters were taken as mentioned earlier in Section 4.9. For the results to be observed, an externally applied magnetic potential difference of $3e^5$ per unit length was considered and the traction load was set to $p_0 = 1500$ Pa. As mentioned earlier, the buckling deformations of our interest are observed for an established magnetic field $\mathbb{H}$ and with increasing large mechanical pressure loads [38, 41]. Therefore we consider the load set up with the magnetic potential application in first phase.

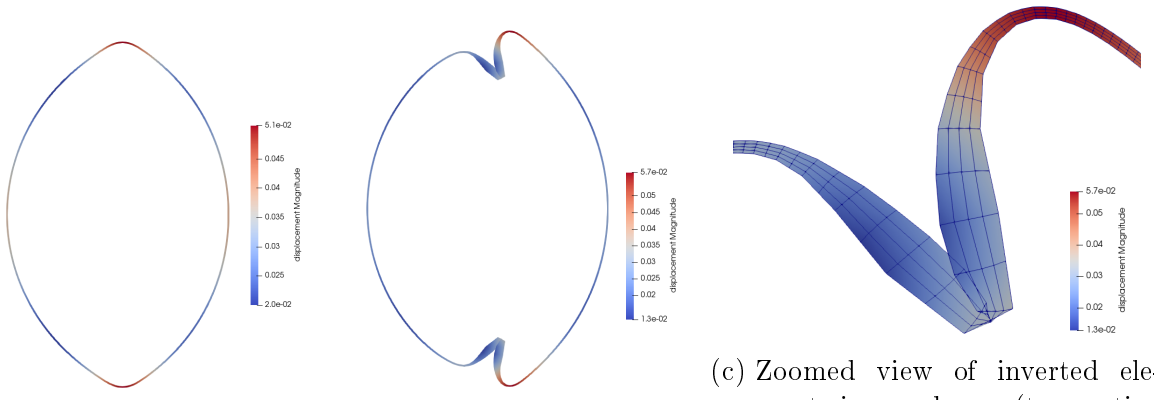

(a) Before numerical failure (b) After numerical failure (c) Zoomed view of inverted elements in membrane (top section at $\Theta = 90°$)

Figure 4.14: Magneto-elastic membrane during numerical failure

We examine the results for the magneto-elastic membrane in Figure 4.14. For the considered load values, material parameters and membrane thickness, we observe a numerical failure of the employed (direct coupled) solution method. The result in Figure 4.14a is at the end of the magnetic loading, i.e. end of the first phase of loading. The numerical failure observed in Figure 4.14b is at the first load step of the second phase of loading, i.e. the mechanical inflating pressure load application. The membrane

appears to buckle at the large pressure applied in the first step on the new compressed (oval) geometry structure. The buckling of the membrane occurs at the sections located along the longitudinal axes at $\Theta = 90°$ and $\Theta = 270°$. On close examination of the elements in these sections, we observe inverted elements at the region near the kink in Figure 4.14c.

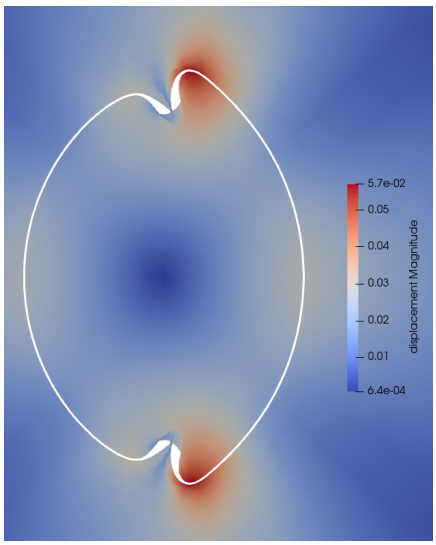

(a) After numerical failure

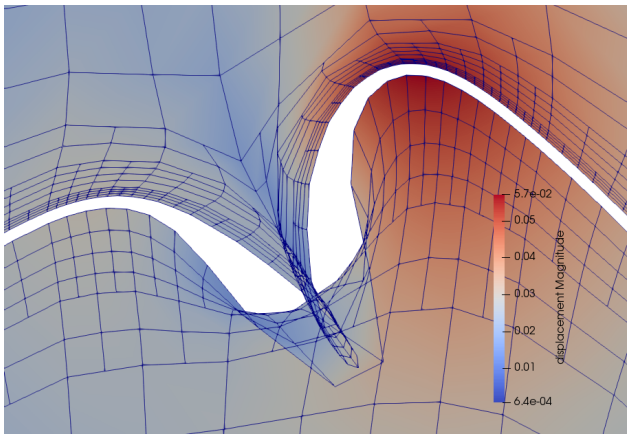

(b) Zoomed view of inverted elements in free space (top section at $\Theta = 90°$)

Figure 4.15: Free space elements surrounding the membrane causing the numerical failure (white section is the cut-out membrane for better visualization purpose)

We now focus on the elements in the free space neighbouring the membrane where we observed numerical failure. It is important to note that the free space material is modelled as a very complaint elastic body with elastic stiffness relatively low compared to the membrane's stiffness. Observing Figure 4.15b, it is suspected that the cause of the numerical failure is the inversion of elements in the complaint free space with non-invertible deformation maps $\boldsymbol{\varphi}$. One can clearly observe the outer free space elements have intersected with the inner free space elements, thus crossing the membrane region (white cut-out section). The reason for this numerical failure is due to the direct solution of the coupled problem, solving for both the magneto-elastic membrane as well as the complaint free space together. Use of a segregated solution method can be motivated to overcome this failure in modelling buckling of the membrane. In the segregated approach, one splits the solution to the problem of deformable geometry (in our case the magneto-elastic membrane) from the mesh update of the surrounding free space. In the first stage, one would consider the degrees of freedom in membrane only and solve the coupled problem for finite deformations of the magneto-elastic body without considering the free space degrees of freedom. In the next stage, which is termed as **moving-mesh update** in literature [20] and [36] for the magneto-active polymers, one would then use

the solution of the first stage coupled problem as the necessary inhomogeneous Dirichlet boundary conditions and solve another boundary value problem to compute a suitable deformation map $\boldsymbol{\varphi}$ in the free space $\mathcal{S}_0$. Such techniques were developed for problems in fluid mechanics and fluid-structure interaction problems where large deformations and moving domains, boundaries and interfaces are to be modelled accurately. Employing this staggered algorithm, one could then truly be able to move past the critical point of numerical artefact as observed in above results for the failing simulations. Due to time restrictions to submit the thesis report, the work in the direction to implement such a mesh update algorithm could not be done and presented in this report. Readers interested to know more about the staggered approach are directed to [see 36, Sec. 7] and the references mentioned therein.

5 Summary and outlook

To summarize this thesis, a robust framework for coupled multi-physics problem of magneto-elasticity was developed using an open-source C++ FEM library. The framework was capable of solving the individual decoupled fields, namely the magnetic scalar potential and the vector-valued displacement fields, and also the fully coupled problem for finite deformations. The framework was tested with many simple models and unit tests to validate the implementation as well as the obtained results. Axisymmetric solids along with axisymmetric loads and boundary conditions are focussed on, in particular.

In the first part of the research work, we solved a magneto-static problem involving no deformations of the domain. Here, the considered magnetic balance equations were discretized employing a scalar magnetic potential formulation. The magnetic field $\mathbb{H}$ was taken as the independent field and defined in terms of a fictitious magnetic scalar potential ϕ. The resulting variational axisymmetric formulation was numerically solved using standard Lagrange finite elements. To validate the results obtained using the axisymmetric geometry, an analogous 3D geometry was developed for the magneto-elastic membrane and the surrounding free space. The results of the 3D simulation were compared to the axisymmetric (2.5D) simulation. An energy metric was computed to account for the total energy present in the membrane. Comparison of the energy metric values in 2.5D and 3D simulation for each h-adpative mesh refinement cycle were done. It was observed that the developed axisymmetric formulation was numerically correct under acceptable tolerance.

In the second phase of research, the finite elastic deformations of the torus membrane were studied under the applied quasi-static inflating pressure load. The existing framework of magneto-statics was extended to include the non-linear elasticity problem. The magneto-elastic membrane and the surrounding free space were modelled using the hyperelastic Neo-Hookean constitutive law. Linearisation of the non-linear problem was presented using the first-order Taylor expansion about the current known solution. The vector-valued problem was discretized using vector-valued finite elements. A uniformly increasing load stepping algorithm was implemented and the solution of the non-linear system was carried out employing the Newton-Raphson iterative method. Since the free space was modelled as a very complaint elastic solid of relatively low elastic stiffness, a parametric study of the free space shear modulus μ was performed. An appropriate elastic stiffness of the free space material was found in order to have no obstructive/reactive force from the free space on the free inflation of the membrane. The instability problem was examined for finite-strain elasticity test models from the literature modelled without any free space. The failure of the Newton method to capture the unstable deformation

in the Crisfield beam model was presented. Thus, the need of the path-following solution method was highlighted for the further instability studies in coupled problem.

In the final part, coupling between the magneto-static and the finite-strain elasticity problem was implemented. The material model for the coupled magneto-elastic membrane was presented and the constitutive relations and tangents were derived. Conclusions were drawn from the results of the experiment for the permanent magnet region with the applied potential in the magneto-static problem and the application of the magnetic loads for the coupled problem was altered appropriately. The solution of the resulting saddle point system was carried out by the Schur complement reduction. To examine the unstable buckling deformations of the membrane, a thin membrane of reduced thickness was considered. An attempt to model the instabilities at/near limit point loads was presented. The reason for the observed numerical failure in the free space elements at the unstable deformation of the magneto-elastic membrane was highlighted.

Possible extensions

As observed in the final results for the buckling instabilities in the membrane for the coupled problem, one immediate possible extension to circumvent the numerical failure, arising due to non-invertible deformation maps in the free space region neighbouring the buckling membrane, is employing a staggered modelling approach. The problem will be split in two sub-problems. The first sub-problem will be to solve for the finite deformations of the elastic membrane neglecting the degrees of freedom in the free space. In the second sub-problem the obtained deformations of the membrane in the earlier sub-problem will be used as the inhomogeneous Dirichlet boundary conditions. A boundary value problem will be solved for the deformations of the free space elements with resulting invertible deformation maps. The approach is termed the "moving-mesh update" in the literature for the fluid mechanics and fluid-structure interaction problems.

Another avenue of extension will be to get the implemented the path-following Arc-Length solver to function correctly. The current Newton method would fail past the critical limit points due to the negative elastic tangents and the lack of the Newton solver to dynamically adapt the load parameter value.

Certainly one could also employ more complex constitutive models such as the Mooney-Rivlin and Arruda-Boyce material model to study their instabilities in depth. Employing an incompressible magneto-elastic membrane for such complex modelling involving complex geometry and external load applications is another open-ended research direction to explore.

Appendix

Rules of Tensor analysis.

Tensor notation:

1. $\mathbf{x} = x_i \mathbf{e}_i$
2. $\mathbf{Y} = Y_{IJ} \mathbf{E}_I \otimes \mathbf{E}_J$
3. $\mathbf{Z} = Z_{IJK} \mathbf{E}_I \otimes \mathbf{E}_J \otimes \mathbf{E}_K$

Inner products:

1. $\mathbf{A} \cdot \mathbf{B} = A_{IJ} B_{JK} \mathbf{E}_I \otimes \mathbf{E}_K$
2. $\mathbf{A} : \mathbf{B} = A_{IJ} B_{IJ}$

Dyadic product: $\mathbf{A} \otimes \mathbf{B} = A_{IJ} B_{KL} \mathbf{E}_I \otimes \mathbf{E}_J \otimes \mathbf{E}_K \otimes \mathbf{E}_L$

Differential operator: $\nabla_{\mathbf{X}} \mathbf{a} = \frac{\partial a_i}{\partial X_J} \mathbf{e}_i \otimes \mathbf{E}_J$

Bibliography

[1] HF Tiersten. "Coupled magnetomechanical equations for magnetically saturated insulators". In: *Journal of Mathematical Physics* 5.9 (1964), pp. 1298–1318.

[2] William Fuller Brown and William Fuller Brown. *Magnetoelastic interactions*. Vol. 9. Springer, 1966.

[3] E. Riks. "An incremental approach to the solution of snapping and buckling problems". In: *International Journal of Solids and Structures* 15.7 (1979), pp. 529–551. DOI: 10.1016/0020-7683(79)90081-7.

[4] M.A. CRISFIELD. "A FAST INCREMENTAL/ITERATIVE SOLUTION PROCEDURE THAT HANDLES "SNAP-THROUGH"". In: *Computational Methods in Nonlinear Structural and Solid Mechanics*. Elsevier, 1981, pp. 55–62. DOI: 10.1016/b978-0-08-027299-3.50009-1.

[5] D. W. Kelly et al. "A posteriori error analysis and adaptive processes in the finite element method: Part I—error analysis". In: *International Journal for Numerical Methods in Engineering* 19.11 (Nov. 1983), pp. 1593–1619. DOI: 10.1002/nme.1620191103.

[6] Attay Kovetz. *Electromagnetic theory*. Vol. 975. Oxford University Press Oxford, 2000.

[7] Timothy A Davis. "Algorithm 832: UMFPACK V4. 3—an unsymmetric-pattern multifrontal method". In: *ACM Transactions on Mathematical Software (TOMS)* 30.2 (2004), pp. 196–199.

[8] A. Dorfmann and R. W. Ogden. "Nonlinear magnetoelastic deformations". In: *The Quarterly Journal of Mechanics and Applied Mathematics* 57.4 (2004), pp. 599–622. DOI: 10.1093/qjmam/57.4.599. eprint: /oup/backfile/content_public/journal/qjmam/57/4/10.1093/qjmam/57.4.599/2/570599.pdf. URL: http://dx.doi.org/10.1093/qjmam/57.4.599.

[9] S.V. Kankanala and N. Triantafyllidis. "On finitely strained magnetorheological elastomers". In: *Journal of the Mechanics and Physics of Solids* 52.12 (2004), pp. 2869–2908. ISSN: 0022-5096. DOI: https://doi.org/10.1016/j.jmps.2004.04.007. URL: http://www.sciencedirect.com/science/article/pii/S0022509604000821.

[10] Michele Benzi, Gene H. Golub, and Jörg Liesen. "Numerical solution of saddle point problems". In: *Acta Numerica* 14 (May 2005), pp. 1–137. DOI: 10.1017/s0962492904000212.

[11] A. Dorfmann and R. W. Ogden. "Some problems in nonlinear magnetoelasticity". In: *Zeitschrift für angewandte Mathematik und Physik ZAMP* 56.4 (July 2005), pp. 718–745. ISSN: 1420-9039. DOI: 10.1007/s00033-004-4066-z. URL: https://doi.org/10.1007/s00033-004-4066-z.

[12] Michael A. Heroux et al. "An overview of the Trilinos project". In: *ACM Trans. Math. Softw.* 31.3 (2005), pp. 397–423. ISSN: 0098-3500. DOI: http://doi.acm.org/10.1145/1089014.1089021.

[13] "Cubit: Geometry and mesh generation toolkit". In: *URL: https://cubit.sandia.gov* (2006).

[14] Michael W Gee et al. *ML 5.0 smoothed aggregation user's guide*. Tech. rep. Technical Report SAND2006-2649, Sandia National Laboratories, 2006.

[15] W. Bangerth, R. Hartmann, and G. Kanschat. "deal.II – a General Purpose Object Oriented Finite Element Library". In: *ACM Trans. Math. Softw.* 33.4 (2007), pp. 24/1–24/27.

[16] M Barham et al. "Limit-point instability of a magnetoelastic membrane in a stationary magnetic field". In: *Smart Materials and Structures* 17.5 (July 2008), p. 055003. DOI: 10.1088/0964-1726/17/5/055003.

[17] Peter Wriggers. *Nonlinear Finite Element Methods*. Springer-Verlag GmbH, Sept. 24, 2008. ISBN: 3540710000. URL: https://www.ebook.de/de/product/7511919/peter_wriggers_nonlinear_finite_element_methods.html.

[18] Matthew I. Barham, Daniel A. White, and David J. Steigmann. "Finite element modeling of the deformation of magnetoelastic film". In: *Journal of Computational Physics* 229.18 (2010), pp. 6193–6207. ISSN: 0021-9991. DOI: https://doi.org/10.1016/j.jcp.2010.04.007. URL: http://www.sciencedirect.com/science/article/pii/S002199911000183X.

[19] Glenn Hrinda. "Snap-through instability patterns in truss structures". In: 2010, p. 2611.

[20] Roger Bustamante, Alois Dorfmann, and Ray W Ogden. "Numerical solution of finite geometry boundary-value problems in nonlinear magnetoelasticity". In: *International Journal of Solids and Structures* 48.6 (2011), pp. 874–883.

[21] Raymond Ogden and David Steigmann. *Mechanics and electrodynamics of magneto-and electro-elastic materials*. Vol. 527. Springer Science & Business Media, 2011.

[22] Yi Han. "Mechanics of magneto-active polymers". PhD thesis. Iowa State University, 2012. DOI: 10.31274/etd-180810-525.

[23] Jean-Paul Pelteret and Andrew McBride. *The deal.II Tutorial Step-44: Three-Field Formulation For Non-Linear Solid Mechanics*. 2012. DOI: 10.5281/zenodo.439772.

[24] Roger Bustamante and Ray W Ogden. "Nonlinear magnetoelastostatics: Energy functionals and their second variations". In: *Mathematics and Mechanics of Solids* 18.7 (2013), pp. 760–772. DOI: 10.1177/1081286512448347. eprint: https://doi.org/10.1177/1081286512448347. URL: https://doi.org/10.1177/1081286512448347.

[25] Stanislaw H. Zak Edwin K. P. Chong. *An Introduction to Optimization*. JOHN WILEY & SONS INC, Jan. 14, 2013. 640 pp. ISBN: 1118279018. URL: https://www.ebook.de/de/product/19579661/edwin_k_p_chong_stanislaw_h_zak_an_introduction_to_optimization.html.

[26] Stephan Rudykh and Katia Bertoldi. "Stability of anisotropic magnetorheological elastomers in finite deformations: a micromechanical approach". In: *Journal of the Mechanics and Physics of Solids* 61.4 (2013), pp. 949–967.

[27] O. C. Zienkiewicz et al. *The Finite Element Method for Solid and Structural Mechanics*. Elsevier LTD, Oxford, Nov. 12, 2013. 768 pp. ISBN: 1856176347. URL: https://www.ebook.de/de/product/21021815/o_c_zienkiewicz_robert_l_taylor_david_a_fox_olek_c_zienkiewicz_the_finite_element_method_for_solid_and_structural_mechanics.html.

[28] Luis Dorfmann and Ray W. Ogden. *Nonlinear Theory of Electroelastic and Magnetoelastic Interactions*. Springer US, 2014. DOI: 10.1007/978-1-4614-9596-3.

[29] F. Vogel et al. "Magnetic force and torque on particles subject to a magnetic field". In: *European Journal of Mechanics - A/Solids* 48 (Nov. 2014), pp. 23–37. DOI: 10.1016/j.euromechsol.2014.03.007.

[30] Timothy A Davis et al. "Suitesparse: a suite of sparse matrix software". In: *URL http://faculty. cse. tamu. edu/davis/suitesparse. html* (2015).

[31] C. Miehe, D. Vallicotti, and D. Zäh. "Computational structural and material stability analysis in finite electro-elasto-statics of electro-active materials". In: *International Journal for Numerical Methods in Engineering* 102.10 (Jan. 2015), pp. 1605–1637. DOI: 10.1002/nme.4855.

[32] Prashant Saxena, Jean-Paul Pelteret, and Paul Steinmann. "Modelling of iron-filled magneto-active polymers with a dispersed chain-like microstructure". In: *European Journal of Mechanics - A/Solids* 50 (Mar. 2015), pp. 132–151. DOI: 10.1016/j.euromechsol.2014.10.005.

[33] Nikolaos Vasios. *Nonlinear Analysis of Structures The Arc Length Method: Formulation, Implementation and Applications*. Tech. rep. Harvard University, 2015.

[34] Marc-Andre Keip and Matthias Rambausek. "A multiscale approach to the computational characterization of magnetorheological elastomers". In: *International Journal for Numerical Methods in Engineering* 107.4 (2016), pp. 338–360.

[35] Jean-Paul Pelteret and Andrew McBride. *The deal.II Code Gallery: Quasi-Static Finite-Strain Compressible Elasticity*. 2016. DOI: 10.5281/zenodo.1228964.

[36] Jean-Paul Pelteret et al. "Computational electro-elasticity and magneto-elasticity for quasi-incompressible media immersed in free space". In: *International Journal for Numerical Methods in Engineering* 108.11 (2016), pp. 1307–1342. DOI: 10.1002/nme.5254. eprint: https://onlinelibrary.wiley.com/doi/pdf/10.1002/nme.5254. URL: https://onlinelibrary.wiley.com/doi/abs/10.1002/nme.5254.

[37] Nikhil Buduma. "Fundamentals of Deep Learning". In: O'Reilly Media, Inc., 2017. Chap. 4. ISBN: 9781491925607.

[38] Narravula Harshavardhan Reddy and Prashant Saxena. "Limit points in the free inflation of a magnetoelastic toroidal membrane". In: *International Journal of Non-Linear Mechanics* 95 (2017), pp. 248–263. ISSN: 0020-7462. DOI: https://doi.org/10.1016/j.ijnonlinmec.2017.06.017. URL: http://www.sciencedirect.com/science/article/pii/S0020746217301282.

[39] G. Alzetta et al. "The `deal.II` Library, Version 9.0". In: *Journal of Numerical Mathematics* 26.4 (2018), pp. 173–183. DOI: 10.1515/jnma-2018-0054.

[40] Vinayak Gholap. *Computationally scalable and efficient Multigrid implementation for long-range Coulomb interaction in atomistic simulations using h-adaptive Finite Element Method*. Tech. rep. Friedrich-Alexander University Erlangen–Nuremberg, 2018.

[41] Narravula Harshavardhan Reddy and Prashant Saxena. "Instabilities in the axisymmetric magnetoelastic deformation of a cylindrical membrane". In: *International Journal of Solids and Structures* 136 (2018), pp. 203–219.